

UNIVERSIDADE DE LISBOA
INSTITUTO SUPERIOR TÉCNICO
Università degli Studi di Padova

Tokamak Magnetic Control Simulation: Applications for JT60-SA and ISTTOK Operation.

Doménica Corona Rivera

Supervisor: Prof. Horácio Fernandes

Co-Supervisor: Prof. Nuno Cruz

External supervisor: Prof. Alfredo Pironti

Thesis specifically prepared to obtain the PhD Degree in
Technological Physics Engineering

Month 2020

ABSTRACT

Abstract en ingles

Keywords:Real-time control, plasma current, centroid position, state-space

RESUMO

Abstract em tuga

Palavras-chave:

SOMMARIO

Abstract em italiano

Parole chiave:

ACKNOWLEDGEMENTS

This work was supported by Fundação para a Ciência e a Tecnologia (FCT) under the grant No.**PD/BD/114306/2016** carried out as part of the training in the framework of the Advanced Program in Plasma Science and Engineering (APPLAuSE, sponsored by FCT under grant No. PD/00505/2012).

CONTENTS

1	INTRODUCTION	3
1.1	Behind the plasma current	4
1.2	Plasma control in tokamaks	7
1.3	Thesis outline	9
2	PLASMA CONTROL SYSTEMS	11
2.1	Overview of control systems	11
2.1.1	DIII-D Plasma Control System	11
2.1.2	Système de Contrôle Distribué	13
2.2	MARTe framework	13
2.2.1	MARTe architecture	14
2.2.2	MARTe hardware containers	14
2.2.3	MARTe 2.0	16
2.3	Tokamak equilibrium codes	18
2.4	Control Techniques and State-Space models	20
2.4.1	State-Space models	20
2.4.2	PID control	22
2.4.3	Multiple-Input Multiple-Output control	24
2.4.4	Observers and Kalman filters	28
2.4.5	Experimental identification of state-space models	30
3	JT60-SA CONTROL DESIGN	33
3.1	Machine description	33
3.2	CREATE magnetic reconstruction tools	35
3.3	Controller design	36
3.4	QST reconstruction and control implementation	39
3.4.1	Cauchy Condition Surface (CCS) reconstruction method	39
3.4.2	QST magnetic controller	39
3.5	Simulation results	41
3.5.1	Disturbances	42
3.5.2	Gap-based XSC	43
3.5.3	Isoflux XSC and QST controller	46
3.5.4	Shape reference change	50
4	ISTTOK	57

Contents

4.1	Machine description	57
4.1.1	ISTTOK AC plasma current	60
4.2	Diagnostics and Actuators	60
4.2.1	Poloidal Field Coils	62
4.3	ISTTOK Hardware	64
4.3.1	ATCA-MIMO-ISOL boards	64
4.4	Real-time integration software	66
4.5	Plasma current magnetic field	69
4.5.1	PF coils state-space model estimation	69
4.6	Plasma centroid position determination	70
4.7	Real-time MARTe implementations for the plasma position reconstruction	72
4.7.1	Poloidal magnetic external contributions subtraction	72
4.7.2	Plasma current and centroid position reconstruction	73
5	ISTTOK CONTROL IMPLEMENTATIONS AND RESULTS	77
5.1	Implementation of the General Application Modules	77
5.1.1	PID control implementation	78
5.1.2	Data-driven state-space model retrieving	79
5.1.3	Kalman filter implementation	81
5.1.4	Multiple-Input Multiple-Output control implementation	82
5.2	Plasma current centroid position control results	88
6	CONCLUSIONS	95
6.1	General Conclusion	95
6.2	JT60-SA	95
6.3	ISTTOK	95
	Bibliography	103
A	EXTENDED CONTROL RESULTS	105
B	JT60-SA PICTURES	119

LIST OF FIGURES

Figure 1.1	Helical trajectory of a charged particle in a uniform magnetic field [1, Chapter 8].	3
Figure 1.2	Toroidal drift, particles drift in the vertical direction. [2, Chapter 3]	4
Figure 1.3	Rotational transform angle ι formed when the magnetic force lines generated by the combination of toroidal and poloidal field cross the plane P in different points [2, Chapter 3].	5
Figure 1.4	Toroidal geometry and variables used for the calculations of the toroidal force balance and the vertical field [1, Chapter 11].	6
Figure 1.5	PF vertical coils and magnetic field lines.	7
Figure 2.1	DIII-D digital PCS in 1991 [8].	12
Figure 2.2	Actual DIII-D PCS real-time systems [10].	12
Figure 2.3	TCV SCD. Real-time network nodes connection. The nodes configurations are shown together with the typical diagnostic and actuator systems to which they are connected [13].	13
Figure 2.4	Example of a set of GAMs connected to the DDB. Timing and hardware GAMs provide the I/O interface to the exterior, whereas a generic waveform GAM inputs the reference for a PID controller. Finally, the output is sent to a DAC and the data is stored for analysis by a collection GAM. It should be noticed that the reference generation and the controller GAM are not aware of the changes in the data providers and data consumers. [17]	14
Figure 2.5	JET ATCA hardware. The acquisition boards map in the controller computer memory a set of four buffers, the selected one is consecutively cycled every $50 \mu s$ by the firmware. The first value written is the header and contains the absolute time since the last trigger, followed by the acquired values of the ADCs, and finally by the footer containing the same value as the header. [14]	15
Figure 2.6	ATCA control board with 32 ADCs developed and assembled at the IPFN. [18]	16
Figure 2.7	The ISTTOK tomography system has 30 acquisition channels connected by an Input-Output ATCA card and sent to MARTe framework. [21]	16
Figure 2.8	Schematic of COMPASS tokamak control and data acquisition system, two ATCA systems are responsible for the fast control of the device and for the data acquisition. [18]	17
Figure 2.9	Sketch of the integration of the state observer RAPTOR in the RFX-mod real-time control system based on the MARTe framework. experimental [31]	19

List of Figures

Figure 2.10	Plant and PID controller block scheme on Laplace domain [41, Chapter 9]. 23
Figure 2.11	Plant with a proportional (P) control scheme on the Laplace domain and its response to a unit-step. The offset or error between the steady-state response is also pointed out [42, Chapter 5]. 24
Figure 2.12	Plant scheme of a plant with a proportional-integral (PI) control on the Laplace domain. Bottom graph corresponds to a step response to closed-loop systems with D and a PI controller [41, Chapter 9], a visible improvement on the state-state error with the PI control is observable. 25
Figure 2.13	The top scheme shows a PD controller for a plant that is only modeled as an inertial load, on the graph below is shown the system response where it is possible to observe an offset reduction and a controlled transient as compared with the P controller [42, Chapter 5]. 26
Figure 2.14	Step response to closed-loop systems with D,PD and PID controllers [41, Chapter 9]. 26
Figure 2.15	State-space model with a K gain matrix feedback scheme. 27
Figure 2.16	Scheme of a state-space model plant and its observer or state estimator. 29
Figure 3.1	JT60-SA tokamak configuration and its main elements [49]. 33
Figure 3.2	JT-60SA poloidal cross-section and layout of the Poloidal Field coils system [50]. 34
Figure 3.3	LCFS Equilibria corresponding to the different Scenario 2 snapshots: X-point formation (XPF), Start of Heating(SOH), the Start of Flattop (SOF), End of Flattop (EOF), End Of Cooling(EOC) and End of Currents in the PF coils (EOC) [51]. 35
Figure 3.4	Poloidal cross-section of the JT-60SA plasma at the Start of the Flat Top (SOF) for reference Scenario 2. At SOF, the nominal plasma current is 5.5 MA, while the nominal values for poloidal beta β_p and internal inductance l_i are 0.53 and 0.85, respectively. 36
Figure 3.5	Poloidal cross-section of the JT-60SA plasma at the Start of the Flat Top (SOF) for reference Scenario 2. At SOF, the nominal plasma current is 5.5 MA, while the nominal values for poloidal beta β_p and internal inductance l_i are 0.53 and 0.85, respectively. In this figure the 85 gaps used to assess the plasma shape controller performance are shown. 37
Figure 3.6	SOF equilibrium reconstructed from CREATE-NL and the CCS code along with the magnetic field and flux sensors locations. 40
Figure 3.7	JT-60SA overall control scheme with the CREATE linearized model and the CCS LCFS reconstruction method using the XSC for an isoflux control approach. 42

- Figure 3.8 Isoflux control JT-60SA overall scheme with a block for the CREATE JT60-SA linearized model, a block for reconstructing the magnetic fluxes with the CCS method and the QST controller. 43
- Figure 3.9 Poloidal beta and internal inductance time traces for Disturbance #1 that models the expected disturbance soon after the plasma current flattop is reached (at $t \sim 20$ s), according to what has been considered in [62]. 44
- Figure 3.10 Poloidal beta and internal inductance time traces for Disturbance #2 that models the behavior of these variables due to the presence of a compound ELM as defined in [51]. 45
- Figure 3.11 Poloidal beta and internal inductance time traces for Disturbance #3 that models the behavior of these variables due to the presence of a Minor disruption as defined in [51]. 46
- Figure 3.12 Different choices for the set of controlled gaps used for gap controller. 47
- Figure 3.13 RMSE time traces for the different gaps selections in the presence of Disturbance #2 (compound ELMs). For all the considered cases, the RMSE is computed on the set of 85 gaps shown in figure 3.5. 47
- Figure 3.14 RMSE time traces for the different gaps selections in the presence of Disturbance #3 (Minor disruption). For all the considered cases, the RMSE is computed on the set of 85 gaps shown in Fig. 3.5. 48
- Figure 3.15 Comparison of the shape controller performance in the presence of Disturbance #3 (Minor disruption). The two cases of 8 and 20 gaps are considered. 49
- Figure 3.16 LCFS reconstructed by CREATE and the CCS code for the JT60-SA scenario 2 SOF equilibrium with a Minor disruption at steady-state for the three considered selection of control segments using the XSC with an isoflux approach. 50
- Figure 3.17 CREATE-NL JT60-SA Scenario 2 - SOF equilibrium compared with the LCFS reconstructed by the CCS method for 8 control points in the presence of a Minor disruption at steady-state using both the XSC and the QST control. 52
- Figure 3.18 CREATE-NL JT60-SA Scenario 2 - SOF equilibrium compared with the LCFS reconstructed by the CCS method for 8 control points in the presence of a Minor disruption (Disturbance #3) at the time of maximum deviation for both cases. As shown in figure 3.11, the disturbance occurs at $t \sim 20$ s 53
- Figure 3.19 Comparison between the flux at the X-point and the fluxes in the 8 control points reconstructed by the CCS method, when a Minor disruption is applied at $t=20$ s using the XSC and the QST controller. It should be noticed that QST control has a faster performance to reach the steady-state and less error. 53

List of Figures

- Figure 3.20 Flux errors for the case of 8 control points in the presence of a Minor disruption using the XSC and the QST controller. Even though both controllers reject the disturbance, is possible to remark how the QST control has an overall smaller error. 54
- Figure 3.21 XSC isoflux response to a change of shape request. The dashed black shape is the starting shape, while the red one is the target shape. The magenta dashed shape is the LCFS at steady state. 54
- Figure 3.22 Comparison between the flux at the X-point and the fluxes a 55
- Figure 3.23 Flux control error for the case of 8 control points for a change in the shape reference between 20 and 21.5 s. 55
- Figure 4.1 ISTTOK top view in 2020, main elements are indicated with magenta lines. 58
- Figure 4.2 ISTTOK frontal view in 2020, main elements are indicated with blue lines. 59
- Figure 4.3 Actual ISTTOK inconel vacuum vessel section with ports. 59
- Figure 4.4 ISTTOK magnetic probes. 61
- Figure 4.5 LEM transducer for measuring the current from the power supplies to the PF coils. 61
- Figure 4.6 ISTTOK close up side views. 62
- Figure 4.7 3D model of the ISTTOK PF coils, vacuum chamber with ports, iron core and the former central solenoid (black color). Primary coils (white color) and horizontal coils (green color) are formed by 2 coils each one and located on the upper and lower LFS (Low Field Side) of tokamak. Vertical coils (yellow color) are formed by 4 coils, 2 are located on the upper and lower LFS and 2 in the upper and lower HFS (High Field Side). 63
- Figure 4.8 Magnetic field generated by the active coil circuits on their nominal positions. Mirnov positions are represented by its sequential number (in red) over the dashed line. Black circle represents the limiter. 63
- Figure 4.9 ISTTOK hardware overall scheme. Data is acquired by the ATCA data acquisition boards, and decimated and transferred to the hosts every 100 μ s. 64
- Figure 4.10 General view of the ATCA-MIMO-ISOL carrier board, including on the right side an original IPFN RTM board joined through an edge connector. 65
- Figure 4.11 ADC module diagram depicting the influence of the WO and EO offsets and the instrumentation since the magnetic probes signal it is acquired until its integration in the FPGA. 66
- Figure 4.12 WO percentage change in the magnetic probe # 10 in 2019 using data from approximately 180 shots distributed during the entire year. 67
- Figure 4.13 WO and percentage change in the magnetic probe #4 throughout 45 shots in ISTTOK. 68

Figure 4.14	Real-time subtraction from the integrated WO is performed on every MARTe cycle for each magnetic probe.	68
Figure 4.15	Fig. 4.15a Response of the integrated and offset corrected signal in shot #44480 from magnetic probe #3 (red) used for obtaining data-driven models of the external fluxes. Reconstruction of the experimental signal through the data-driven model is shown in black. Fig. 4.15b Response of the magnetic probe #3 (orange) to a plasma-less discharge (shot #44632) with different current waveforms in the PF coils. Post-process reconstruction of the signal probe using the models already obtained is shown in orange.	70
Figure 4.16	Fig. 4.16a: ISTTOK Poloidal Cross Section with depiction of the radial and poloidal positions of the selected filaments for the plasma modelling and the magnetic probes. Fig. 4.16b: Comparison between magnetic probes measurements (blue line) and reconstructed values (orange line) during a plasma current positive Flat-top.	71
Figure 4.17	Comparison between the plasma current signal computed with Ampere's law and with the filamentary currents sum.	72
Figure 4.18	Real-Time reconstruction of the external fluxes contribution to the magnetic probes, this plot corresponds to the time trace of the magnetic probe # 3.	73
Figure 4.19	Real-Time reconstruction during a plasma flat-top of the external fluxes and its subtraction from the magnetic probe signal.	73
Figure 4.20	Comparison of the magnetic probe # 1 signal without the contribution of the external fluxes and its real-Time SVD reconstruction over the course of an AC Plasma discharge	74
Figure 4.21	Real-time reconstruction of the vertical and horizontal current centroid position and plasma current assisted by the magnetic probes signal acquisition and post-processing of two plasma discharges. Left column shows the resulting signals when the discharge control feedback is performed using Langmuir probes and right column shows when using Magnetic probes signals. Negative plasma cycles are lost when using Langmuir probes signals.	75
Figure 5.1	ISTTOK MARTe overall control position scheme.	78
Figure 5.2	Model response for two different $I_p \approx 4 \text{ kA}$ discharges.	80
Figure 5.3	Model response for two $I_p \approx -4 \text{ kA}$ discharges.	80
Figure 5.4	Comparison of the real-time Kalman filter retrieved centroid position and the multi-filament reconstruction time trace for $I_p > 0$.	81
Figure 5.5	Comparison of the real-time Kalman filter retrieved centroid position and the multi-filament reconstruction time trace for $I_p < 0$	82

List of Figures

- Figure 5.6 The matrix exponential defines a conformal map on the complex plane, mapping stable eigenvalues in the left half plane for continuous systems into eigenvalues inside the unit circle for discrete [82, Chapter 8]. 83
- Figure 5.7 Response to a unit step input from a non-minimum phase system [87]. 83
- Figure 5.8 Pole-zero maps in closed loop for the model when $I_p \approx 4kA$. Superposition of poles and zeros can be seen in the four transfer functions. 84
- Figure 5.9 Zoom to the stability border of the pole-zero maps in closed loop for the model when $I_p \approx 4kA$. 84
- Figure 5.10 Pole-zero maps in open loop for the model when $I_p \approx 4kA$. Superposition of poles and zeros can be seen in the four transfer functions. 85
- Figure 5.11 Zoom to the stability border of the pole-zero maps in open loop for the model when $I_p \approx 4kA$. 85
- Figure 5.12 Pole-zero maps in closed loop for the model when $I_p \approx -4kA$. Superposition of poles and zeros can be seen in the four transfer functions. In the transfer function $H_2(z)$ should be noticed the zero far from the unitary circumference. 86
- Figure 5.13 Zoom to the stability border of the pole-zero maps in closed loop for the model when $I_p \approx -4kA$. 86
- Figure 5.14 Pole-zero maps in open loop for the model when $I_p \approx -4kA$. Superposition of poles and zeros can be seen in the four transfer functions. In the transfer function $H_2(z)$ should be noticed the zero far from the unitary circumference. 87
- Figure 5.15 Zoom to the stability border of the pole-zero maps in open loop for the model when $I_p \approx -4kA$. 87
- Figure 5.16 Horizontal and vertical plasma centroid position during $I_p \approx 4kA$ flat-tops, blue time trace corresponds to a PID feedback control and orange time trace to a LQR MIMO feedback control, the dashed black line shows the programmed set point. The green vertical line marks the time when the discharge Shot#48324 switches from PID to MIMO LQR control. 89
- Figure 5.17 Horizontal and vertical plasma centroid position during $I_p \approx 4kA$ flat-tops, blue time trace corresponds to a PID feedback control and orange time trace to a LQR MIMO feedback control, the dashed black line shows the programmed set point. 90
- Figure 5.18 Vertical and Horizontal PF coils currents during $I_p \approx -4kA$ flat-tops, blue time trace corresponds to a PID feedback control and orange time trace to a LQR MIMO feedback control. The green vertical line marks the time when the discharge Shot#48324 switches the control from PID to MIMO LQR. 92

- Figure 5.19 Vertical and Horizontal PF coils currents during $I_p \approx 4kA$ flat-tops, blue time trace corresponds to a PID feedback control and orange time trace to a LQR MIMO feedback control. 93
- Figure A.1 Horizontal and vertical plasma centroid position during $I_p \approx 4kA$ flat-tops, blue time trace corresponds to a PID feedback control and orange time trace to a LQR MIMO feedback control, the dashed black line shows the programmed set point. Shot# 48563 and Shot# 48561. 105
- Figure A.2 Vertical and Horizontal PF coils currents during $I_p \approx 4kA$ flat-tops, blue time trace corresponds to a PID feedback control and orange time trace to a LQR MIMO feedback control. Shot # 48563 and Shot # 48561. 106
- Figure A.3 Horizontal and vertical plasma centroid position during $I_p \approx 4kA$ flat-tops, blue time trace corresponds to a PID feedback control and orange time trace to a LQR MIMO feedback control, the dashed black line shows the programmed set point. Shot # 48556 and Shot # 48555. 106
- Figure A.4 Vertical and Horizontal PF coils currents during $I_p \approx 4kA$ flat-tops, blue time trace corresponds to a PID feedback control and orange time trace to a LQR MIMO feedback control. Shot# 48556 and Shot# 48555. 107
- Figure A.5 Horizontal and vertical plasma centroid position during $I_p \approx 4kA$ flat-tops, blue time trace corresponds to a PID feedback control and orange time trace to a LQR MIMO feedback control, the dashed black line shows the programmed set point. Shot# 48551 Shot# 48554. 107
- Figure A.6 Vertical and Horizontal PF coils currents during $I_p \approx 4kA$ flat-tops, blue time trace corresponds to a PID feedback control and orange time trace to a LQR MIMO feedback control. Shot# 48551 and Shot# 48554. 108
- Figure A.7 Horizontal and vertical plasma centroid position during $I_p \approx 4kA$ flat-tops, blue time trace corresponds to a PID feedback control and orange time trace to a LQR MIMO feedback control, the dashed black line shows the programmed set point. Shot# 48515 and Shot# 48541. 108
- Figure A.8 Vertical and Horizontal PF coils currents during $I_p \approx 4kA$ flat-tops, blue time trace corresponds to a PID feedback control and orange time trace to a LQR MIMO feedback control. Shot# 48515 and Shot# 48541. 109
- Figure A.9 Horizontal and vertical plasma centroid position during $I_p \approx 4kA$ flat-tops, blue time trace corresponds to a PID feedback control and orange time trace to a LQR MIMO feedback control, the dashed black line shows the programmed set point. Shot# 48544 and Shot# 48542. 109

List of Figures

- Figure A.10 Vertical and Horizontal PF coils currents during $I_p \approx 4kA$ flat-tops, blue time trace corresponds to a PID feedback control and orange time trace to a LQR MIMO feedback control. Shot # 48544 and Shot# 48542. 110
- Figure A.11 Horizontal and vertical plasma centroid position during $I_p \approx 4kA$ flat-tops, blue time trace corresponds to a PID feedback control and orange time trace to a LQR MIMO feedback control, the dashed black line shows the programmed set point. Shot# 48546 and Shot#48548. 110
- Figure A.12 Vertical and Horizontal PF coils currents during $I_p \approx 4kA$ flat-tops, blue time trace corresponds to a PID feedback control and orange time trace to a LQR MIMO feedback control. Shot # 48546 and Shot# 48548. 111
- Figure A.13 Horizontal and vertical plasma centroid position during $I_p \approx 4kA$ flat-tops, blue time trace corresponds to a PID feedback control and orange time trace to a LQR MIMO feedback control, the dashed black line shows the programmed set point. The green vertical line marks the time when the discharge Shot# 48338 switches from PID to MIMO LQR control. 111
- Figure A.14 Vertical and Horizontal PF coils currents during $I_p \approx -4kA$ flat-tops, blue time trace corresponds to a PID feedback control and orange time trace to a LQR MIMO feedback control. The green vertical line marks the time when the discharge Shot#48338 switches the control from PID to MIMO LQR. Shot# 48340 and Shot# 48338. 112
- Figure A.15 Horizontal and vertical plasma centroid position during $I_p \approx 4kA$ flat-tops, blue time trace corresponds to a PID feedback control and orange time trace to a LQR MIMO feedback control, the dashed black line shows the programmed set point. The green vertical line marks the time when the discharge Shot# 48342 switches from PID to MIMO LQR control. 112
- Figure A.16 Vertical and Horizontal PF coils currents during $I_p \approx -4kA$ flat-tops, blue time trace corresponds to a PID feedback control and orange time trace to a LQR MIMO feedback control. The green vertical line marks the time when the discharge Shot#48342 switches the control from PID to MIMO LQR. Shot # 48343 and Shot# 48342. 113
- Figure A.17 Horizontal and vertical plasma centroid position during $I_p \approx 4kA$ flat-tops, blue time trace corresponds to a PID feedback control and orange time trace to a LQR MIMO feedback control, the dashed black line shows the programmed set point. The green vertical line marks the time when the discharge Shot# 48345 switches from PID to MIMO LQR control. 113

- Figure A.18 Vertical and Horizontal PF coils currents during $I_p \approx -4kA$ flat-tops, blue time trace corresponds to a PID feedback control and orange time trace to a LQR MIMO feedback control. The green vertical line marks the time when the discharge Shot#48345 switches the control from PID to MIMO LQR. Shot# 48346 and Shot# 48345. 114
- Figure A.19 Horizontal and vertical plasma centroid position during $I_p \approx 4kA$ flat-tops, blue time trace corresponds to a PID feedback control and orange time trace to a LQR MIMO feedback control, the dashed black line shows the programmed set point. The green vertical line marks the time when the discharge Shot# 48348 switches from PID to MIMO LQR control. 114
- Figure A.20 Vertical and Horizontal PF coils currents during $I_p \approx -4kA$ flat-tops, blue time trace corresponds to a PID feedback control and orange time trace to a LQR MIMO feedback control. The green vertical line marks the time when the discharge Shot#48348 switches the control from PID to MIMO LQR. Shot# 48349 and Shot# 48348 115
- Figure A.21 Horizontal and vertical plasma centroid position during $I_p \approx 4kA$ flat-tops, blue time trace corresponds to a PID feedback control and orange time trace to a LQR MIMO feedback control, the dashed black line shows the programmed set point. The green vertical line marks the time when the discharge Shot# 48354 switches from PID to MIMO LQR control. 115
- Figure A.22 Vertical and Horizontal PF coils currents during $I_p \approx -4kA$ flat-tops, blue time trace corresponds to a PID feedback control and orange time trace to a LQR MIMO feedback control. The green vertical line marks the time when the discharge Shot#48354 switches the control from PID to MIMO LQR. Shot# 48352 and Shot# 48354. 116
- Figure A.23 Horizontal and vertical plasma centroid position during $I_p \approx 4kA$ flat-tops, blue time trace corresponds to a PID feedback control and orange time trace to a LQR MIMO feedback control, the dashed black line shows the programmed set point. The green vertical line marks the time when the discharge Shot# 48350 switches from PID to MIMO LQR control. 116
- Figure A.24 Vertical and Horizontal PF coils currents during $I_p \approx -4kA$ flat-tops, blue time trace corresponds to a PID feedback control and orange time trace to a LQR MIMO feedback control. The green vertical line marks the time when the discharge Shot#48350 switches the control from PID to MIMO LQR. Shot# 48351 and Shot# 48350. 117
- Figure B.1 JT60-SA assembly when the cryostat top part was installed, 2018. 119
- Figure B.2 JT60-SA assembly in 2019.JT60-SA 120

List of Figures

- | | | |
|------------|--|-----|
| Figure B.3 | JT60-SA insertion of TF coil in 2018. | 120 |
| Figure B.4 | JT60-SA insertion of TF coil in 2018. | 121 |
| Figure B.5 | JT60-SA transportation of the first PF coil in 2019. | 122 |

LIST OF TABLES

Table 3.1	Steady-state RMSE values for the different choices of number of controlled gaps and for the different disturbances test cases.	45
Table 3.2	Steady-state flux RMSE values for the different selection of control points for the JT60-SA scenario 2, SOF equilibrium in the presence of Disturbance #1 at $t \sim 20$ s.	49
Table 3.3	X-point position steady state error for JT60-SA scenario 2, SOF equilibrium in the presence of Disturbance #1 at $t \sim 20$ s. The XSC and QST controller were used in different simulations for the shape control along with two reconstruction methods for the LCFS.	50
Table 3.4	Steady-state flux RMSE values for the different selection of control points for the JT60-SA scenario 2, SOF equilibrium in the presence of Disturbance #2 (Compound ELM) at $t \sim 20$ s.	51
Table 3.5	X-point position steady state error for JT60-SA scenario 2, SOF equilibrium in the presence of Disturbance #2 (Compound ELM) at $t \sim 20$ s. The XSC and QST controller were used in different simulations for the shape control along with two reconstruction methods for the LCFS.	51
Table 3.6	Steady-state flux RMSE values for the different selection of control points for the JT60-SA scenario 2, SOF equilibrium in the presence of Disturbance #3 (Minor disruption) at $t \sim 20$ s.	51
Table 3.7	X-point position steady state error for JT60-SA scenario 2, SOF equilibrium in the presence of Disturbance #3 (Minor disruption) at $t \sim 20$ s. The XSC and QST controller were used in different simulations for the shape control along with two reconstruction methods for the LCFS.	51
Table 5.1	Centroid position RMSE comparison between PID and MIMO-LQR controlled discharges for different set points and plasma current scenarios.	91

LIST OF ABBREVIATIONS

- AC - Alternating Current
- ADC - Analog to Digital Converter
- ATCA - Advanced Telecommunications Computing Architecture
- CCS- Couchy Condition Surface
- CREATE - Consorzio di Ricerca per l'Energia, l'Automazione e le Tecnologie dell'Elettromagnetismo
- DDB - Dynamic Data Buffer
- DAC - Digital to Analog Converter
- EFIT - Equilibrium Fitting
- ELM - Edge Localized Mode
- EO - Electronic Offset
- GAM - Generic Application Module
- IST - Instituto Superior Técnico
- IPFN - Insituto de Plasmas e Fusão Nuclear
- JET - Joint European Torus
- LCFS- Last Closed Flux Surface
- LQR - Linear Quadratic Regulator
- MARTe - Multi-threaded Application Real-Time executor
- MIMO - Multiple-Input Multiple-Output
- ODE- Ordinary differential equations
- PCS - Plasma Control System
- PF - Poloidal Field
- PID - Proportional - Integrative - Derivative
- QST - National Institutes for Quantum and Radiological Science and Technology

List of Abbreviations

- RAPTOR - RApid Plasma Transport simulatOR
- RFM - Reflective Memory
- RMSE - Root Mean Squared Error
- SISO- Single-Input Single-Output
- SCD - Systéme de Contrôle Distribué
- SVD -Singular Value Decomposition
- SOF - Start Of Flattop
- XSC - eXtreme Shape Controller
- WO - Wiring Offset

LIST OF VARIABLES

@TODO: Review variable lists as writing the thesis

VARIABLES:

- B_θ - Poloidal magnetic field
- B_ϕ - Toroidal magnetic field
- μ_0 - Vacuum permeability
- β_p - Poloidal beta
- I_p - Plasma current
- l_i - Internal inductance
- I_{PF} - Poloidal Field coils current
- $x(t), x[k]$ - State-space vector

I

INTRODUCTION

What is a fusion plasma and why is it magnetically confined for nuclear fusion devices?

A fusion plasma is a fully ionized gas whose behavior is dominated by long-range electric and magnetic fields. A major consequence of this behavior is that a plasma is an exceptionally good conductor of electricity, its conductivity implies that the plasma inside is shielded from DC electric fields \bar{E} to a very large degree. On the other hand, DC magnetic fields \bar{B} can penetrate and it is these fields that provide plasma confinement, hence the name "magnetic confinement" [1, Chapter 6].

Why do we need magnetic fields in nuclear fusion devices ?

Magnetic fields are needed to confine the hot plasma and keep it away from the machine walls. In a generic magnetic fusion reactor the basic properties of magnetic fields require a toroidal geometry so it can hold the plasma equilibrium [1, Chapter 4]. The properties of the magnetic fields require a toroidal geometry for confining magnetically the plasma. Trajectories of particles in the presence of magnetic fields are described by the Lorentz force equation $m\frac{d\vec{v}}{dt} = q(\bar{E} + \vec{v} \times \bar{B})$, where $\frac{d\vec{r}}{dt} = \vec{v}$, the combined perpendicular and parallel motion of a charged particle corresponds to a helical trajectory as depicted in figure 1.1. If particles stream in a cylindrical device, they would collide with the wall due to the motion of the particles, a magnetic device whose lines are wrapped around a toroidal shape prevent free streaming end loss, making obvious why the magnetic geometry for confining the plasma has to be toroidal.

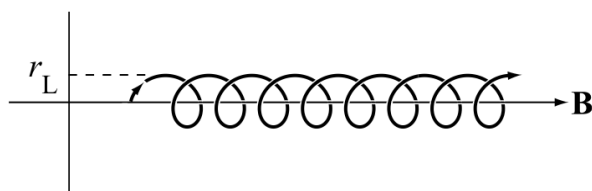


Figure 1.1.: Helical trajectory of a charged particle in a uniform magnetic field [1, Chapter 8].

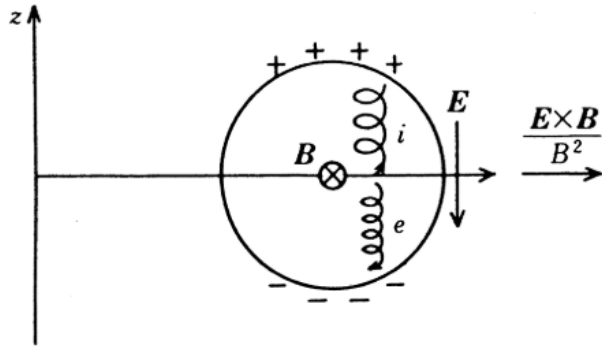


Figure 1.2.: Toroidal drift, particles drift in the vertical direction. [2, Chapter 3]

1.1 BEHIND THE PLASMA CURRENT

Considering the drift of guiding center of a charged particle in a simple toroidal field in cylindrical coordinates (R, φ, z) . The component of the magnetic field B_φ is the toroidal field and it decreases in the form of $1/R$ outward. The magnetic lines of force are circles around z axis. Particles in this torus run fast in the toroidal direction and drift slowly in the z direction as shown in figure 1.2, this drift is called toroidal drift. As a consequence using only a toroidal component of magnetic field is not sufficient for confining the plasma inside a toroidal device or tokamak since particles drift and therefore will cause a loss of confinement [2, Chapter 3].

If a current is induced in a toroidal plasma, the component of magnetic field around the magnetic axis (which is also called minor axis) is introduced. This component B_p is called poloidal magnetic field and has components in (R, z) . The addition of this field creates magnetic lines circling the major axis of the torus, thus the particles circulate through the force lines. These lines cross a certain cross-section P of the torus, each time the lines cross the plane P , the crossing point rotates around the minor axis by a certain angle ι which is called "rotational transform angle", this is shown in figure 1.3. The combination of toroidal and poloidal magnetic fields avoids the drift described before originated by having an only-toroidal magnetic field by the introduction of the rotational transform angle. The poloidal field in a tokamak is mainly produced by the induced plasma toroidal current.

All toroidally confined plasmas experience outward toroidal forces along the R direction, the first one is called the "hoop force" and is analogous to the outward expansion force generated by the current flowing in a circular loop of wire, for this case this force corresponds to the toroidal current flowing in the plasma or simply called plasma current I_p . The second force is called " $1/R$ force" and its name comes from the $1/R$ dependence of the toroidal field resulting from the toroidal geometry, the applied toroidal field $B_{\varphi a}$, where a is the minor radius of the tokamak or the distance from the center of the vacuum chamber to the wall, has a $1/R$ dependence which follows from integrating Ampere's law around any closed toroidal loop located between the toroidal coils and the plasma. Finally the third one is called

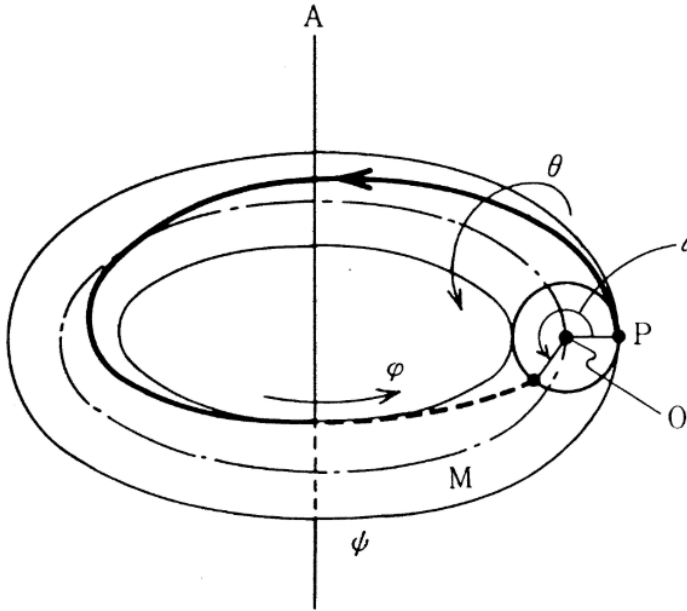


Figure 1.3.: Rotational transform angle ι formed when the magnetic force lines generated by the combination of toroidal and poloidal field cross the plane P in different points [2, Chapter 3].

"tire tube force" and its existence is related to the difference of plasma pressures created by the toroidal geometry [1, Chapter 11].

Given these outward toroidal forces, somehow the toroidal force balance must be establish before the plasma hits the walls. An inwardly pointing restoring force is required and it is apply by means of the external poloidal field (PF) coils which generate a vertical field in order to compensate the radial forces generated by the tokamak. By choosing the magnitude and sign of the vertical field correctly, one can produce an inward restoring force to produce toroidal force balance. In order to make an analytic deviation of the toroidal force balance a simple model for the magnetic fields is used, this model consists of a toroidal plasma whose contours of constant pressure are a set of nested concentric circles $p = p(r)$, where r is the minor radius coordinate as shown in figure 1.4. The simplified version of the pressure and magnetic fields to be used in the determination of the toroidal force balance are:

$$\begin{aligned} p &= p(r) \\ B &= \frac{R_0}{R} B_\phi(r) \hat{\phi} + \frac{R_0}{R} B_\theta(r) \hat{\theta} + B_v \hat{z} \end{aligned} \tag{1.1}$$

where R_0 is the tokamak major radius or the distance from the center of the torus to the center of the chamber (see figure 1.4), B_θ is the poloidal field and B_v the external vertical field generated by the PF coils. After substituting the expression for the magnetic field into the general MHD force balance equation or the so-called Grad-Shafranov equation ([2, Chapter 6], [1, Chapter 11], [3, Chpater 2]), the expression for the toroidal force balance can be obtained.

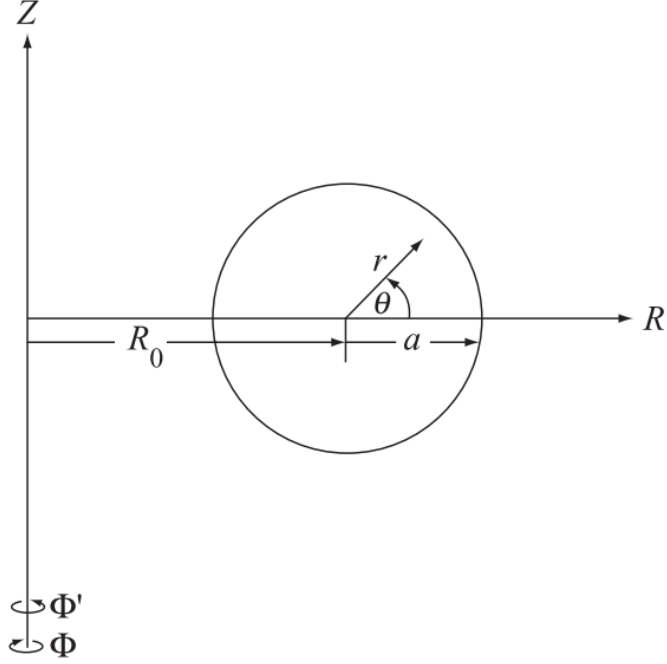


Figure 1.4.: Toroidal geometry and variables used for the calculations of the toroidal force balance and the vertical field [1, Chapter 11].

The toroidal force balance establishes the forces equation $F_{hoop} + F_{1/R} + F_{tube} + F_v = 0$, where F_v is the force generated by the external vertical field. Thus, the hoop force is given by:

$$F_{hoop} = 2\pi^2 a^2 (li + le + 2) \frac{B_{\theta a}^2}{2\mu_0} \quad (1.2)$$

where le and li are the external and internal normalized inductances, $l = (L/2\pi R_0)/(\mu_0/4\pi)$. The "1/R" force is established as:

$$F_{1/R} = 2\pi^2 a^2 \left(\frac{B_{\phi a}^2}{2\mu_0} - \frac{\langle B_\phi^2 \rangle}{2\mu_0} \right) \quad (1.3)$$

where $\langle B_\phi^2 \rangle$ is the toroidal field average. The "tire tube" force is given by:

$$F_{tube} = 2\pi^2 a^2 \langle p \rangle \quad (1.4)$$

and finally the external vertical force is:

$$F_v = -2\pi^2 a^2 \left(\frac{2R_0 B_v B_{\theta a}}{a\mu_0} \right) \quad (1.5)$$

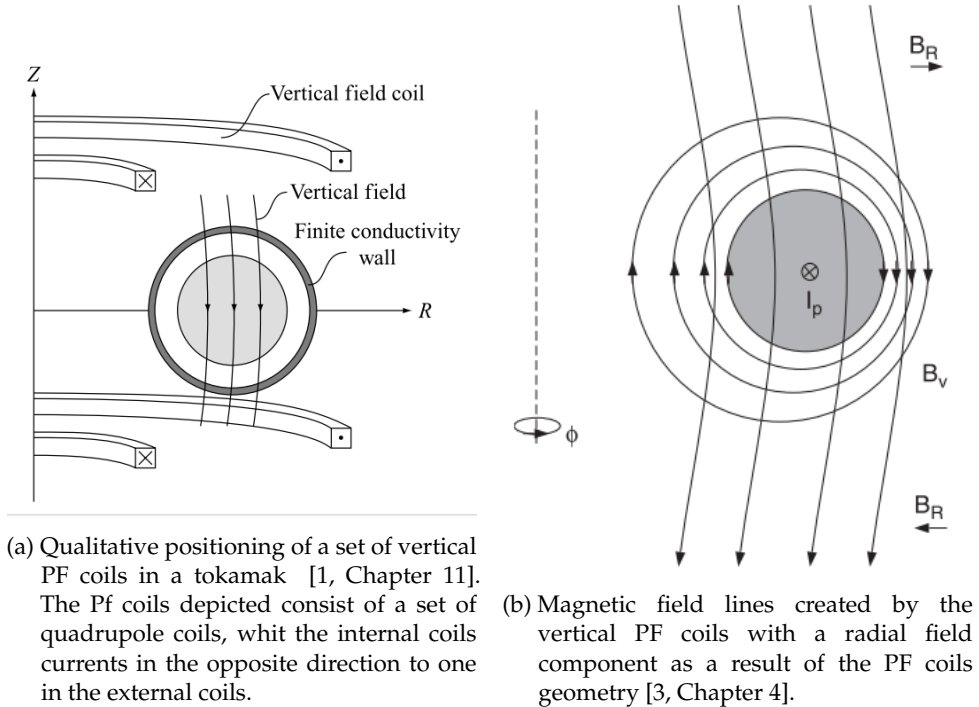


Figure 1.5.: PF vertical coils and magnetic field lines.

where B_v is the external vertical magnetic field. Doing the combination of the 4 forces into the forces equation, the required vertical field for toroidal force balance remains:

$$B_v = B_{\theta a} \frac{a}{4R_0} \left[\frac{2\mu_0 \langle p \rangle}{B_{\theta a}^2} + \frac{B_{\phi a}^2 - \langle B_\phi^2 \rangle}{B_{\theta a}^2} + li + le + 2 \right] \quad (1.6)$$

B_v is the necessary vertical external field in order to avoid the plasma moving outwardly and touch the chamber walls, this equation will be addressed in chapter 4. In a purely vertical field, the plasma does not experience a vertical force and the vertical plasma current position is not well defined [3, Chapter 4]. Due to the form that the PF coils are positioned around the vessel the field produced by them is not completely vertical generating thus a radial component of external magnetic field. Due to Lorentz force law the radial component of the external field causes a vertical displacement of the plasma, this is compensated by adding another set of PF coils which generates an horizontal magnetic field. Figures 1.5 show the field lines created by the vertical PF coils and its geometrical configuration surrounding the vacuum chamber.

1.2 PLASMA CONTROL IN TOKAMAKS

Tokamaks are devices with an axisymmetric configuration with a large toroidal magnetic field and a DC toroidal current or plasma current I_p , given its physical characteristics and its performance until now is presently the leading candidate to become the world's first fusion reactor. During the start up

and subsequent approximately steady state phase of many fusion plasma discharges a toroidal current is induced in the plasma by means of transformer action with the plasma being the secondary of the transformer [1, Chapter 9]. Sometimes the PF coils means both the equilibrium field coils and the ohmic heating coils. By raising the current of the primary windings of the current transformer (ohmic heating coils), a current is induced in the plasma, which acts as the secondary winding, for example at the ISTTOK tokamak the plasma is heated by the ohmic heating coils which also generate a vertical magnetic field [2, Chapter 16].

Typical operation of a tokamak discharge starts with the establishment of a large, steady, toroidal, magnetic field¹. Next, neutral gas is injected into the vacuum chamber and often pre-ionized. The transformer induced the plasma current I_p which is then ramped up to its maximum value and maintained for the “flat top” portion of the pulse [1, Chapter 13]. Since currently tokamaks have a plasma pulsed nature of some ms or s, in the case of bigger devices, it is easy to acquire a large volume of data over short periods and archived it after the plasma discharge or even during the plasma discharge, data acquisition and storage of signals in tokamaks is vitally important since the collected data us use for modeling the plasma, study instabilities and develop new codes and algorithms.

Usually tokamak control tends to reefer to the control of the plasma itself, the supervisory plant control is conventional and normally uses industrial equipment. Control engineering for magnetic confined plasmas embrace different types of techniques and they are use for controlling the physical variables existing on the device and the plasma. The tokamak control problems can be separated into two major classes: electromagnetic control and plasma kinetic control. Electromagnetic control refers to controlling the magnetic and electric fields and kinetic control refers to controlling particle feed rates and heating to modify the plasma density, temperature, pressure and current density [4, Chapter 1]. One of the main tasks of control engineering in the field of fusion is to maintain the plasma in certain position and shape in such way that it stays stable, follows set points and rejects possible instabilities which may occur maintaining a constant plasma current.

Early tokamaks were quite primitive. The desired plasma parameters were obtained as a result of sets of pre-programmed power-supply or gas-valve commands, designed by trial and error. As technology tokamak began to develop and the plasma pulses duration became longer, feedback control loops were integrated to control simple parameters [5]. It is natural that one of the first parameters to be actively controlled in a tokamak was the plasma position since this would mean maintaining the hot plasma centered inside the vacuum vessel. As already explained in last section coupling between the plasma radial position and current control systems depends on the active PF coil system. Initially, research efforts concentrated on the radial position control of circular, vertically stable tokamak plasmas [4, Chapter 1]. By the end of the 1970’s, the advantages of forcing the tokamak plasma cross-section to be other than circular were being proposed on the basis of theoretical studies and the first plasmas with

¹ Tokamaks should have superconductive toroidal coils since they do not dissipate power in steady state and require only a small amount os cooling power [1, Chapter 5].

vertically elongated cross-sections were created. These elongated plasmas are inherently unstable but this fact contributed to master the shape plasma control.

1.3 THESIS OUTLINE

This thesis will study the properties and control applications for two tokamaks: JT60-SA and ISTTOK. These tokamaks possess physical characteristics which vary in big scale between them: the size, ISTTOK has a cross-circular section and JT60-SA is a diverted plasma, the dimension of the magnetic fields and plasma current, ISTTOK has 30 years operating and JT60-SA will start operations in late 2020, etc. Despite these facts there exist a big reason to join the two machines in a single work: both tokamaks rely on active magnetic control applied to the PF coils in order to control the plasma position and shape. Beyond that, both use active magnetic control for the plasma position, also in this work for both tokamaks control and modeling approaches relying in the same concepts are applied.

This work is divided in 5 chapters being this chapter the Introduction.

- Chapter 2 explores the plasma control systems implemented in different tokamaks around the world and addresses some important theoretical concepts to be applied in the further chapters.
- Chapter 3 addresses JT60-SA operation, its theoretical modeling and assessments for the shape and plasma current control.
- Chapter 4 presents the overall picture of ISTTOK tokamak: the geometry, the actuators and diagnostics. Following, the novel implemented reconstruction of the plasma current centroid position is addressed.
- Chapter 5 presents the experimental control results in ISTTOK after the implementation of two different control algorithms in the device.

The research done in this work is important and needed because it delves into topics crucial for tokamak operation. It asses control techniques for what will be the biggest operating tokamak (JT60-SA) and implements novelty algorithms in a small tokamak that probably would have not existed on the ISTTOK tokamak without the latest technology advances. The main objectives of this thesis are to encompass the implementation of plasma position controllers for two different devices demonstrating that despite the size or characteristics of a tokamak it relies in the same physics principles and control engineering tools.

2

PLASMA CONTROL SYSTEMS

2.1 OVERVIEW OF CONTROL SYSTEMS

The control of plasma position, shape and current among other parameters is one of the essential engineering problems for present and future magnetic confinement devices. The Plasma Control Systems (PCS) lead with the overall control of fusion devices being responsible also for the plasma configuration and scenarios algorithms [6, Chapter 8]. Even though this entire work mainly focuses on position and shape control it is also important to mention the relevance of density control for tokamak operation for the gas feeding feedback [7]. Industrial control systems in fusion devices like water cooling and power supply control usually are controlled outside the domain of the PCS. Currently different PCS's are used in the tokamaks around the world. In this chapter the "DIII-D-like" PCS, the Système de Contrôle Distribué (SCD) and the Multi-threaded Application Real-Time executor (MARTE) will be approached, this last one being of special interest due to its extensive utilization in this work, likewise this chapter presents an overview of the equilibrium and control algorithms used for the reconstruction of plasma parameters and the controllers used for position, shape and plasma current among other parameters.

2.1.1 *DIII-D Plasma Control System*

The DIII-D-like PCS is used in various fusion research facilities such as EAST (China), K-STAR (South Korea), NSTX (USA) and MAST (UK). Early documentation regarding the PCS in DIII-D¹ refers to digitalization of analog signals transmitted to a high speed processor executing a shape control algorithm and then writing the result to a digital to analog converter for driving the controlled systems. The real-time computer used allowed to perform operations with vectors and matrices required for the plasma shape control algorithm [8]. Figure 2.1 shows the block diagram of the DIII-D PCS 30 years ago.

In recent years the DIII-D PCS had extensive software and hardware upgrades. The PCS actual software consists of an infrastructure library core which provides all the routines that are necessary for implementing a basic and generic control system. The current PCS hardware configuration uses a collection of Intel Linux based multi-processor computers running in parallel to perform the real-

¹ DIII-D is a D-shape tokamak operated by General Atomics in San Diego, California.

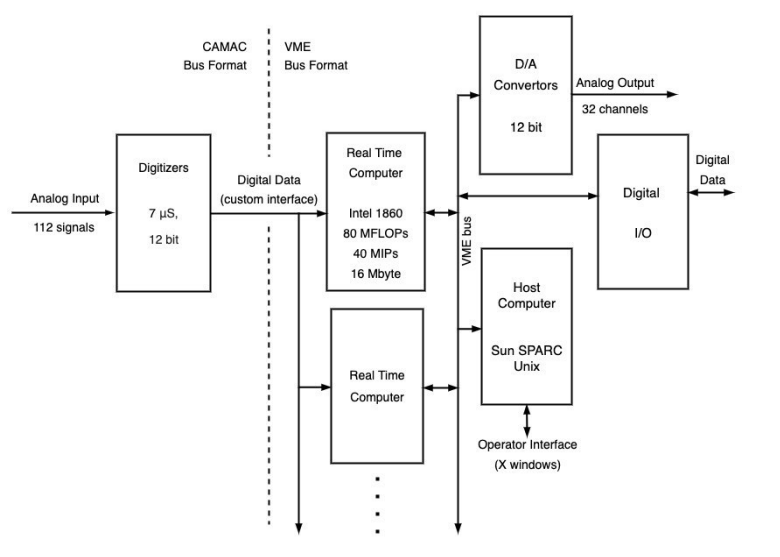


Figure 2.1.: DIII-D digital PCS in 1991 [8].

time analysis and feedback control [9]. New digitizers have been added to the real-time network to increase the number of signals acquired and to control hardware on real-time, several real-time control algorithms were added and real-time data was added to external entities such as web server. [10]. In the current version of the PCS, a Myricom² network has been replaced with a 40 Gb/sec InfiniBand³ network based on the Mellanox Connect-X 3⁴ hardware set. Figure 2.2 shows the currently overall networking diagram of DIII-D PCS .

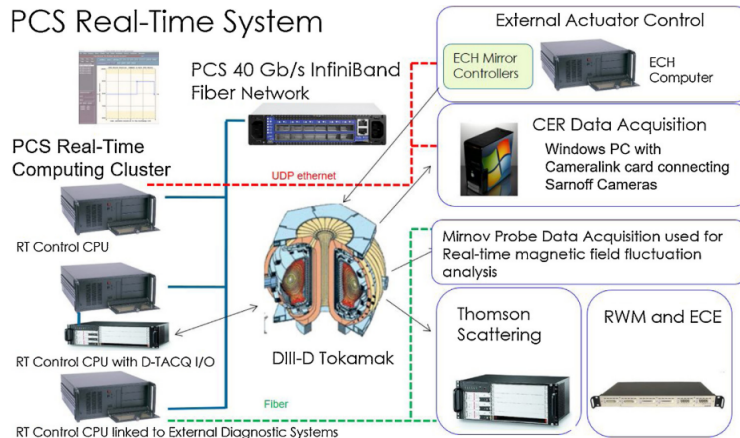


Figure 2.2.: Actual DIII-D PCS real-time systems [10].

² Myricom networks also called Myrnet are high speed networking systems used to interconnect machines to form computer clusters.

³ Is a network architecture from Mellanox designed to support I/O connectivity and reliability, availability, and serviceability Internet requirements [11].

⁴ The Connect-X from the Mellanox company are Ethernet network interface cards with PCI Express.

2.1.2 Système de Contrôle Distribué

The TCV⁵ distributed control system uses a modular network of real time PC nodes liken by a real time network to provide feedback control over all of the actuator systems. Each node consists of a Linux PC either embedded on a Compact-PCI module or as a desktop computer with Intel CPU. A fiber optic ring network links the reflective memory (RFM) network cards in each node [12]. The design of the diagnostic signal processing and control algorithms is performed in Matlab-Simulink software. During the real-time execution C/C++ code is generated from the Simulink and compiled into a Linux shared library and distributed to target nodes providing the input/output interface to the control algorithm code [13]. Figure 2.3 depicts the TCV SCD layout with the connectivity to diagnostics and actuators.

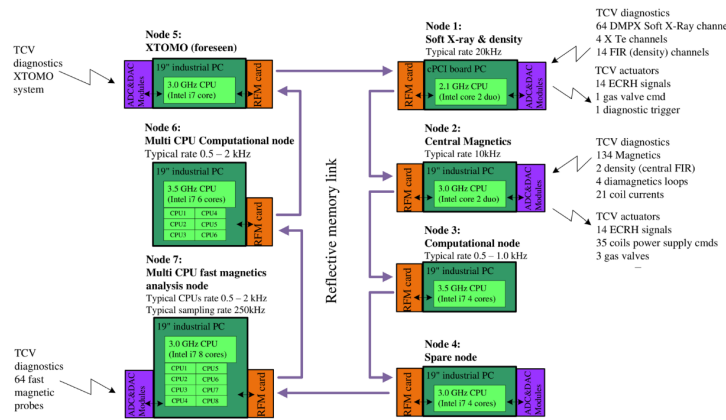


Figure 2.3.: TCV SCD. Real-time network nodes connection. The nodes configurations are shown together with the typical diagnostic and actuator systems to which they are connected [13].

2.2 MARTE FRAMEWORK

Regardless the nature of a real-time system, the design of it is usually related to the specific requirements it has, commonly this implies to have customized hardware and software which causes a lack in modularity and portability. When systems become bigger is convenient to provide a common library containing shareable functionalities and which also allows for modular implementations. In order to deal with this the MARTe framework was designed about a decade ago. MARTe was developed in order to standardize general real-time control systems for the execution of control algorithms and is based on a multiplatform C++ library [14]. Previous implementations for a software framework similar to MARTe were developed some years before for the JET tokamak. JETRT was a software framework used to develop real-time control and data acquisition systems which laid the foundation for current MARTe framework [15]. MARTe is currently used in several tokamaks such as JET, FTU, COMPASS and ISTTOK.

⁵ The Tokamak à configuration variable (TCV) is a medium size tokamak localized in Laussane, Switzerland. It is characterized by a highly elongated, rectangular vacuum vessel.

2.2.1 MARTe architecture

The unitary MARTe component is the Generic Application Module (GAM), each of the C++ programmed GAMs usually performs a specific task of the control system, the collection of interconnecting GAMs builds MARTe [16]. The GAMs have an entry point to receive data driven configuration and a set of input and output channels to interface with other GAMs. The Dynamic Data Buffer (DDB) is a generic memory data bus where each GAM receives and produce data using DDB named channels. Usually each GAM is associated with a special function of the system like processing data of an specific diagnostic or perform some control algorithm. MARTe hardware data interface and synchronization for inputs and outputs is performed using a special GAM called IOGAM.

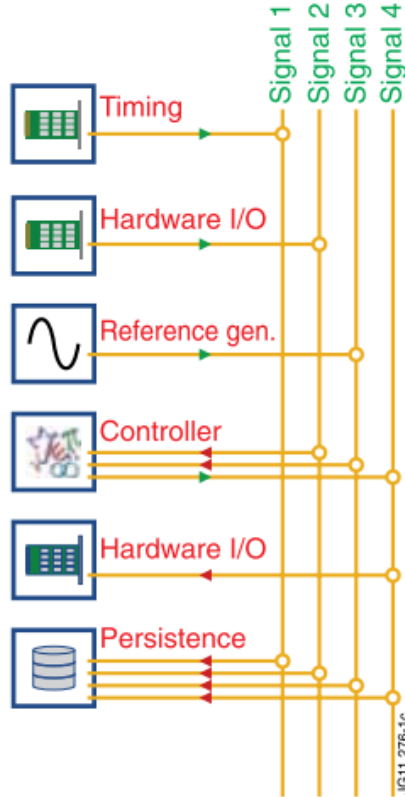


Figure 2.4.: Example of a set of GAMs connected to the DDB. Timing and hardware GAMs provide the I/O interface to the exterior, whereas a generic waveform GAM inputs the reference for a PID controller. Finally, the output is sent to a DAC and the data is stored for analysis by a collection GAM. It should be noticed that the reference generation and the controller GAM are not aware of the changes in the data providers and data consumers. [17]

2.2.2 MARTe hardware containers

This section will describe the hardware used altogether with the MARTe framework for the overall plasma control in different devices, specially the case for the JET, COMPASS and ISTTOK tokamaks.

Devices with the MARTE framework base their hardware on the Advanced Telecommunications Computing Architecture (ATCA) standard, which is the most promising architecture to substantially enhance the performance and capability of existing standard systems as it is designed to handle tasks such as event building, feature extraction and high-level trigger processing [18].

At JET the data acquisition system is based on the PICMG 3.0 ATCA standard and contains six data acquisition cards. Each board comprises 32 18-bit resolution analog-to-digital converters (ADC) acquiring at 2 Msamples/s. The cards are connected to the controller computer using the Peripheral Component Interconnect Express (PCIe) point-to-point links through the ATCA backplane [14], [19]. Data synchronization is performed in the master board, which is guaranteed by the firmware to be the latest to have data available. Once new data is available, it is collected and a new MARTE cycle starts. The CPU core isolation scheme allows to protect the real-time environment from spurious and undesired interrupt sources. Figure 2.5 depicts a roughly JET scheme of the acquisition boards and its connection to the MARTE framework.

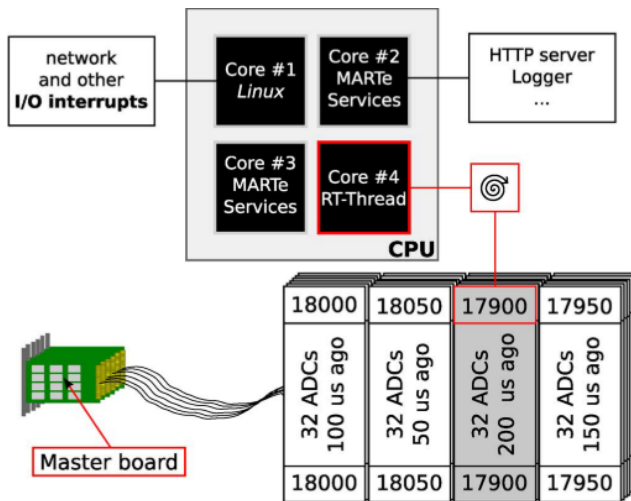


Figure 2.5.: JET ATCA hardware. The acquisition boards map in the controller computer memory a set of four buffers, the selected one is consecutively cycled every $50 \mu s$ by the firmware. The first value written is the header and contains the absolute time since the last trigger, followed by the acquired values of the ADCs, and finally by the footer containing the same value as the header. [14]

The hardware used in the ISTTOK real-time system is also based on the ATCA standard while the old architecture was based on the Peripheral Component Interconnect (PCI) standard. The ATCA acquisition boards are composed by 32 ADC modules connected to a Virtex-4 Field-programmable gate array (FPGA) that manages the data path from the ADC to the PCIe bus. Since ISTTOK has a noisy environment and the selected ADCs were able to acquire data at 2 Msample/s, it was decided to implement an additional digital filter in the FPGA to filter each ADC sample with a finite impulse response (FIR) filter [20]. Figure 2.6 shows a photograph of an ATCA board, each board contains 512 MBytes of DDR memory and an FPGA, which performs digital signal processing and includes a PCI Express communications interface, this boards are developed at the IPFN(Instituto de Plasmas e Fusão

Nuclear) where the ISTTOK tokamak is also located. Figure 2.7 shows an schematic example of how a tomography system installed at ISTTOK is connected to the ATCA boards.



Figure 2.6.: ATCA control board with 32 ADCs developed and assembled at the IPFN. [18]

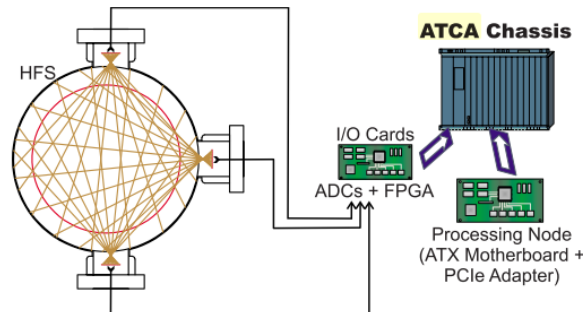


Figure 2.7.: The ISTTOK tomography system has 30 acquisition channels connected by an Input-Output ATCA card and sent to MARTe framework. [21]

For the Compass Tokamak, currently being installed in Prague, Czech Republic, its whole control and data acquisition system is being redesigned and built from scratch, based also on the ATCA standard. In total 14 ATCA boards (developed at IPFN) will be used with 32 ADCs each one. In order to guarantee real-time execution of the control codes a framework based on Linux and the Real-Time Application Interface (RTAI) will be used. This will explore the features provided by the new multi-core technologies [18]. Figure 2.8 shows an schematic of the new COMPASS system.

2.2.3 MARTe 2.0

Software Quality Assurance (QA)⁶ processes are being applied to the development of a new version of the MARTe framework also called MARTe 2.0. The main objective is to provide a QA certifiable

⁶ Software QA is a set of activities or processes that define and assess the adequacy of software processes to provide evidence that establishes confidence that the software processes are appropriate for and produce software products of suitable quality for their intended purposes [22, Chapter 5.1].

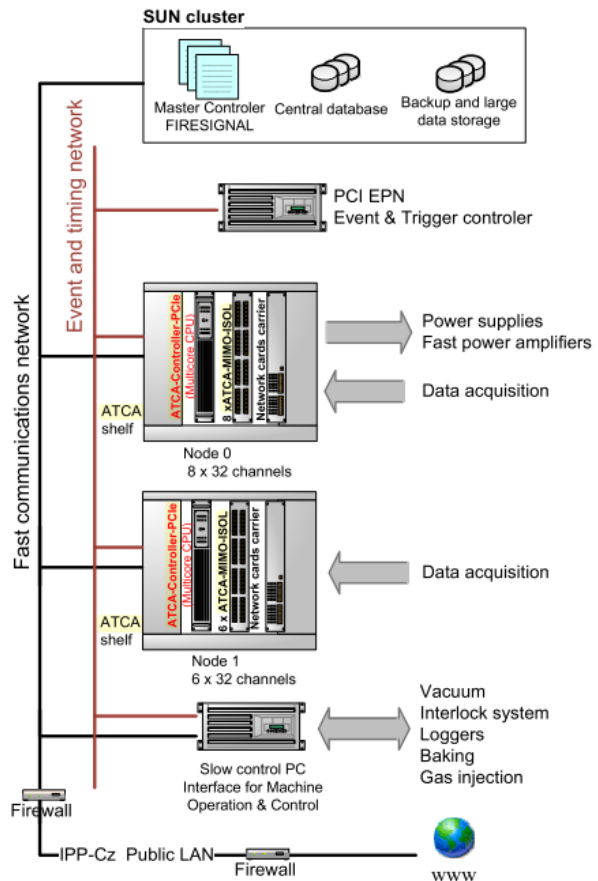


Figure 2.8.: Schematic of COMPASS tokamak control and data acquisition system, two ATCA systems are responsible for the fast control of the device and for the data acquisition. [18]

environment from where it is possible to develop, with less effort, certifiable applications. The MARTE QA version can be easily adapted to the development of many types of software which are common in the fusion community, in particular for software related to control and data acquisition systems that is to be shared among different teams [23]. MARTE 2.0 will be the result of reduction exercise of the core framework based on the lessons learned from MARTE. This version will incorporate and implement an integral quality assurance process for the development of the framework (e.g. unit tests and coding standard) [24].

In order to develop robust code and to avoid common errors and pitfalls, a controlled subset of the C++ language must be defined for the MARTE framework. This subset will be define by means of a list of coding rules, which will address all dangerous aspects of the C++ language for critical systems. Thus, the C++ version used on MARTE will be defined by the standard ISO/IEC 14882:2003 aka as C++03, while the coding rules will be those defined by the standard MISRA C++:2008 [25]. The MARTE project manager is responsible for appointing a quality office (QO) for the QA process. The QO will guarantee that the QA activities are executed accordingly to the software development process, it will also conduct independent reviews and audit all data and processes involving the development, production and maintenance of MARTE deliverables [26]. The overall advantage of the new MARTE version is that the common faced difficulties of distributing and maintaining a software without the continuous support of the original developers will be overcome following a complete QA system.

2.3 TOKAMAK EQUILIBRIUM CODES

Tokamak equilibrium codes are used for retrieving information about plasma current, shape and position and pressures profiles among other parameters. Usually these codes use as input data as the machine geometry, the PF coils currents and the flux and magnetic field diagnostics measurements. The importance of these codes is that since some of the parameters necessary for an accurate feedback control are not directly measured from the diagnostics, these data has to be fitted on real-time somehow to the Grad-Shafranov equilibrium model [27]. In this section some of the most implemented and reported codes for tokamak plasma equilibrium reconstruction will be briefly described.

The EFIT (Equilibrium Fitting) code is used to efficiently reconstruct the current profile parameters, the plasma shape and a current density profile satisfying the MHD equilibrium constraint based on a Picard iteration⁷ approach which approximately conserves the external magnetic measurements [28]. EFIT has served as the de-facto standard technique to infer equilibrium from experimental diagnostics and there have been many different code implementations of this technique, all EFIT versions are able to solve the MHD force balance and most experiment-specific customizations are made for the addition of experimental constraints peculiar to the experiment being modelled [29]. EFIT reconstruction code is used in tokamaks such as DIII-D and the National Spherical Torus Experiment (NSTX). For the specific

⁷ Picard iterations is a method based on successive approximations to obtained a set of conditions under which an initial value problem has a unique solution.

NSTX case they implemented a special real-time EFIT version called rtEFIT developed at General Atomics, the rtEFIT code provides the shape of the plasma boundary that is used as input to an isoflux control algorithm that generates voltage requests to the power supplies. The reconstruction of plasma boundaries in real-time compare well to those reconstructed using the EFIT code offline in between plasma discharges [30].

The RAPTOR (RApid Plasma Transport simulatOR) is a model-based control-oriented code that predicts tokamak plasma profile evolution on real-time, it predicts the evolutions of several parameters, thanks to its accurate yet simplified physics model [31]. The physical model of the plant is derived from a spatially discretized partial differential equation (PDE), yielding a nonlinear set of ordinary differential equations (ODEs) for which the derivatives are evaluated analytically by the RAPTOR code. One of the main RAPTOR features is that while the plasma is evolving RAPTOR has full knowledge of the plasma profiles and the available real-time diagnostic data can be included in a natural way to improve the accuracy of the estimation, in control engineering this approach is known as dynamic state observer and is used to estimate unmeasured or poorly states of a dynamical system [32]. This dynamic state observer consists on an extended Kalman filter which estimates an augmented state consisting of physical states and random-walk disturbances [33]. The concepts of states-space systems and Kalman filtering will be addressed in the next subsections. Figure 2.9 scheme shows the carries out integration of the RAPTOR code on top of the MARTe framework at the Italian tokamak RFX-mod.

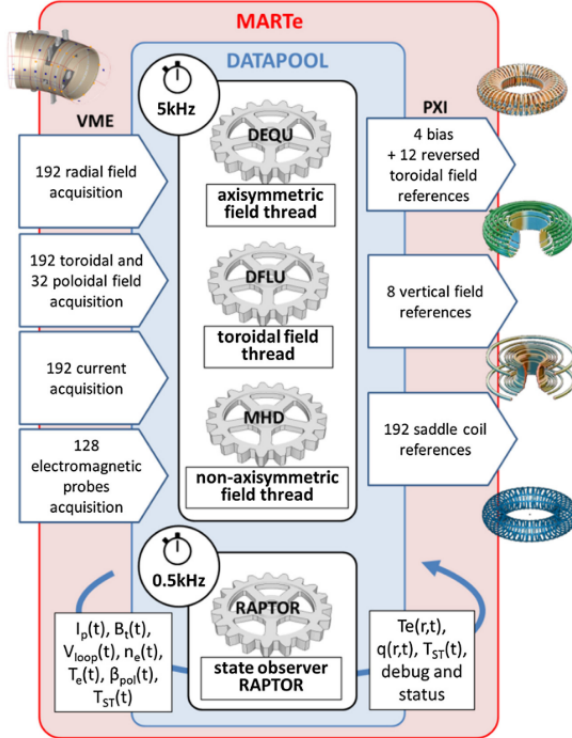


Figure 2.9.: Sketch of the integration of the state observer RAPTOR in the RFX-mod real-time control system based on the MARTe framework. experimental [31]

For the case of JET a boundary reconstruction package called XLOC has been used to localized the X-point position and plasma boundary [34]. A newer code relying on XLOC called Equinox was designed and implemented in C++ using a finite element method and a non linear fixed point algorithm associated to a least square optimization procedure to reconstruct the plasma equilibrium in less than 50ms for the real-system [35].

The CREATE codes (CREATE-L [36] and CREATE-NL [37]) are equilibrium solvers that will be widely described in next chapter as well as their application to plasma shape and position control design for the JT60-SA tokamak.

2.4 CONTROL TECHNIQUES AND STATE-SPACE MODELS

This section will summarize some systems dynamics and control concepts which will be applied on the next chapters. Applying a feedback control loop to a system brings a link between the output and input signals , this action corrects the error in between the system output and a desired set-point, eventually the objective of any closed loop controller is to take and maintained the output signal at a prescribed value. The reduction of the system error is merely one of the many important effects that feedback may have upon a system, that is the reason why this sections will deepen in several control techniques [38, Chapter 1]. This section will also delve into the state-space models concepts since it will be a recurrent representation for several systems presented in next chapters.

2.4.1 State-Space models

State-space models will be crucial for the overall development of the work presented on this thesis whether they will be use to describe a tokamak linear model for plasma position and shape control or use to model some other relevant variables. The first concepts to be summarized on this section are the state variable and state equation definitions ([38, Chapter 10], [39, Chapter 2]).

Let the n state equations of n th-order dynamic system be represented as:

$$\frac{dx_1(t)}{dt} = f_i[x_1(t), x_2(t), \dots, x_n(t), u_1(t), u_2(t), \dots, u_p(t), w_1(t)w_2(t), \dots, w_v(t)] \quad (2.1)$$

where $i = 1, 2, \dots, n$. The i th state variable is represented by $x_i(t)$; $u_j(t)$ denotes the j th input for $j = 1, 2, \dots, p$; and $w_k(t)$ denotes the k th disturbance⁸ input, with $k = 1, 2, \dots, v$.

Let $y_1(t), y_2(t), \dots, y_q(t)$ be the q system output variables. The output variables are functions of the state variables and the input variables. The output equations can be expressed as:

$$y_j(t) = g_j[x_1(t), x_2(t), \dots, x_n(t), u_1(t), u_2(t), \dots, u_p(t), w_1(t)w_2(t), \dots, w_v(t)] \quad (2.2)$$

⁸ The unknown disturbances acting on the state-space model are assumed to be generated by independent stochastic noise vectors.

where $j = 1, 2, \dots, q$.

The set of n state equations from 2.1 and the q output equations in 2.2 together they form the *dynamic equations*. In order to have an easier form of expression and manipulations of these equations is common to represent them in vectors and matrices as follows: **State vector:**

$$x(t) = \begin{bmatrix} x_1(t) \\ x_2(t) \\ \vdots \\ x_n(t) \end{bmatrix} \quad (n \times 1) \quad (2.3)$$

Input vector:

$$u(t) = \begin{bmatrix} u_1(t) \\ u_2(t) \\ \vdots \\ u_p(t) \end{bmatrix} \quad (p \times 1) \quad (2.4)$$

Output vector:

$$y(t) = \begin{bmatrix} y_1(t) \\ y_2(t) \\ \vdots \\ y_q(t) \end{bmatrix} \quad (q \times 1) \quad (2.5)$$

Disturbance vector:

$$w(t) = \begin{bmatrix} w_1(t) \\ w_2(t) \\ \vdots \\ w_v(t) \end{bmatrix} \quad (v \times 1) \quad (2.6)$$

Using these defined vectors, equation 2.1 can be write for the n states like:

$$\frac{dx(t)}{dt} = f[x(t), u(t), w(t)] \quad (2.7)$$

where f is a vector containing the functions f_1, f_2, \dots, f_n as elements. In the same way the equations from 2.2 become:

$$y(t) = g[x(t), u(t), w(t)] \quad (2.8)$$

where g is a vector containing the functions g_1, g_2, \dots, g_n as elements.

For a system that is time-invariant and linear like the ones that will show on next chapter, the equations can be re-write as:

$$\frac{dx(t)}{dt} = Ax(t) + Bu(t) + Ew(t) \quad (2.9)$$

$$y(t) = Cx(t) + Du(t) + Hw(t) \quad (2.10)$$

where A is the state matrix, B is the input matrix, C is the output matrix, D is the feed-forward matrix and E and H are disturbances matrices. For simplification is usual the study state-space and controllers concepts under the assumption that $w(t) = 0$ which leads to the form:

$$\frac{dx(t)}{dt} = Ax(t) + Bu(t) \quad (2.11)$$

$$y(t) = Cx(t) + Du(t) \quad (2.12)$$

When applying the Laplace transform to system from 2.12 it leads to:

$$x(s) = (sI - A)^{-1}[x(0) + Bu(s)] \quad (2.13)$$

$$y(s) = C(sI - A)^{-1}[x(0) + Bu(s)] + Du(s) \quad (2.14)$$

where $x(0)$ is the initial state or initial conditions from the system [40, Chapter 4]. The representation of the system from equation 2.14 shall be use in next subsections.

State-space dynamics can describe Multiple-Input Multiple-Output (MIMO) models where a number of inputs $n_{inputs} > 1$ can relate through the dynamics matrices of the system to a number of outputs $n_{outputs} > 1$. Given the physical conditions of the systems that will be analyzed and controlled on this work MIMO models will show several times.

2.4.2 PID control

This subsection will shortly address the Proportional-Integral-Derivative (PID) control concepts. PID controllers are now at days the most common ones in industrial applications and they are use several times through all this work. The PID controller has three parameters; proportional gain, integral gain, and derivative gain, they have proved through the years to provide a suitable control for a variety of systems despite not being optimal always. The usefulness of PID controls lies in their general applicability to most control systems. In particular, when the mathematical model of the plant is not known and therefore analytical design methods cannot be used, PID controls prove to be most useful.

The closed-loop systems compensate the disturbances by measuring the output response, feeding that measurement back through a feedback path, and comparing that response to a reference or set point. If there is any difference between the two signals, the system drives the plant, via the actuating signal, to make a correction. If there is no difference, the system does not drive the plant, since the

plant's response is already the desired set point [41, Chapter 1]. Closed-loop systems also focus on achieving the stability as a system must be stable in order to produce the proper transient and steady-state response [41, Chapter 3], thus if the closed-loop system poles are in the left half of the plane the feed-back system will be stable.

Systems that feed the error forward to the plant are called proportional control systems. Systems that feed the integral of the error to the plant are called integral control systems. Finally, systems that feed the derivative of the error to the plant are called derivative control systems [41, Chapter 9]. A PID controller consists on a feedback control loop where the current, previous and future error signal which originates from the difference between the output of the system and a given set point, is multiplied by the proportional, integral and derivative gains and then sum converting this signal into the system input, the effects on the feedback loop from each one of the gains will be described. When the model of the system plant is known is possible to apply designing techniques for the PID gains like the Ziegler-Nichols method, when is not the case analytical or even intuition arising from the physics and numerics of the problem should be applied. Figure 2.10 shows the block scheme of a PID controller with a system plant $G(s)$ on the Laplace domain.

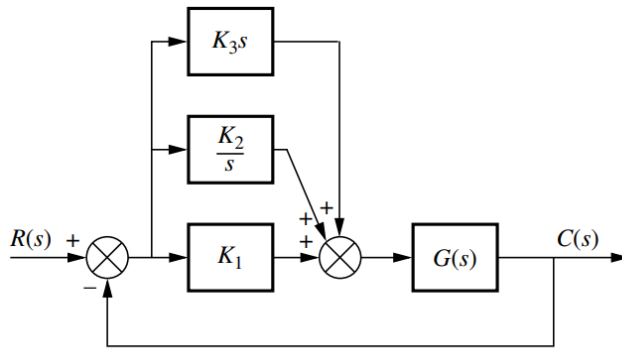


Figure 2.10.: Plant and PID controller block scheme on Laplace domain [41, Chapter 9].

An only proportional controller relates the output of the system to the input by a proportional constant, and even though it performs a first approach to follow the set point and stabilizes, it results in a steady-state error or offset, such error may be eliminated with integral control action, see figure 2.11.

The integral gain produces a signal that is proportional to the time integral of the error system, the offset or steady-state error can be eliminated by the sum of an integral action, the integral term also tends to produce an oscillatory response. This is an important improvement over the proportional control alone, which gives an offset. Since the PI controller is also a low-pass filter, it helps filtering out the high-frequency noise [38, Chapter 9], [42, Chapter 5]. Figure 2.12 shows the block scheme of a PI controller and its response to a unitary step.

The derivative gain added to a proportional controller gives a more sensitive controller which responds to the rate of change of the error and can produce a significant correction before the magnitude of the error becomes large. In general, derivative control anticipates the actuating error, adds damping and

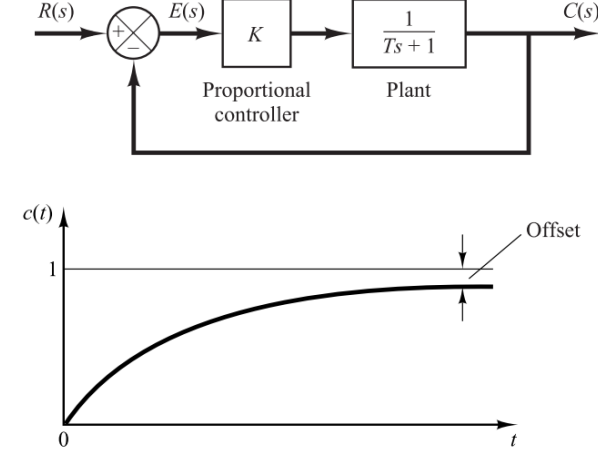


Figure 2.11.: Plant with a proportional (P) control scheme on the Laplace domain and its response to a unit-step. The offset or error between the steady-state response is also pointed out [42, Chapter 5].

tends to increase the system stability, figure 2.13 depicts the scheme and system response with a PD controller. The PD control uses the error derivative $de(t)/dt$ which allows the control to anticipate the error direction, it initiates an early corrective action which means an improvement on the transient response [38, Chapter 9], [41, Chapter 9]. Normally in linear systems when the slope of $e(t)$ is large overshoots may occur, when using a PD controller it also corrects the overshoot.

A PID controller improves the steady-state error and the transient response. Figure 2.14 shows the response time traces of the same system with a PID, PD and D controllers to a unit step.

2.4.3 Multiple-Input Multiple-Output control

This subsection will discuss the pole-place method and the linear quadratic optimal regulator (LQR) for control systems in state-space already discussed in subsection 2.4.1. State feedback controllers basically relocate the eigenvalues of the given system through a state-feedback multiplication by a constant gain matrix K so the system can follow a reference and be stabilized if necessary.

The concept of pole should be introduced as it will be related to the definitions of the MIMO control methods. The poles p_i of state-space system are the eigenvalues $\lambda_i(A)$, $i = 1, \dots, n$ of the system matrix A . Poles are important for establishing the stability of a system, for continuous systems a linear dynamic system $\dot{x}(t) = Ax(t) + Bu(t)$ is stable if and only if all poles are in the open left half plane (LHP), that is $\text{Re } \lambda_i(A) < 0, \forall i$. Eigenvalues in the right half plane (RHP) with $\text{Re } \lambda_i(A) \geq 0$ give rise to unstable modes since for this case $e^{\lambda_i(A)t}$ is unbounded as $t \rightarrow \infty$, eigenvalues in the open LHP give rise to stable modes where $\text{Re } \lambda_i(A) \rightarrow 0$ as $t \rightarrow \infty$ [43, Chapter 4].

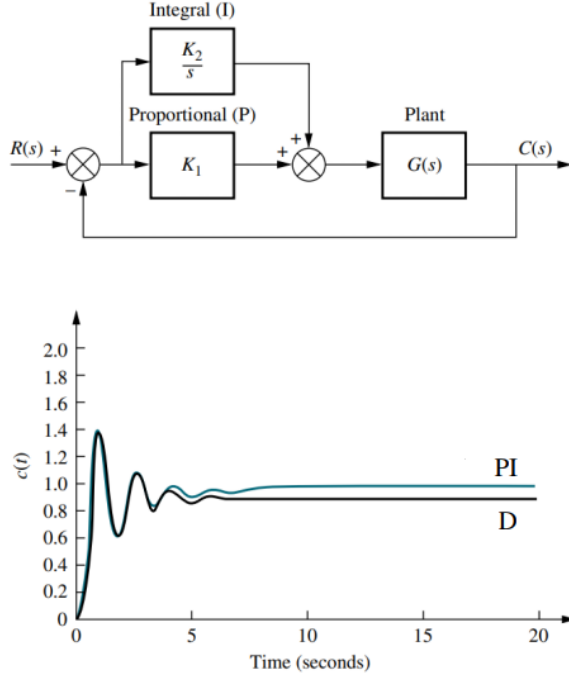


Figure 2.12.: Plant scheme of a plant with a proportional-integral (PI) control on the Laplace domain. Bottom graph corresponds to a step response to closed-loop systems with D and a PI controller [41, Chapter 9], a visible improvement on the state-state error with the PI control is observable.

Consider the system:

$$\dot{x}(t) = Ax(t) + Bu(t) \quad (2.15)$$

$$y(t) = Cx(t)$$

where it is assumed that $D = 0$. In state feedback, the input $u(t)$ is given by:

$$u(t) = r(t) - Kx(t) = r(t) - [k_1 \ k_2 \ \dots \ k_n]x(t) = r - \sum_{i=1}^n k_i x_i \quad (2.16)$$

as shown in figure 2.15. Each feedback gain k_i is a real constant. This is called the constant gain negative state feedback or in a simpler form *state feedback* [40]. Substituting equation 2.15 into 2.16 its obtained:

$$\dot{x}(t) = (A - BK)x(t) + Br(t) \quad (2.17)$$

$$y(t) = Cx(t)$$

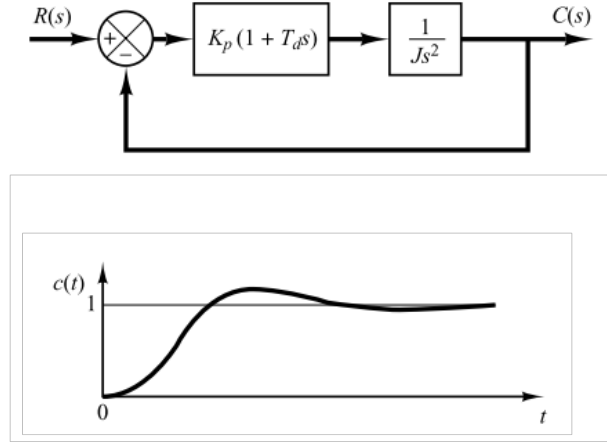


Figure 2.13.: The top scheme shows a PD controller for a plant that is only modeled as an inertial load, on the graph below is shown the system response where it is possible to observe an offset reduction and a controlled transient as compared with the P controller [42, Chapter 5].

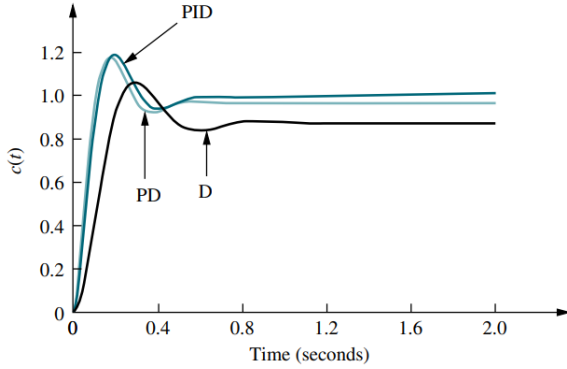
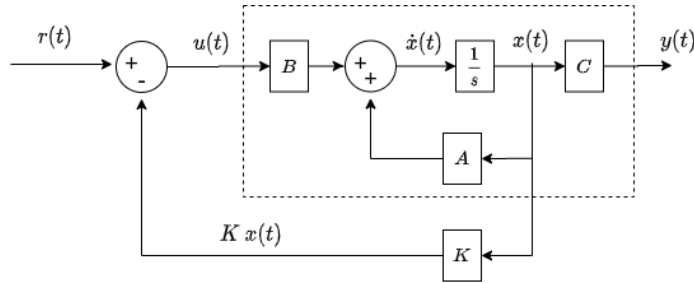


Figure 2.14.: Step response to closed-loop systems with D, PD and PID controllers [41, Chapter 9].

The first control MIMO algorithm to be addressed is the pole-placement method which consists in placing the closed-loop system poles in certain location by means of state feedback through an appropriate state feedback gain matrix K , the design objective of the pole-placement design is to find K such that the eigenvalues or poles of $(A - BK)$, or the closed-loop system, are of certain prescribed values. For this method the eigenvalues of the closed-loop system can assigned arbitrarily as long as they are stable [38, Chapter 10]. The determination of the desired closed-loop poles is based on the transient-response and/or frequency-response requirements, such as speed, damping ratio, or bandwidth, as well as steady-state requirements [42, Chapter 10].

Let's consider the system given in equation 2.17 and the feedback control input from 2.16, by substituting one on the other the closed-loop system is represented by the equation:

$$\dot{x}(t) = (A - BK)x(t) + Br(t) \quad , \quad (2.18)$$

Figure 2.15.: State-space model with a K gain matrix feedback scheme.

K is the $1 \times n$ feedback matrix that can give an arbitrary set of eigenvalues or poles of $(A - BK)$, which are the n roots of the Laplace equation [38, Chapter 10]:

$$|sI - A + BK| = 0 \quad . \quad (2.19)$$

From the canonical representation of equation 2.15 its obtained ([38, Chapter 10] , [40, Chapter 4]) :

$$A = \begin{bmatrix} 0 & 1 & 0 & \cdots & 0 \\ 0 & 0 & 1 & \cdots & 0 \\ \vdots & \vdots & \vdots & \ddots & \vdots \\ 0 & 0 & 0 & \cdots & 1 \\ -a_0 & -a_1 & -a_2 & \cdots & -a_{n-1} \end{bmatrix} \quad B = \begin{bmatrix} 0 \\ 0 \\ \vdots \\ 0 \\ 1 \end{bmatrix} \quad . \quad (2.20)$$

Then the gain feedback matrix K is expressed as:

$$K = [k_1 \ k_2 \ \cdots \ k_n] \quad (2.21)$$

where k_1, k_2, \dots, k_n are real constants, this leads to the expression:

$$A - BK = \begin{bmatrix} 0 & 1 & 0 & \cdots & 0 \\ 0 & 0 & 1 & \cdots & 0 \\ \vdots & \vdots & \vdots & \ddots & \vdots \\ 0 & 0 & 0 & \cdots & 1 \\ -a_0 - k_1 & -a_1 - k_2 & -a_2 - k_3 & \cdots & -a_{n-1} - k_n \end{bmatrix} \quad (2.22)$$

The eigenvalues or poles of $A - BK$ can be found from the characteristic equation:

$$|sI - A + BK| = s^n + (a_{n-1} + k_n)s^{n-1} + (a_{n-2} + k_{n-1})s^{n-2} + \cdots + (a_0 + k_1) = 0 \quad (2.23)$$

since the elements k_1, k_2, \dots, k_n are isolated in each coefficient of the characteristic equation the eigenvalues can be arbitrarily assigned to any set of stable poles [38, Chapter 10], [42, Chapter 10].

Another control technique for state-space feedback is the optimal control referred as Linear Quadratic Gaussian (LQG) or Linear Quadratic Regulator (LQR). It is assumed that the plant dynamics are linear and there are noise measurements and disturbance signals stochastic with known statistical properties [43, Chapter 9].

Consider the system:

$$\dot{x}(t) = Ax(t) + Bu(t) \quad (2.24)$$

that has an initial condition $x(t_0) = x_0 \neq 0$. Therefore $x(t) \neq 0, t \geq t_0$ and the regulator problem is to apply an input signal $u(t)$ that takes the system back to the zero state in an optimal manner. The manner the LQR regulator achieves this is by minimizing the deterministic cost [43, Chapter 9], [38, Chapter 3]:

$$J_r = \int_0^{\infty} (x(t)^T Q x(t) + u(t)^T R u(t)) dt \quad (2.25)$$

where Q is a positive-definite Hermitian or real symmetric matrix and R is a positive-definite Hermitian or real symmetric matrix. The optimal solution is for any initial state $u(t) = -K_r x(t)$ where:

$$K_r = R^{-1} B^T X \quad (2.26)$$

and $X = X^T \geq 0$ is the unique positive-semidefinite solutions of the algebraic Riccati equation

$$A^T X + X A - X B R^{-1} B^T X + Q = 0 \quad . \quad (2.27)$$

In order to design the optimal K_r feedback gain the Riccati equation 2.27 has to be solved for the matrix X and then substitute into equation 2.26.

2.4.4 Observers and Kalman filters

In practical real systems that have been modeled as state-space it may occur that the states vector, which is vital for performing the feedback control of the methods just presented, is not fully measurable, when this occurs is necessary to retrieve the states-vector $x(t)$ from the system outputs $y(t)$ and is obtained through an state estimator also called observer to estimate not measurable state variables [40, Chapter 8]. A state observer estimates the state vector based on the measurements of the output and inputs system signals. The inputs of the observer are the output $y(t)$ and the control input $u(t)$. Similarly with the construction of a state-space controller, the observer uses an observer gain matrix K_{obs} which is a weighting matrix to the correction term involving the difference between the measured output $y(t)$ and the estimated output $C x_{est}(t)$, where $x_{est}(t)$ are the estimated states [42, Chapter 10].

Through the observer gain matrix K_{obs} is possible to retrieve an estimated state-space model which will have as output the reconstructed states $x_{est}(t)$ and the reconstructed outputs $y_{est}(t)$, the estimation

error or observation error is the difference between $y(t)$ and $y_{est}(t)$. Figure 2.16 shows a scheme of state-space plant model and a observer block to reconstruct the states.

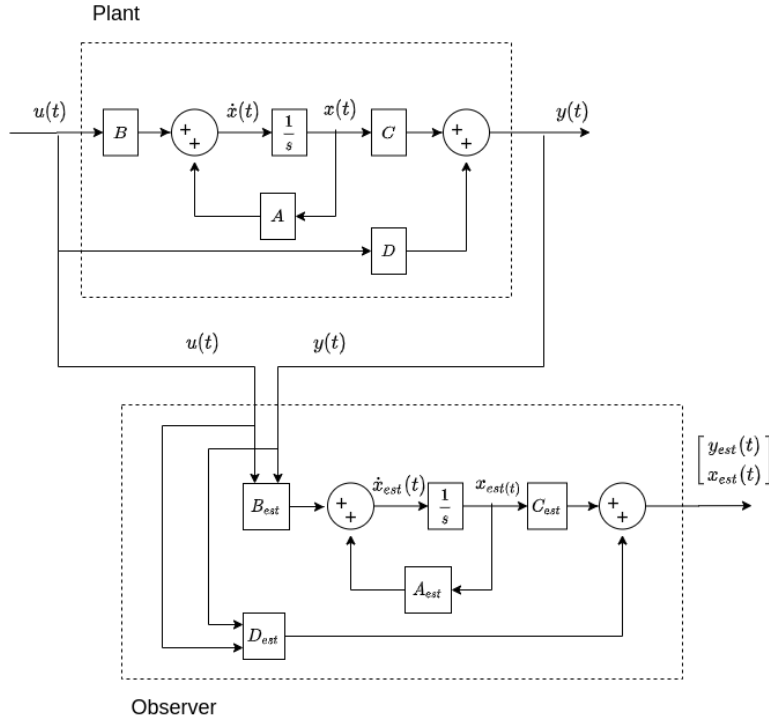


Figure 2.16.: Scheme of a state-space model plant and its observer or state estimator.

Kalman filters have the structure of an ordinary state estimator but they take into account the process and measurement noise(ω_d, ω_n) from the inputs signals. In Kalman filters the optimal choice of K_{obs} , which minimizes the covariance $E[x - x_{est}]^T [x - x_{est}]$, is given by ([43, Chapter 9], [44, Chapter 8]):

$$K_{obs} = Y C^T V^{-1} \quad (2.28)$$

where $Y = YT \geq 0$ is the unique positive-semidefinite solution of the algebraic Riccati equation:

$$YA^T + AY - YC^T V^{-1} CY + W = 0 \quad (2.29)$$

where W is a positive-definite Hermitian or real symmetric matrix and V is a positive-definite Hermitian or real symmetric matrix, solving equation 2.29 for Y and substituting on 2.28, gives the optimal K_{obs} for reconstructing the states of the original system . The combination of an optimal state estimator or Kalman filter and an optimal state feedback or LQR controller is commonly called LQG, this type of compensator-estimator configuration will be used ahead for implementation of plasma position controllers.

2.4.5 Experimental identification of state-space models

When experimental work is been carrying out most of the times the available signals are not continuous. In addition it may happen that a theoretical model that links the signals at a experiment as inputs and outputs of it, does not exist or has not been done yet. This section will address the representation in discrete time of state-space models as well as a method for retrieving a model only when the input and output signals are available along with some useful concepts.

For some physical systems is natural to work with the continuous-time representation of the systems since most of the basic relationships are expressed in terms of differential equations. The relation between the Laplace transform of the input and output of the system is called *transfer function* and is represented as: $Y(s) = G_C(s)U(s)$, where introducing p as the differential operator the time-domain transfer function yields as: $y(t) = G_C(p)u(t)$. Taking into account the disturbances that influence on the system the transfer function can be re-write as: $y(t) = G_C(p)u(t) + H(q)w(p)$ [45, Chapter 2]. Thus, the discrete transfer function will be $G_C(p) \rightarrow G_T(q)$ where q is the discrete time shift operator, for the state-space models variables G_T and H are matrices. The concept of transfer function will be frequently used in this section.

State-Space discrete models

When implementing numerical methods and models in digital computers it is necessary to transfer the continuous variables and models to their discrete equivalents. If an input $u(t)$ is generated by a digital computer followed by a digital to analog converter (DAC), then $u(t)$ will be piecewise constant, this situation often arises in computer control of control systems [40, Chapter 4]. Let:

$$u(t) = u(kT) =: u[k] \quad \text{for } kT \leq t < (k+1)T \quad (2.30)$$

for $k = 0, 1, 2, \dots$, where T is the sampling time. This input $u[k]$ changes values only at discrete time instants. If an input changes its value only at discrete time instants kT and the response is only compute at $t = kT$ then discrete state-space model (considering absence of disturbances) can be represented as:

$$x[k+1] = A_d[k] + B_d u[k] \quad (2.31)$$

$$y[k] = C_d x[k] + D_d u[k] \quad (2.32)$$

with

$$A_d = e^{AT} \quad B_d = \left(\int_0^T e^{A\tau} d\tau \right) B \quad C_d = C \quad D_d = D. \quad (2.33)$$

Discrete state-space model identification

For system identification purposes it is often desirable to use parametric models, i.e. , a set of models is described by a number of real-valued parameters collected in a parameter vector $\theta \in \mathbb{R}^d$ to be determined. A particular model is then represented by a value of the d-dimensional unknown parameters vector θ [46, Chapter 2]. Let's write the state-space model structure considering the discrete disturbances $w[k]$ in the form:

$$\begin{aligned}\mathcal{M} : \quad \hat{x}[k+1] &= A(\theta)\hat{x}[k] + B(\theta)u[k] + E(\theta)w[k] \\ y[k] &= C(\theta)\hat{x}[k] + w[k]\end{aligned}\tag{2.34}$$

where the vectors \hat{x} and \hat{y} are called predictors and they are the conditional expectations of $x(t)$ and $y(t)$ given information up to $k - 1$ and the matrices A, B, C and E are constructed from the parameter vector θ according to the model structure \mathcal{M} . Let:

$$d_{\mathcal{M}} = \dim \theta\tag{2.35}$$

denote the dimension of the parameter vector θ and let $\mathcal{M}(\theta)$ denote the model from equation 2.34. The way of representing the disturbances in 2.34 is called the innovations form. The model will thus have the transfer functions:

$$G(q, \theta) = C(\theta)[qI - A(\theta)]^{-1}B(\theta)\tag{2.36}$$

and

$$H(q, \theta) = I + C(\theta)[qI - A(\theta)]^{-1}K(\theta) .\tag{2.37}$$

From equation 2.34, the state predictor $\hat{x}[k+1]$ is given by:

$$\begin{aligned}\hat{x}[k+1] &= [A(\theta) - K(\theta)C(\theta)]\hat{x}[k] + B(\theta)u[k] + -K(\theta)y[k] \\ \hat{y}[k|\theta] &= C(\theta)\hat{x}[k]\end{aligned}\tag{2.38}$$

where $\hat{y}[k|\theta]$ denotes the conditional expectation of $y[k]$ given the parameter vector θ [45, Chapter 3], this is a one-step ahead prediction and is denote as $\hat{y}[k|\theta]$ to emphasize its dependence on the parameter vector θ .

The system identification technique applied is based on the prediction error minimization (PEM) [45, Chapter 7], [45, Chapter 3]. The standard setting can be described as: given the experimental data consisting of an input vector $u[k]$ and an output vector $y[k]$ by:

$$Z^N = \{y[k], u[k] | k = 1, \dots, N\},\tag{2.39}$$

and a model structure \mathcal{M} defining a mapping from the parameter space $D_{\mathcal{M}}$ to the outputs predictor $\hat{y}(t|\theta)$, the objective is to find the value $\hat{\theta}$ which minimizes a criterion $V_N(\theta)$. This criterion is defined as:

$$V_N(\theta) = \frac{1}{N} \sum_{t=1}^N |\varepsilon[k, \theta]|^2, \quad (2.40)$$

where $|\cdot|$ is the Euclidian $l_2 - \text{norm}$. The prediction error is the vector

$$\varepsilon(t, \theta) = y[k] - \hat{y}[k|\theta] \quad (2.41)$$

with the predictor $\hat{y}(t|\theta)$ given by the equation 2.38. The minimizing parameter vector is defined by:

$$\hat{\theta}_N = \arg \min_{\theta \in D_{\mathcal{M}}} V_N(\theta) \quad (2.42)$$

where "arg min" is the operator returning the argument which minimizes the function. The minimization of $V_N(\theta)$ given in equation 2.40 as well as the properties of the resulting estimation of the parameters vector $\hat{\theta}_N$ under varying assumptions on the model structure \mathcal{M} and the experimental data set Z^N , has been formulated in the related literature and computationally implemented, such is the case of the *System Identification Toolbox* from MATLAB. This toolbox relies on the function called "pem" for computing the error minimization which returns an estimated state-space model given a data vector of input and output signals [47, Chapter 4], the model is adjusted by optimizing the prediction error fit, it is possible to select the order of the model or use the "best" order given by the toolbox. Due to its adaptability and flexibility, this toolbox was used for retrieving data-driven models in several stages of the implementation in real-time of some of the algorithms in ISTTOK.

3

JT60-SA CONTROL DESIGN

3.1 MACHINE DESCRIPTION

JT60-SA is a superconductive tokamak located at one of the facilities from the National Institutes for Quantum and Radiological Science and Technology (QST) at Naka, Japan whose principal purpose is the contribution to early realization of fusion energy by supporting the exploitation and resolving key physics for the ITER reactor. JT60-SA construction has been successfully completed by the end of March 2020 and its first plasma is expected for late 2020. Figure 3.1 shows the overall general configuration and the most remarkable elements of the machine. The JT-60SA vacuum chamber will have a major radius of 2.96 m and a Minor radius of 1.18 m with an overall plasma volume of 132 m^3 [48]. JT60-SA will become the largest tokamak ever built so far. Appendix B contains a set of photos depicting the assembling of some of the JT60-SA components and its overall look during 2018 and 2019.

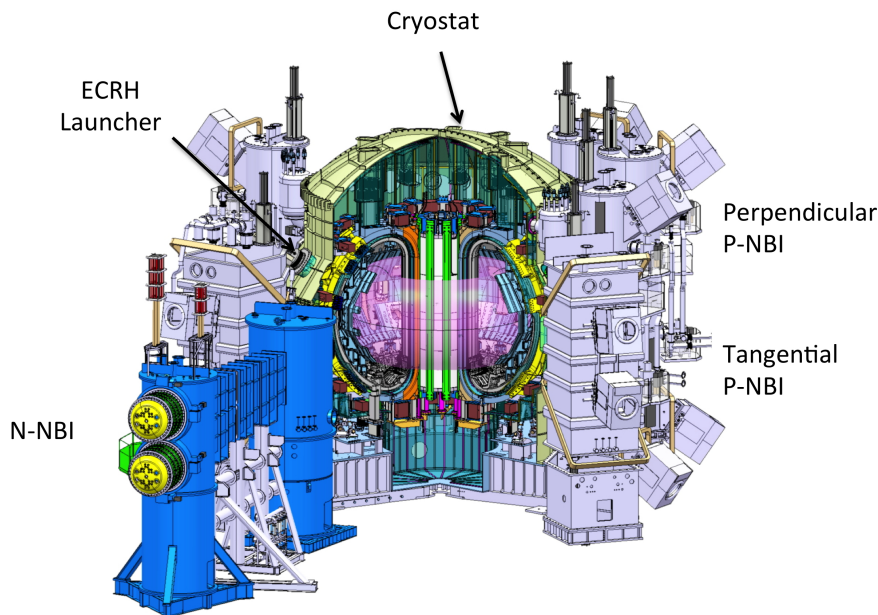


Figure 3.1.: JT60-SA tokamak configuration and its main elements [49].



Figure 3.2.: JT-60SA poloidal cross-section and layout of the Poloidal Field coils system [50].

The Poloidal Field (PF) coils shown in JT60-SA cross-section from figure 3.2 consist of two sets of superconductive coils: the Equilibrium Field Coils (EF1–6) and the Central Solenoid (consisting of four independent coils, named CS1–4) which are ex-vessel coils. Furthermore, two in-vessel cooper Fast Plasma Position Coils (FPPC1–2) will also be installed [50]. The total of 12 PF coils have independent power sources for the control of the plasma current, position and shape.

JT-60SA shall be capable of investigating different design scenarios. As referred in [51] it exists a set of 6 reference scenarios, additional ones, including some with a shorter repetition rate will be defined in future. For the control study in this section all simulations will be built based on the Scenario 2 characteristics. In particular, Scenario 2 refers to a 5.5 MA inductive lower single null discharge. The Scenario 2 its divided in 5 time snapshots with different equilibrium each one starting at $t=-40$ s until $t= 177.96$ s. The different Last Closed Flux Surfaces (LCFS) for each time window are shown in figure 3.3, the time sequence starts at the X-point formation (XPF) followed by the Start of Heating(SOH), the Start of Flattop (SOF), End of Flattop (EOF), End Of Cooling(EOC) and finishing with the End of Currents in the PF coils (EOC). In this section, reconstruction methods and control algorithms will be based on the *Start of Flattop* (SOF) equilibrium shown in figure 3.4. The nominal values for the plasma current,

the poloidal beta and the internal inductance for Scenario 2 at SOF are $I_{p_{eq}} = 5.5$ MA, $\beta_{p_{eq}} = 0.53$, and $l_{i_{eq}} = 0.85$.

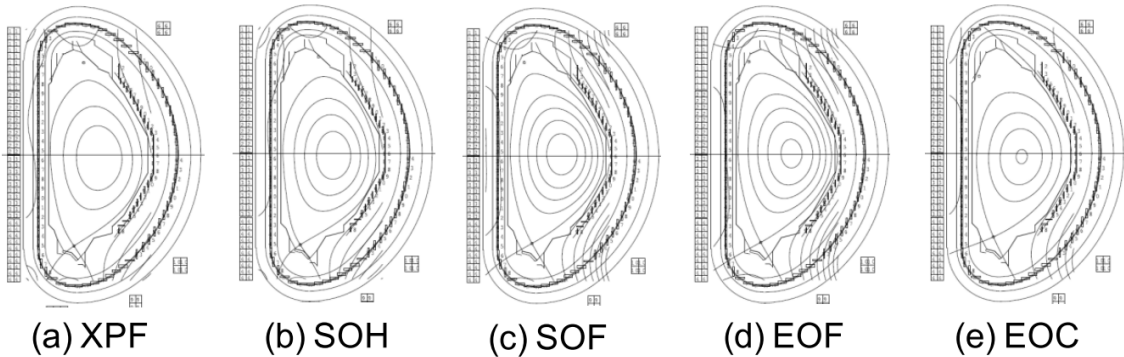


Figure 3.3.: LCFS Equilibria corresponding to the different Scenario 2 snapshots: X-point formation (XPF), Start of Heating(SOH), the Start of Flattop (SOF), End of Flattop (EOF), End Of Cooling(EOC) and End of Currents in the PF coils (EOC) [51].

This chapter will address two different approaches for the LCFS reconstruction along with different plasma current, shape and position controllers for JT60-SA in order to achieve and maintain the desired operational scenario given the plasma equilibrium in the SOF while the performance of the controllers is compared .

3.2 CREATE MAGNETIC RECONSTRUCTION TOOLS

CREATE-NL is a finite elements method (FEM¹) solver implemented on MATLAB. It deals with the free boundary dynamic plasma equilibrium problem i.e. the MHD (Magneto-Hydro-Dynamics) time evolution of 2D axisymmetric plasmas in tokamaks, including eddy currents in the passive structures, and feedback control laws for current, position and shape control [52]. CREATE-NL is an upgraded version of the CREATE-L code written in FORTRAN and validated in different tokamaks. Both CREATE-L and CREATE-NL produce linerized models of the plasma in the neighborhood of a certain equilibrium condition. CREATE-NL has more capabilities than CREATE-L due to the possibility of using different plasma profiles shapes, introducing different outputs in a user friendly way and running inverse equilibrium calculation [53].

Using the CREATE codes [36,52] it is possible to retrieve a linearized state-space model for a reference configuration that describes the plasma magnetic behavior around that equilibrium². It should be noted that CREATE-NL equilibrium solver has been validated on several tokamaks such as JET and EAST. A

¹ It is well known that many physical and engineering systems are expressed in terms of partial differential equations which cannot be solved via analytical methods. One of the most recurrent techniques is numerical discretization to approximate the solution of the partial differential equations, the FEM is commonly used to solve these approximations in two or three space variables, in this particular case for a numerical solution of the well-known Grad-Shafranov equation.

² Reference [50, Sec. 3] can be consulted for more details about the use of the CREATE equilibrium codes to retrieve plasma linearized models.

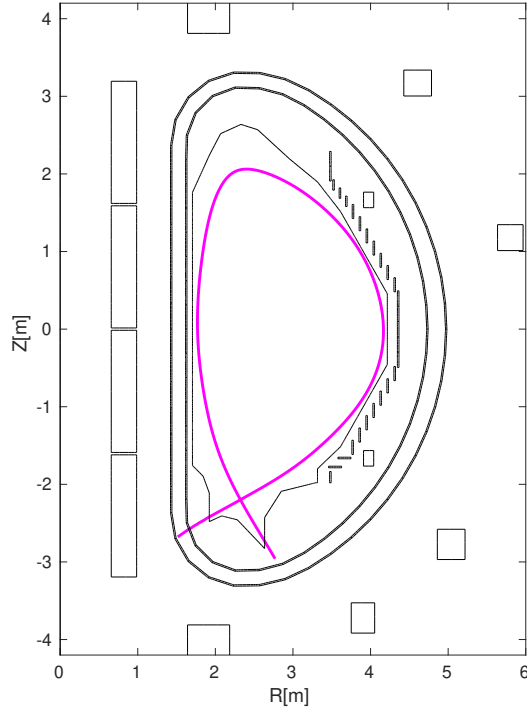


Figure 3.4.: Poloidal cross-section of the JT-60SA plasma at the Start of the Flat Top (SOF) for reference Scenario 2. At SOF, the nominal plasma current is 5.5 MA, while the nominal values for poloidal beta β_p and internal inductance l_i are 0.53 and 0.85, respectively.

JT60-SA CREATE-NL electromagnetic linear model around the equilibrium from the Scenario 2- SOF for the plasma-circuit response has been used for designing the controller presented in next section.

3.3 CONTROLLER DESIGN

The JET (Joint European Torus) tokamak was the first machine where around 2005 a new model based plasma current and shape controller was set up and tested with the existing active circuits and control hardware. The novelty controller was the eXtreme Shape Controller (XSC) and its aim was to improve the performance of the, back then, present controller to allow the control of extremely shaped plasmas with higher values of elongation and triangularity [54]. More recently this control approach was utilized at TCV [55]. At JET, the XSC recently enabled the control of high triangularity shapes with both strike points in the divertor corner, which has a large impact in the H-mode confinement in the case of the ITER-like wall at JET [56].

Usually the controlled shape geometrical descriptors are the distances between the plasma boundary and the vessel at some specific points. These plasma-wall distances are called gaps [57]. The gaps are segments that can be used to describe the shape of the plasma boundary. Being g_i the abscissa along the i -th control segment, we assume that $g_i = 0$ at the first wall. *Gap-based* plasma shape control is

achieved by controlling to zero the difference $g_{i\text{ref}} - g_i$ on a sufficiently large number of gaps, being $g_{i\text{ref}}$ the value of the abscissa on the i -th control segment for the reference shape. Figure 3.5 shows a poloidal cross-section of JT-60SA together with a set of 85 gaps used for the assessment of the plasma shape control.

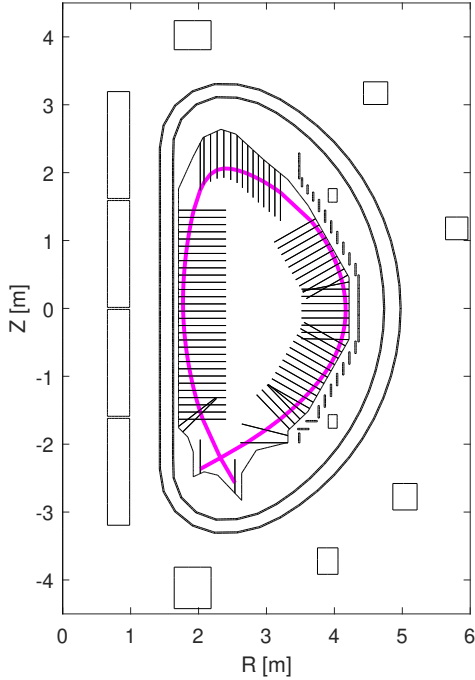


Figure 3.5.: Poloidal cross-section of the JT-60SA plasma at the Start of the Flat Top (SOF) for reference Scenario 2. At SOF, the nominal plasma current is 5.5 MA, while the nominal values for poloidal beta β_p and internal inductance l_i are 0.53 and 0.85, respectively. In this figure the 85 gaps used to assess the plasma shape controller performance are shown.

The XSC algorithm can be used either to implement a gap-based control strategy, or an isoflux one, as it has been proposed in [50]. The isoflux strategy consists in controlling the X-point position along with a set of flux differences between the flux at some selected control points along the desired plasma boundary and the X-point flux. Thus the XSC block inputs are the error between the X-point flux and the fluxes in the control points, and the X-point position error.

The peculiarity of the XSC approach is that it permits to control a number of plasma shape descriptors that is greater than the number of available actuators, i.e. of PF Circuits, this is basically tackled by using a singular value decomposition (SVD) to identify the principal directions of the algebraic mapping between coil currents and geometrical descriptors [54]. The XSC control relies on the PFC decoupling controller (more details can be found in [50, Section 4.4]), since it is assumed that each PF coil can

be treated as an independent single-input-single-output (SISO) channel whose dynamic response is modeled in the Laplace domain by

$$I_{PF_i}(s) = \frac{I_{PF_{ref,i}}(s)}{1 + s\tau_{PF}},$$

where I_{PF_i} and $I_{PF_{ref,i}}$ are the Laplace transform of the measured and reference current in the i -th PFC, respectively, and where it is assumed that all the PFC exhibit the same bandwidth (i.e., they have the same time constant τ_{PF}).

Denoting by $\delta Y(s)$ the Laplace transform of the variations of the n_G shape descriptors to be controlled, it is possible to exploit the CREATE electromagnetic linear model [50] that links the variation of the PFC reference currents $\delta I_{PF_{ref}}$ to $\delta Y(s)$, i.e.

$$\delta Y(s) = C \frac{\delta I_{PF_{ref}}(s)}{1 + s\tau_{PF}},$$

which, at steady-state, implies $\delta Y(s) = C\delta I_{PF_{ref}}(s)$.

If the number of controlled plasma shape descriptors n_G is such that $n_G > n_{PF}$, the XSC computes the additional current references as

$$\delta I_{PF_{ref}} = C^\dagger \delta Y. \quad (3.1)$$

where the matrix C^\dagger denotes the pseudo-inverse of C^3 that can be computed via the singular value decomposition (SVD). As a result, the XSC algorithm minimizes the following steady-state performance index

$$J_{XSC} = \lim_{t \rightarrow +\infty} (\delta Y_{ref} - \delta Y(t))^T (\delta Y_{ref} - \delta Y(t)), \quad (3.2)$$

where δY_{ref} are constant references for the geometrical descriptors. When the SVD of the C matrix is used to minimize (3.2), it may happen that some singular values (depending on the plasma configuration) are one order of magnitude smaller than the others. This fact implies that minimizing the performance index (3.2) retaining all the singular values results in a large control effort at the steady-state, that is a large request on some PFC currents which have only a minor effect on the plasma shape. In order to minimize also the control effort, the additional references (3.1) are generated by using only the $\bar{n} < n_{PF}$ linear combinations of PF currents which are related to the largest singular values of the C matrix. This is achieved by using only the \bar{n} singular values when computing the pseudo-inverse C^\dagger .

Moreover, the PFC current variations given by (3.1) are summed to the scenario currents and sent to the PFC decoupling controller as references to be tracked. It is worth to remark here that the dynamnic behavior of the XSC is improved by adding a set of proportional-integral-derivative (PID) controllers on each PF coil channel (see [58] for a complete description of the XSC control scheme).

For the development of this work both approaches of the XSC strategy were studied and simulated for a different number of control points: isoflux and gap-based controllers. In addition, a second controller

³ C is the output matrix from the state-space linearized CREATE model for JT60-SA.

developed by the QST team was implemented in the simulations, the features of this controller will be detailed in the next section.

3.4 QST RECONSTRUCTION AND CONTROL IMPLEMENTATION

Along with the CREATE tools presented on last section for the reconstruction of the LCFS and the XSC for plasma shape control, a reconstruction code and controller provided by the QST team were implemented, tested and compared. This section will briefly describe these two methods and its limitations.

3.4.1 Cauchy Condition Surface (CCS) reconstruction method

The QST Cauchy Condition Surface (CCS) method for the reconstruction of the magnetic last closed flux surface (LCFS) calculates controlled variables for plasma position and shape control such as the poloidal magnetic flux at control points on an isoflux scheme [59]. The CCS method allows a selection up to 19 geometrical points for dexterizing the LCFS and its input parameters are the current in the PF coils, the measurements in the magnetic field and flux sensors and the plasma current. The output signals from the CCS reconstruction method are the magnetic fluxes at the X-point and at the selected geometrical points.

3.4.2 QST magnetic controller

The QST magnetic controller uses the PF coils signals to control the plasma current I_p , position and shape, and the FPPC coils signals for plasma position control. The PF coil currents I_{PF_ref} are calculated using an isoflux control approach using proportional-integral(PI) feedback controllers [60]. The controller calculates I_{PF_ref} reducing $\delta\Psi_s$ and $\delta\Psi_x$ according to:

$$I_{PF_ref}(t + \Delta t) = I_{PF}(t_0) + M_{PF}^\dagger \left[G_{SP} \delta\Psi_s(t) + G_{SI} \int_{t_0}^t \delta\Psi_s(t) dt + G_{XP} \delta\Psi_X(t) + G_{XI} \int_{t_0}^t \delta\Psi_X(t) dt \right], \quad (3.3)$$

where $\delta\Psi_s$ is the residual between the LCFS flux and the control point fluxes, $\delta\Psi_x$ is the difference between the I_p value and its reference, t_0 is the initial time, Δt is the coil control cycle, M_{PF}^\dagger is the $(m \times (n + 1))$ control matrix which is the pseudo-inverse of the Green function M calculated using the SVD method; where m is the number of PF coils, n is the number of control points including the evaluated X-point. G_{SP} and G_{SI} are the respective control gains for the PI plasma position and shape feedback controllers, G_{XP} and G_{XI} are the PI control gains for the I_p feedback control. G_{SP} and G_{XP} are dimensionless and, G_{SI} and G_{XI} are in s^{-1} .



Figure 3.6.: SOF equilibrium reconstructed from CREATE-NL and the CCS code along with the magnetic field and flux sensors locations.

The coils voltage command values ($V_{coil-com}$) are calculated considering the mutual interactions between the PF coils and the plasma, the actual values of the PF coil currents, I_p and the mutual inductances. On a real plasma experiment, the mutual inductances between the plasma and the PF coils are unknown due to the difficulty of measuring them directly. Therefore, they are provided by the CCS method. The controller calculates command values of PF coils voltages according to the following equation:

$$V_{com} = G_{vt} \left[M_{coil} \frac{(I_{coil_ref} - I_{coil_meas})}{dt} + \frac{M_{plasma_now} \cdot I_{p_now} - M_{plasma_bfr} \cdot I_{p_bfr}}{dt} \right], \quad (3.4)$$

where M_{coil} represents the mutual inductances between the coils, I_{coil_meas} are the measured coil currents, M_{plasma_now} and M_{plasma_bfr} are the mutual inductances between the plasma and the coils at the current and previous time step, I_{p_now} and I_{p_bfr} are the measured plasma current at the current and previous time step and G_{vt} is the voltage transformer gain.

On the other hand, the in-vessel FPPC coils currents (I_{FPPC_ref}) are calculated with an isoflux control approach which uses proportional-differential (PD) feedback control. In order to reduce the residual between the LCFS flux and two specified control points (Ψ_{SF}) the controller calculates (I_{FPPC_ref}) using:

$$I_{FPPC_ref}(t + \Delta t) = I_{FPPC}(t_0) + M_{FPPC}^\dagger \left[G_{FP} \delta \Psi_{SF}(t) + G_{FD} \frac{d}{dt} \delta \Psi_{SF}(t) \right], \quad (3.5)$$

where M_{FPPC}^\dagger is the 2×2 control matrix which is the pseudo-inverse of the Green function M_{FPPC} , G_{FP} and G_{FD} are the respective PD feedback gains for the plasma position control. G_{FP} is dimensionless and G_{FD} is in s.

3.5 SIMULATION RESULTS

The simulations for the JT60-SA CREATE-NL model, the XSC, the CCS reconstruction method and the QST controller were programmed on top of MATLAB and SIMULINK blocks. This section will address in detail the outcome of the control simulations using a linearized equilibrium given by CREATE-NL for JT60-SA, Scenario 2 at the SOF time frame. The first results to be presented correspond to a gap-based controller using the XSC with different tests cases.

The second part of the results corresponds to isoflux controllers using the XSC with a LCFS reconstruction given by CREATE and also given by the CCS method, as well as the QST controller with the LCFS reconstructed by the CCS method and by CREATE. The figures 3.7 and 3.8 show an overall control block scheme for the simulations. Figure 3.7 corresponds to a configuration using the XSC where the LCFS can be obtained through the CCS method or from the CREATE model. It is worth to point out the existence of the block localized on the bottom part of the scheme called "Vertical Stability Control" along with the XSC. The task of this block is to vertically stabilize the plasma by exploiting the in-vessel coils, which are able to guarantee a faster response due to the fact that the magnetic field generated



Figure 3.7.: JT-60SA overall control scheme with the CREATE linearized model and the CCS LCFS reconstruction method using the XSC for an isoflux control approach.

does not have to penetrate the vessel structures [50]. This controller calculates the voltages at the FPPC coils with the equation:

$$V_{FPPC}(t) = k_1 I_{FPPC}(t) + k_2 \dot{z}_p(t) \quad (3.6)$$

By tuning the gains k_1 and k_2 from equation 3.6 is possible to obtain zero velocity in the vertical plasma direction while maintaining low imbalance current I_{FPPC} in the in-vessel coils [50, Sec. 4.1]. In addition should also be notice the block "Ip Control" which is a Plasma current Controller, which tracks the desired value of the plasma current [61].

Figure 3.8 depicts a configuration using the QST controller receiving as inputs the magnetic fluxes measured at the control points reconstructed either by the CCS method or by the CREATE linearized model.

3.5.1 Disturbances

As far as plasma magnetic control is concerned, the JT60-SA linearized model disturbances have been modeled as variations of β_p and l_i . These disturbances should be in principle rejected by the control systems and maintain in the most accurate possible way the plasma equilibrium. The following set of disturbances have been considered:



Figure 3.8.: Isoflux control JT-60SA overall scheme with a block for the CREATE JT60-SA linearized model, a block for reconstructing the magnetic fluxes with the CCS method and the QST controller.

- **Disturbance #1** refers to the behavior of β_p and l_i soon after the current flattop is reached, as it was modeled in [62] (in this paper we assume that the flattop is reached at $t \sim 20$ s). As an example, the correspondent time traces are shown in figure 3.9⁴.
- **Disturbance #2** refers to the behaviour of β_p and l_i when a compound ELM⁵ appears during the flattop. As described in [51, p. 34], an instantaneous drop in β_p of $0.05 \beta_{p_{eq}}$ is followed by an exponential recovery with a time constant of 0.05 s with a frequency 10 Hz, l_i is described by an instantaneous drop of 0.06 ($l_{i_{eq}} - 0.5$) followed by an exponential recovery with a time constant of 0.05 s with a frequency 10 Hz. The time traces for β_p and l_i are described in figure 3.10.
- **Disturbance #3** describes an instantaneous drop in l_i of 0.2 ($l_{i_{eq}} - 0.5$) without recovery, simultaneous with a drop on β_p of 0.2 $\beta_{p_{eq}}$ followed by a recovery exponential time of 1 s [51, p. 34], which are typical of a so called *Minor disruption*. The correspondent time traces for both β_p and l_i are reported in figure 3.11.

3.5.2 Gap-based XSC

JT-60SA represents a relevant benchmark to further validate the gap-based control approach, given the high beta regimes that are envisaged during its operation, which represent a challenge from the plasma magnetic control perspective. Different test cases are considered to assess the performance of the proposed shape controller, with the aim of defining an optimal set of gaps to be controlled. This

⁴ The time behavior of both β_p and l_i have been estimated starting from the spatial profiles for both plasma density and temperature envisaged for Scenario 2.

⁵ A compound ELM is commonly referred as multiple clearly distinguishable crash events causing large energy losses [63].

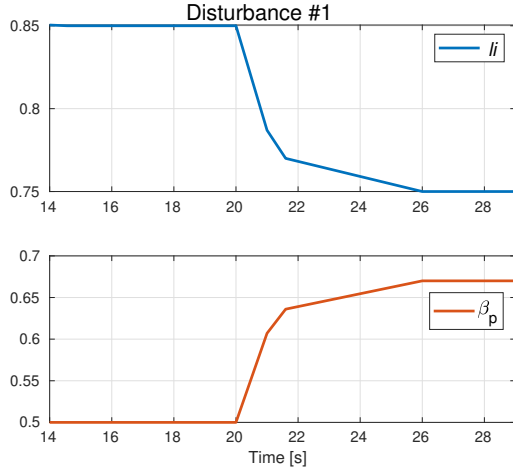


Figure 3.9.: Poloidal beta and internal inductance time traces for Disturbance #1 that models the expected disturbance soon after the plasma current flattop is reached (at $t \sim 20$ s), according to what has been considered in [62].

sections evaluates the steady-state performance of the plasma shape controller under different choices for *gaps* to be controlled.

All around the first wall an equally spaced distribution of 85 gaps was considered as shown in figure 3.5. It should be noticed that all different selections of controlled gaps considered in this paper include the two vertical gaps in the divertor zone, which allows to control the strike-points, and hence the position of the X-point. Other than the whole set of 85 gaps, three additional choices are considered. The first one is reported in figure 3.12a, which consists of 20 gaps equally spaced along the first wall. Moreover, the selection of 8 and 6 gaps that correspond with the control segments considered by the isoflux controllers presented in [64] and [65], respectively, have been also considered (see figures 3.12b and 3.12c). These two latter options are the outcome of preliminary studies aimed at controlling the plasma shape with a set of almost decoupled loops, i.e. SISO, while the XSC approach proposed in this section is intrinsically MIMO. Moreover, it is worth to remark that, although in [64] and [65] the 8 and 6 gap options have been used with an isoflux control approach, here the same control segments have been used to design the XSC adopting a gap-based approach.

The comparison between the various considered gap sets for the different disturbances test cases is summarized in Table 3.1. This table shows the *root-mean-square error* (RMSE) between the reference shape and the shape obtained at steady-state after the occurrence of the disturbances. For all the cases reported in Table 3.1, the RMSE has been computed on the set of 85 gaps shown in figure 3.5, even when not all of them are controlled.

It turns out that, according to this preliminary analysis, the rejection of the disturbances induced by the compound ELMs at steady-state is not an issue at JT-60SA, whatever is the set of gaps that is controlled. Indeed, figure 3.13 shows the RMSE time traces for Disturbance #2 (compound ELMs), being the RMSE computed on the set of 85 gaps shown in figure 3.5 for all the considered options. It turns



Figure 3.10.: Poloidal beta and internal inductance time traces for Disturbance #2 that models the behavior of these variables due to the presence of a compound ELM as defined in [51].

Steady-state RMSE mm				
	85 gaps	20 gaps	8 gaps	6 gaps
Disturbance #1	7.7	8.7	31.2	19.8
Disturbance # 2 (compound ELM)	~ 0	~ 0	~ 0	~ 0
Disturbance # 3 (Minor disruption)	6.1	7.8	26.9	16.3

Table 3.1.: Steady-state RMSE values for the different choices of number of controlled gaps and for the different disturbances test cases.

out that, whatever gap set is used, the controller has almost the same behavior, with a slightly worse performance of the 6 and 8 gap options. Being a periodic disturbance, the compound ELMs have been applied only during the first part of the simulation, in order to evaluate the steady-state performance of the controller. However, from figure 3.13 it can be noticed that the rejection of the compound ELMs is not a concern even during the transients, being the maximum RMSE ~ 2 mm.

For the other two considered cases, at steady-state, the selection of 85 and 20 gaps have a considerable better RMSE in comparison with the selection of 8 and 6 gaps. As outlined in Table 3.1, the worst case corresponds to the selection of 8 gaps with the presence of Disturbance #3 (Minor disruption) during the flattop. As an example, figure 3.15 shows a comparison of the steady-state shape obtained for the 8 and 20 gaps options when the Minor disruption is considered. Figure 3.14 shows the RMSE time traces for this disturbance and it can be noticed that the 20 gaps option gives better results with respect to the 8 and 6 gaps cases also during the transient, and not just in steady-state. In particular, in the 6 and 8 gaps cases, being the number of controlled gaps less than the number of the actuators available for plasma shape control, the steady-state error on the controlled gaps is practically zero. However, not being these two sets of gaps *well representative* of the whole plasma boundary, minimizing the error on such sets does not minimize the error on the whole boundary, as shown in figure 3.14.

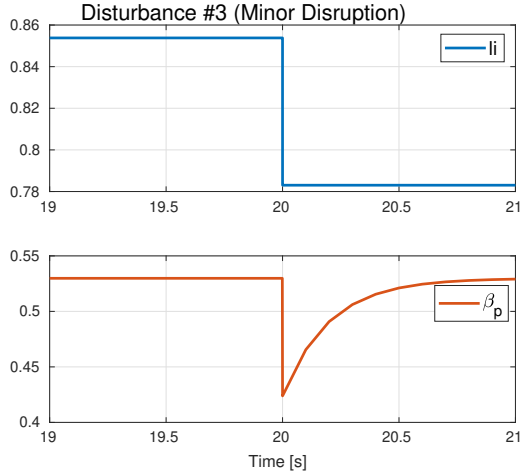


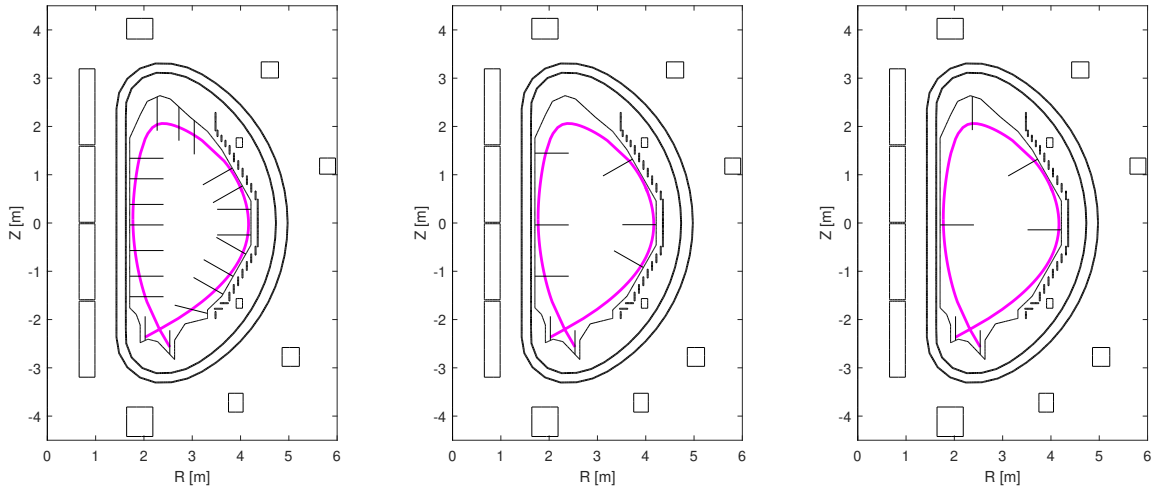
Figure 3.11.: Poloidal beta and internal inductance time traces for Disturbance #3 that models the behavior of these variables due to the presence of a Minor disruption as defined in [51].

It should be also noticed that the 6 gaps option considered in [65] gives better performance than the set of 8 gaps chosen in [64]. Indeed, with the latter set, there is a worse control of the plasma top region, as shown in figure 3.15b. Moreover, for the two options with 85 and 20 equally spaced gaps there is no practical difference between the reference shape and the one attained at steady-state. The fact that there is no practical improvement in controlling 85 gaps rather than 20, can be better understood recalling that $\bar{n} < n_{PF}$ singular values are used to compute the control matrix as the pseudo-inverse C^\dagger in (3.1). In particular, only the singular values that are greater than the 5% of the greatest one are used to compute C^\dagger .

3.5.3 Isoflux XSC and QST controller

As mentioned in the previous section, simulations with an iso-flux control approach using the CREATE linearized model and the XSC along with the QST reconstruction and control tools were carried out. The same three disturbances (see figure 3.9, 3.10 and 3.11) and JT60-SA equilibrium scenario from the simulations in last section were used for these test cases for a different number of control points. Due to the vast extension of results, this section will focus on analyze the case for 8 control points in the presence of a Minor disruption with the XSC and the QST controller. Figure 3.16 shows the control points configurations used for carrying out the simulations with an iso-flux shape controller as well as the LCFS's reconstructed by CREATE and the CCS method at steady-state in the presence of a Minor disruption(Disturbance #3).

For the control and reconstruction points configurations a selection of 19 equally spaced descriptors was used (see figure 3.16a), along with the previous 8 and 6 points configurations used for the gap controller. As mentioned before, the CCS method allows a maximum of 19 points for the fluxes reconstruction



- (a) The 20 gaps used to assess the performance of plasma shape controller.
(b) The 8 control segments by the isoflux controller proposed in [64].
(c) The 6 control segments used by the isoflux controller proposed in [65].

Figure 3.12.: Different choices for the set of controlled gaps used for gap controller.

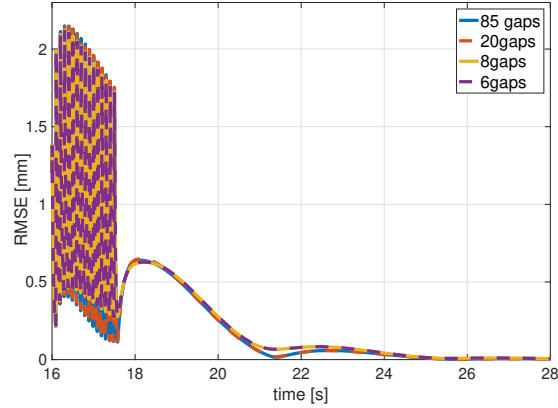


Figure 3.13.: RMSE time traces for the different gaps selections in the presence of Disturbance #2 (compound ELMs). For all the considered cases, the RMSE is computed on the set of 85 gaps shown in figure 3.5.

and the QST controller a maximum of 10 control points, due to these limitations the 19 segments scenario is only feasible using the XSC.

Figure 3.17 compares the steady-state LCFS's for the same disturbance and equilibrium using both controllers, at first glance it is not possible to identify any visible difference between the two controllers, which allows a first conclusion that both controls reject the disturbance and maintain the reference plasma shape in steady-state. For further study in figures 3.18a and 3.18b is presented the behavior of both controllers at the time instant where their fluxes errors are on their highest value, this happens around 2 ms for the case of the XSC and 65 μ s for the QST control after the Minor disruption takes place. From these figures is possible to observe that there is a noticeable plasma shape difference in



Figure 3.14.: RMSE time traces for the different gaps selections in the presence of Disturbance #3 (Minor disruption). For all the considered cases, the RMSE is computed on the set of 85 gaps shown in Fig. 3.5.

comparison with the one from the equilibrium, specially on the radial outer region and secondly is visible that the difference between the equilibrium and the steady-sate shape is smaller for the QST controller case.

Figure 3.19 shows the time traces comparing the flux at the X-point and the 8 control points fluxes, for the XSC and the QST control cases. From these two graphs is noticeable that the QST controller takes around 0.5 s more to reach the steady-state after the disturbance takes place than XSC , but the fluxes at the control points reach a state-state flux value way closer to the X-point flux than the fluxes using the XSC for the simulation, in addition figure 3.20 shows the flux error time traces on the 8 control points for both controllers, on these plots is worth to mention that additionally to a smaller state-state error using the QST control, the maximum error values which are located right after the disturbance takes place are higher for the simulation using the XSC.

In order to summarize all the results from the tested cases, tables 3.3 , 3.5 and 3.7 outline the control points fluxes RMSE and tables 3.3, 3.5 and 3.7 present the X-point radial and vertical position errors in steady-state, these tables summarize results for all the different number of control points with the three different disturbances. Some of the main aspects that are possible to conclude from the tables results are :

- (a) For all disturbances the 8 control points selection has the biggest fluxes and X-point position steady-state errors while the cases with 19 control points the lesser ones.
- (b) Disturbance #2 (Compound ELM) results present the lesser flux RMSE values in comparison with the other two disturbances. See table 3.4.
- (c) The simulations using the QST controller present practically a flux RMSE equal to zero in steady-state for all disturbances while the XSC does not.

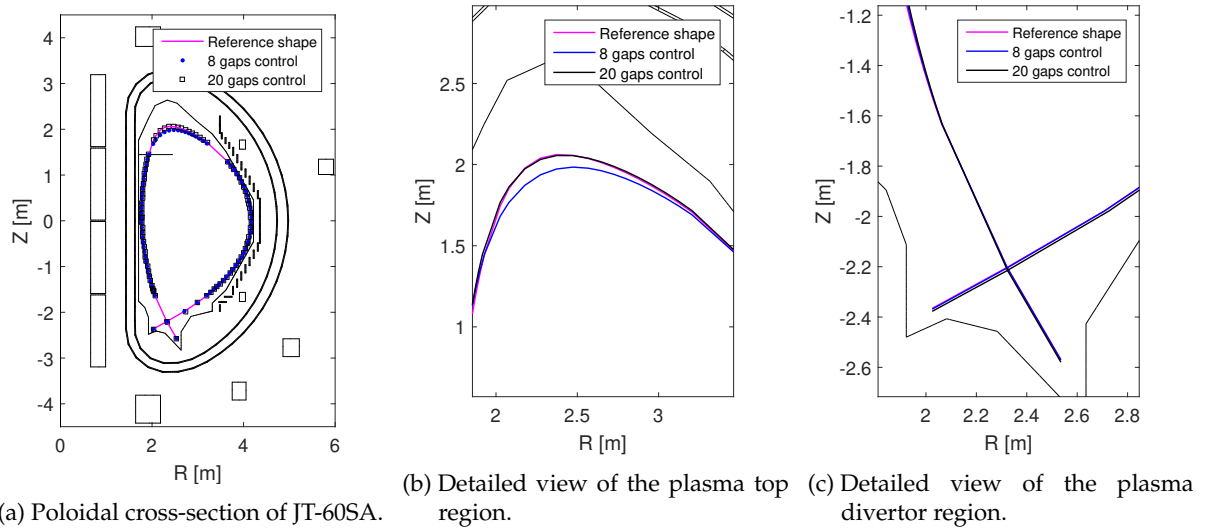
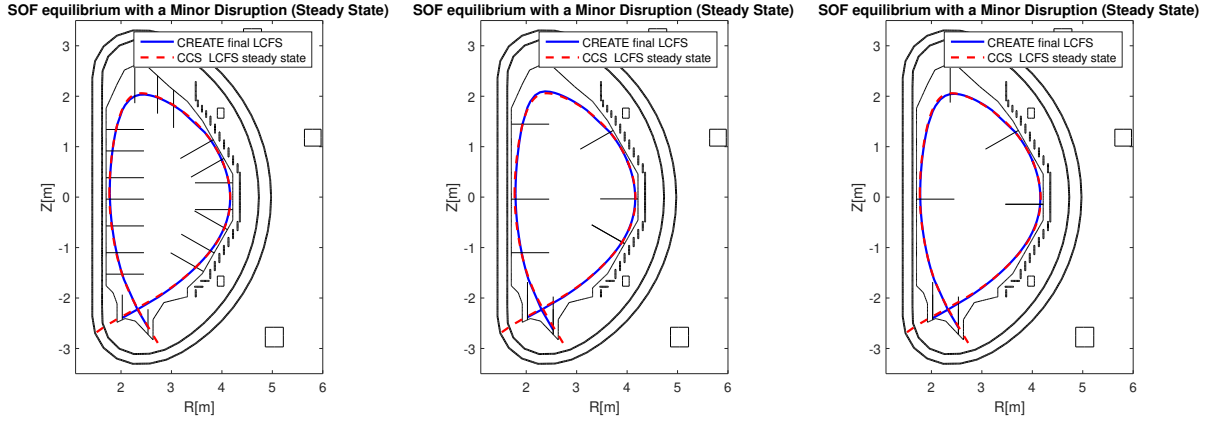


Figure 3.15.: Comparison of the shape controller performance in the presence of Disturbance #3 (Minor disruption). The two cases of 8 and 20 gaps are considered.

Disturbance #1 flux RMSE steady state		Wb/ 2π	
Controller	eXtreme Shape Controller	QST Controller	
LCFS reconstruction method	CCS	CREATE	CCS
6 points	0.0116	0.0133	~ 0
8 points	0.0166	0.0181	~ 0
19 points	0.0085	0.0088	

Table 3.2.: Steady-state flux RMSE values for the different selection of control points for the JT60-SA scenario 2, SOF equilibrium in the presence of Disturbance #1 at $t \sim 20$ s.

- (d) For all the scenarios the vertical XSC X-point error is at least %30 greater than the radial position error, while for the QST control the vertical position error tends to be around %50 lesser than the radial position.
- (e) As mentioned on the previous section and as it can be observe on the scheme in figure 3.7, the XSC isoflux approach also controls the X-point position, this is noticeable for all the disturbances with 8 control points, where the vertical and horizontal position error values with the QST controller are at least 50% greater than the ones with the XSC .
- (f) Despite the X-point control dynamics embedded on the XSC, for the 6 control points scenarios, the radial X-point error positions are similar between the XSC and the QST control simulations, and the vertical X-point error using the XSC is for all disturbances at least 10 times greater than the simulations with the QST controller.



- (a) The 19 control segments used to assess the performance of plasma shape controller.
- (b) The 8 control segments by the isoflux controller proposed in [64].
- (c) The 6 control segments used by the isoflux controller proposed in [65].

Figure 3.16.: LCFS reconstructed by CREATE and the CCS code for the JT60-SA scenario 2 SOF equilibrium with a Minor disruption at steady-state for the three considered selection of control segments using the XSC with an isoflux approach.

Disturbance #1 steady state X-point position error									
Controller	eXtreme Shape Controller				QST Controller				
LCFS reconstruction method	CCS		CREATE		CCS		CREATE		
	Rx mm	Zx mm	Rx mm	Zx mm	Rx mm	Zx mm	Rx mm	Zx mm	
6 points	-4.606	19.96	-3.576	28.16	-1.434	-0.843	-1.16	-0.316	
8 points	18.58	21.95	18.96	29.82	49.16	-46.52	59.66	-40.92	
19 points	2.62	12.84	2.375	20.51					

Table 3.3.: X-point position steady state error for JT60-SA scenario 2, SOF equilibrium in the presence of Disturbance #1 at $t \sim 20$ s. The XSC and QST controller were used in different simulations for the shape control along with two reconstruction methods for the LCFS.

3.5.4 Shape reference change

A change in the plasma shape for the Scenario 2 - SOF equilibrium has been also considered. In this test scenario closed-loop simulations with the CCS reconstruction method and the isoflux XSC for the plasma shape were performed. Since the configuration with 8 control points seems to be for all cases the one most challenging due to the error values in steady-state obtained on the past subsection, these selection of control points was used for this simulation. The transition time from the initial shape to the target was set equal to 1.5 s. Figure 3.21 shows the equilibrium LCFS (Scenario 2 -SOF), the desired target shape and the LCFS at steady state reconstructed by the CCS method. It can be noticed that the controller is able to track the required shape with negligible error at steady-state, taking ~ 6 s to reach to it. Figure 3.22 shows the time traces for the fluxes at the 8 control points compared with the X-point flux and figure 3.23 shows the correspondent control flux errors.

Disturbance #2 (Compound ELM) flux RMSE steady state Wb/2π			
Controller	eXtreme Shape Controller	QST Controller	
LCFS reconstruction method	CCS	CREATE	CCS
6 points	0.0014	0.0022	~ 0
8 points	0.0104	0.0101	~ 0
19 points	0.0023	0.0028	

Table 3.4.: Steady-state flux RMSE values for the different selection of control points for the JT60-SA scenario 2, SOF equilibrium in the presence of Disturbance #2 (Compound ELM) at $t \sim 20$ s.

Disturbance #2 (Compound ELM) steady state X-point position error								
Controller	eXtreme Shape Controller				QST Controller			
LCFS reconstruction method	CCS		CREATE		CCS		CREATE	
	Rx mm	Zx mm	Rx mm	Zx mm	Rx mm	Zx mm	Rx mm	Zx mm
6 points	0.3968	-2.455	1.3	2.556	-0.481	-0.267	-0.019	0.0143
8 points	15.72	-8.41	16.61	-3.098	50.18	-43.25	54.44	-32.68
19 points	-0.0007	0.0237	-0.1916	-4.69				

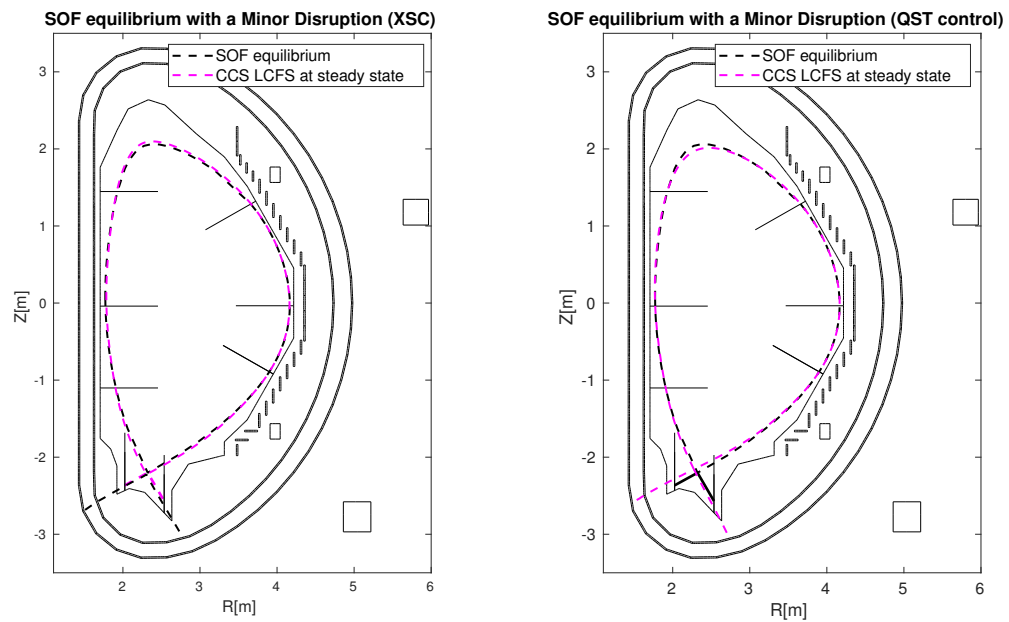
Table 3.5.: X-point position steady state error for JT60-SA scenario 2, SOF equilibrium in the presence of Disturbance #2 (Compound ELM) at $t \sim 20$ s . The XSC and QST controller were used in different simulations for the shape control along with two reconstruction methods for the LCFS.

Disturbance #3 (Minor disruption) flux RMSE steady state Wb/2π			
Controller	eXtreme Shape Controller	QST Controller	
LCFS reconstruction method	CCS	CREATE	CCS
6 points	0.0121	0.0139	~ 0
8 points	0.0152	0.0170	~ 0
19 points	0.0069	0.0088	

Table 3.6.: Steady-state flux RMSE values for the different selection of control points for the JT60-SA scenario 2, SOF equilibrium in the presence of Disturbance #3 (Minor disruption) at $t \sim 20$ s.

Disturbance #3 (Minor disruption) steady state X-point position error								
Controller	eXtreme Shape Controller				QST Controller			
LCFS reconstruction method	CCS		CREATE		CCS		CREATE	
	Rx mm	Zx mm	Rx mm	Zx mm	Rx mm	Zx mm	Rx mm	Zx mm
6 points	-4.92	20.9	-3.57	28.8	-2.70	-0.105	-2.24	0.369
8 points	17.44	21.56	17.81	29.04	47.08	-46.56	57.61	-41.42
19 points	-5.54	16.78	-4.42	24.41				

Table 3.7.: X-point position steady state error for JT60-SA scenario 2, SOF equilibrium in the presence of Disturbance #3 (Minor disruption) at $t \sim 20$ s . The XSC and QST controller were used in different simulations for the shape control along with two reconstruction methods for the LCFS.



(a) Comparison between the reference shape (i.e., the shape at the considered equilibrium) and the LCFS reconstructed by the CCS code at steady-state in the presence of the Minor disruption using the XSC for the plasma shape, when 8 control segments are considered.

(b) Comparison between the reference shape (i.e., the shape at the considered equilibrium) and the LCFS reconstructed by the CCS code at steady-state in the presence of a Minor disruption using the QST controller for the plasma shape and current and 8 control segments .

Figure 3.17.: CREATE-NL JT60-SA Scenario 2 - SOF equilibrium compared with the LCFS reconstructed by the CCS method for 8 control points in the presence of a Minor disruption at steady-state using both the XSC and the QST control.



Figure 3.18.: CREATE-NL JT60-SA Scenario 2 - SOF equilibrium compared with the LCFS reconstructed by the CCS method for 8 control points in the presence of a Minor disruption (Disturbance #3) at the time of maximum deviation for both cases. As shown in figure 3.11, the disturbance occurs at $t \sim 20$ s

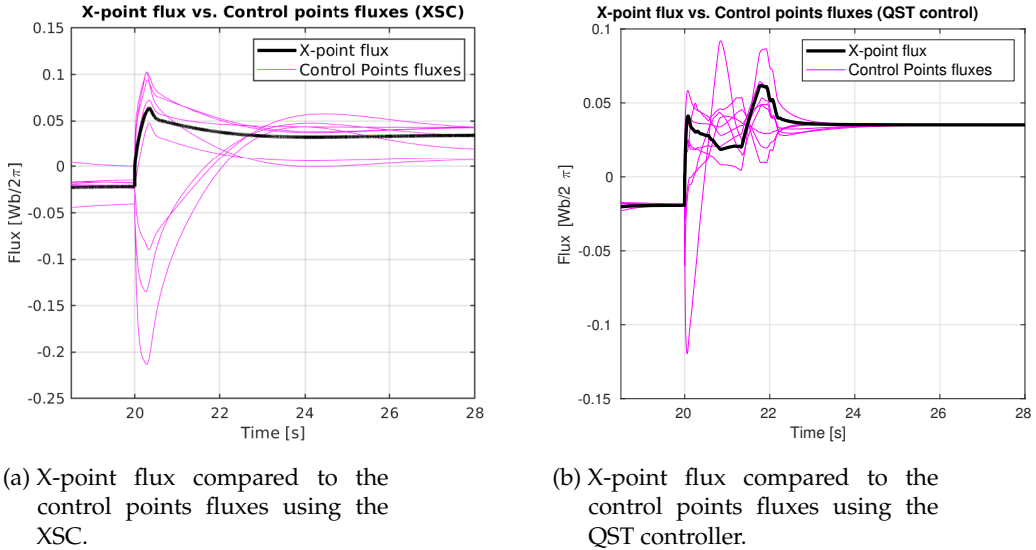


Figure 3.19.: Comparison between the flux at the X-point and the fluxes in the 8 control points reconstructed by the CCS method, when a Minor disruption is applied at $t=20$ s using the XSC and the QST controller. It should be noticed that QST control has a faster performance to reach the steady-state and less error.



(a) Flux errors using the XSC for 8 control points in the presence of a Minor disruption starting at $t = 20$.

(b) Flux errors using the QST controller for 8 control points in the presence of a Minor disruption starting at $t = 20$.

Figure 3.20.: Flux errors for the case of 8 control points in the presence of a Minor disruption using the XSC and the QST controller. Even though both controllers reject the disturbance, is possible to remark how the QST control has an overall smaller error.



Figure 3.21.: XSC isoflux response to a change of shape request. The dashed black shape is the starting shape, while the red one is the target shape. The magenta dashed shape is the LCFS at steady state.



Figure 3.22.: Comparison between the flux at the X-point and the fluxes a

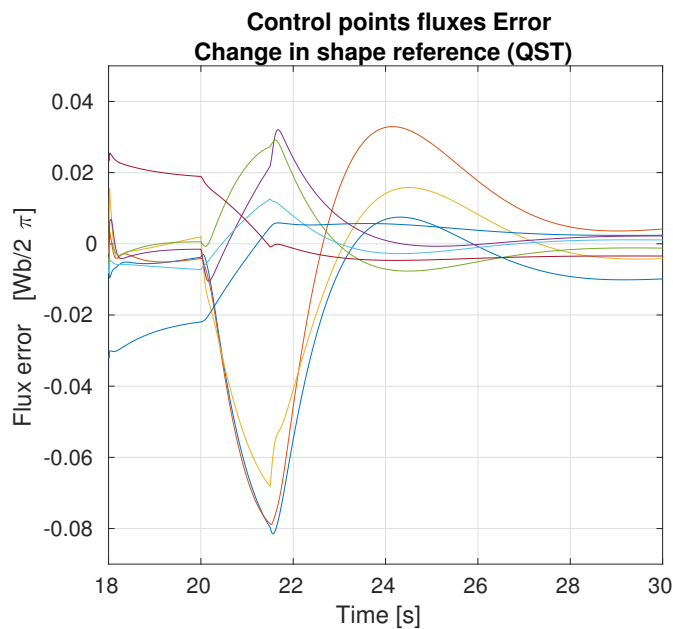


Figure 3.23.: Flux control error for the case of 8 control points for a change in the shape reference between 20 and 21.5 s.

4

ISTTOK

ISTTOK is a large aspect ratio tokamak (IPFN-IST, Lisbon, Portugal) operating for 30 years and which has been in constant upgrading of diagnostics, hardware acquisition system and control algorithms (major and minor plasma radius are respectively $R = 46\text{ cm}$, $a = 8.5\text{ cm}$). Together with the JT60-SA development of control techniques from last chapter, ISTTOK studies complement as a whole this work. This chapter will detailed how ISTTOK operates, from topics such as describing its diagnostics to description of the reconstruction method for calculating the plasma centroid position.

4.1 MACHINE DESCRIPTION

The construction of the actual ISTTOK machine was started in 1990 reusing some parts of the former dutch TORTUT tokamak: support structure, vacuum vessel, copper shell, toroidal magnetic coils, transformer, capacitor banks, radiofrequency (rf) generator, and discharge cleaning system [66]. The toroidal magnetic field is given by a set of 24 conventional coils which generate a maximum of 3 T. The other components of ISTTOK such as the vacuum systems, the PF coils, and the power supply for the toroidal magnetic coils, as well as its diagnostics and control and data acquisition system, were locally designed and built. Figure 4.1 shows a top view of the ISTTOK tokamak and figure 4.2 a frontal one in early 2020, its main elements are signalized with arrows.

Figure 4.3 corresponds to a section of the ISTTOK vacuum vessel, it is possible to observe on the image the ribbed surface from the vessel and some of the ports on the top of it. The vacuum vessel is formed by two half torus made of INCONEL alloy 625 with a thickness of 0.15 mm. The vacuum vessel is completely surrounded by a 1.5 cm thick cooper shell which is possible to see in the images from figure 4.6, this shell supports the vacuum vessel and it originally also worked suppressing variations of the plasma position in less than 2 ms since a first version of TORTUR had no PF coils, this was a form of auto-control. The cooper shell, due to its properties, adds a delay or skin time for the penetration of the magnetic fields into the vacuum vessel.



Figure 4.1.: ISTTOK top view in 2020, main elements are indicated with magenta lines.



Figure 4.2.: ISTTOK frontal view in 2020, main elements are indicated with blue lines.



Figure 4.3.: Actual ISTTOK inconel vacuum vessel section with ports.

4.1.1 ISTTOK AC plasma current

The STOR-M tokamak was the first device to demonstrate an alternation in the plasma current even though the control position for negative cycles was not very successful [67], afterwards in JET, plasma current reversal was implemented as a necessity to demonstrate the feasibility of AC operation in conditions which can be considered relevant to a reactor achieving plasma current of 2 MA in each direction along with modifications in the PF coils powers supplies control systems [68].

One of the main characteristics from ISTTOK is that due to the flexibility of the power supplies it is possible to perform AC discharges which allow the fast reversal of the plasma current while maintaining a finite plasma density between consecutive flat tops [69]. The current inversions make it possible to achieve a much longer plasma duration in comparison to single mode operation, which is limited by the saturation of the iron core magnetization, the plasma duration is of approximately 1 s with positive and negative flaptops of $\approx 25\text{ ms}$ ([70], [71]). An AC plasma current also accounts for an inversion in the direction of the poloidal magnetic field, from the equation 1.6 is possible to see that a change of sign in the poloidal field B_θ while the toroidal field B_ϕ remains the same only implies a change of sign in the required vertical field for achieving toroidal force balance. ISTTOK has dwell time in between positive and negative cycles of $\approx 1\text{ ms}$.

4.2 DIAGNOSTICS AND ACTUATORS

Different diagnostics are integrated in ISTTOK to retrieve important plasma parameters, i.e. langmuir probes, tomography, magnetic probes. This work is focused on the magnetic diagnostics since they are responsible for retrieving the signals necessary to reconstruct the centroid position of the column and the plasma current. ISTTOK has a set of 12 of magnetic probes or Mirnov coils positioned along the poloidal direction (30° between probes), each coil has an area of 49 mm^2 , 50 turns and a length of 5 mm, a scheme is depicted in figure 4.4a. Picture from figure 4.6a shows the vessel side port where the magnetic probes are placed and its acquisition cables along with some of the PF coils cables in orange and white. Each coil is inside a graphite box and the set of 12 forms the plasma limiter, see figure 4.4b and 4.4c. Magnetic probes send an induced voltage given by Faraday's law $\varepsilon = -N \frac{\Phi_p}{dt}$ where Φ_p is the poloidal magnetic flux generated by the plasma and passive elements passing through the probe cross-section.

A second set of diagnostics important for this work are the three current transducers, also called LEMs, installed in ISTTOK for measuring the current applied by the power supplies to each PF coils, figure 4.5 show a picture of one LEM.

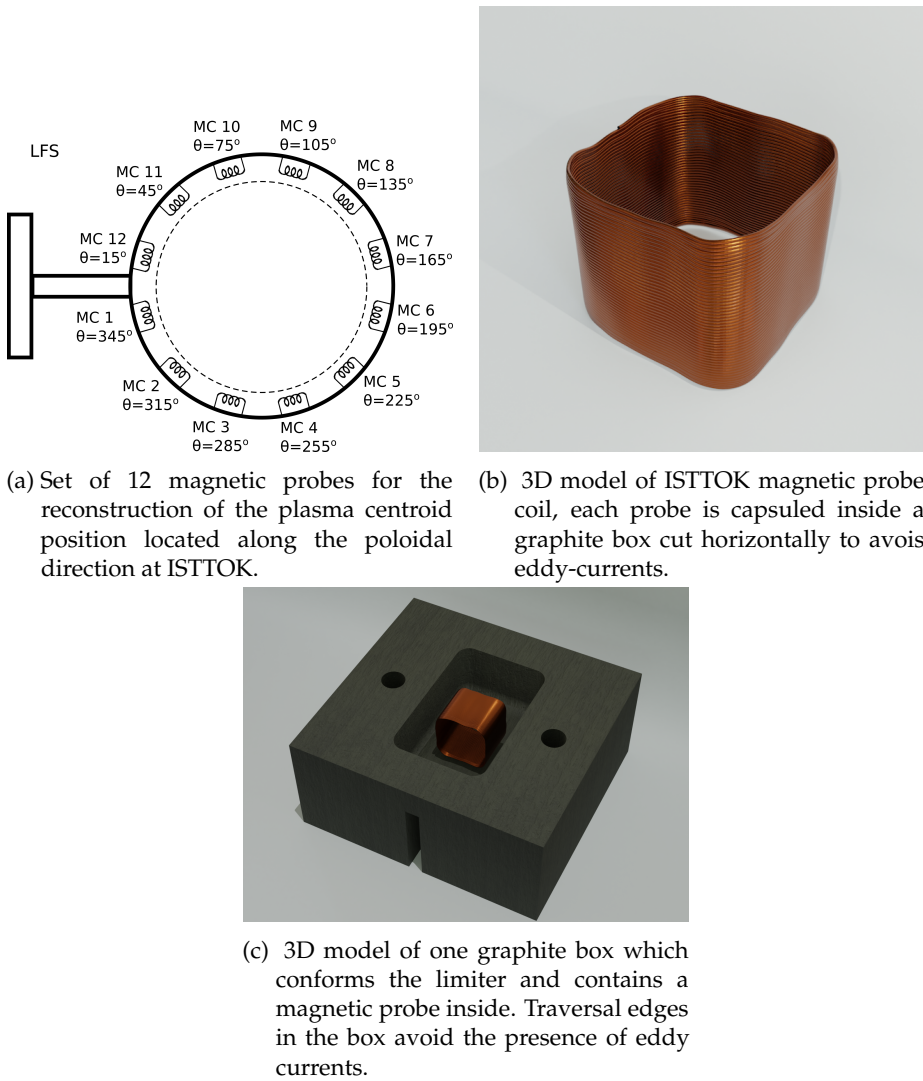


Figure 4.4.: ISTTOK magnetic probes.

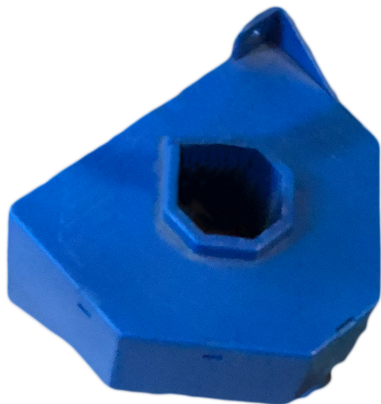


Figure 4.5.: LEM transducer for measuring the current from the power supplies to the PF coils.



(a) Magnetic probes port with connection cable to the ATCA acquisition boards, also PF coils and cooper shell are shown.
(b) PF coils close up, primary coils correspond to the white cables and vertical and horizontal to the orange ones.

Figure 4.6.: ISTTOK close up side views.

4.2.1 Poloidal Field Coils

ISTTOK poloidal field coils are placed in between the TF coils and the cooper shell. In figures 4.6a and 4.6b is possible to see the cables from the PF coils arrange in sets of orange and white cables. ISTTOK Poloidal Field (PF) coils are connected to three independently feedback controlled power supplies for the purpose of generating plasma current and also to control vertically and horizontally its centroid position. In figure 4.7 is shown on the right side of the iron core an old central solenoid which used to be responsible for plasma current generation, this element is currently disconnected. The primary PF coils, in white color, generate ohmic heating for the creation of plasma current and an additional vertical field. In yellow is depicted the vertical PF coils and in green the horizontal PF coils, both controlled by different control algorithms in order to follow a centroid position set point [72]. The PF coils power supplies have as saturation limits $I_{sat-prim} = \pm 300 A$, $I_{sat-vert} = \pm 400 A$ and $I_{sat-hor} = \pm 200 A$. Figure 4.8 shows the magnetic field lines generated by each PF coil around the vacuum chamber cross section on their nominal positions:

- Primary PF coils: 2 coils, 14 turns, ($R_{1,2} = 62 cm$, $z = 13 cm \pm$).
- Vertical PF coils: 4 coils, 5 turns, ($R_{1,2} = 58 cm$, $R_{3,4} = 34 cm$, $z = 7 cm \pm$).
- Horizontal PF coils: 2 coils, 4 turns, ($R_{1,2} = 58 cm$, $z = 7 cm \pm$).

As mentioned before, figure 4.7 shows the nominal positions of the PF coils. From the pictures in figure 4.6 is notorious that specially the vertical and horizontal PF coils (orange cables) are not uniformly



Figure 4.7.: 3D model of the ISTTOK PF coils, vacuum chamber with ports, iron core and the former central solenoid (black color). Primary coils (white color) and horizontal coils (green color) are formed by 2 coils each one and located on the upper and lower LFS (Low Field Side) of tokamak. Vertical coils (yellow color) are formed by 4 coils, 2 are located on the upper and lower LFS and 2 in the upper and lower HFS (High Field Side).

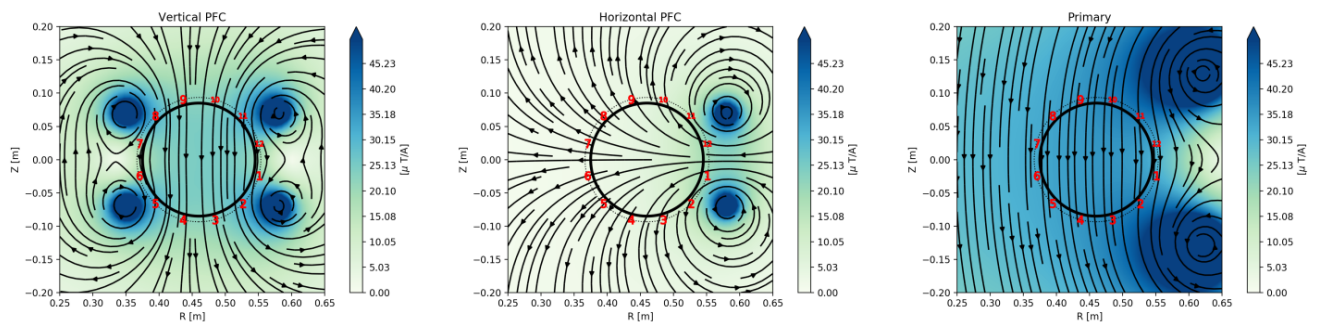


Figure 4.8.: Magnetic field generated by the active coil circuits on their nominal positions. Mirnov positions are represented by its sequential number (in red) over the dashed line. Black circle represents the limiter.

arranged, toroidally not very axisymmetric and they seem to have a general negative offset in the vertical coordinate, on top of that there is no certain notion of how the internal vertical coils have moved through the years, this represented and issue attempting to adjust a theoretical ISTTOK model based on the CREATE codes.

4.3 ISTTOK HARDWARE

ISTTOK real-time control diagnostics and actuators implementation rely on the recently upgraded hardware based on the Advanced Telecommunications Computing Architecture (ATCA). The real-time control system is programmed on top of the Multi-threaded Application Real-Time executor (MARTe) framework, which integrates and processes the information gathered by all the diagnostics [73], figure 4.9 depicts the schematic of the implemented control system at ISTTOK.

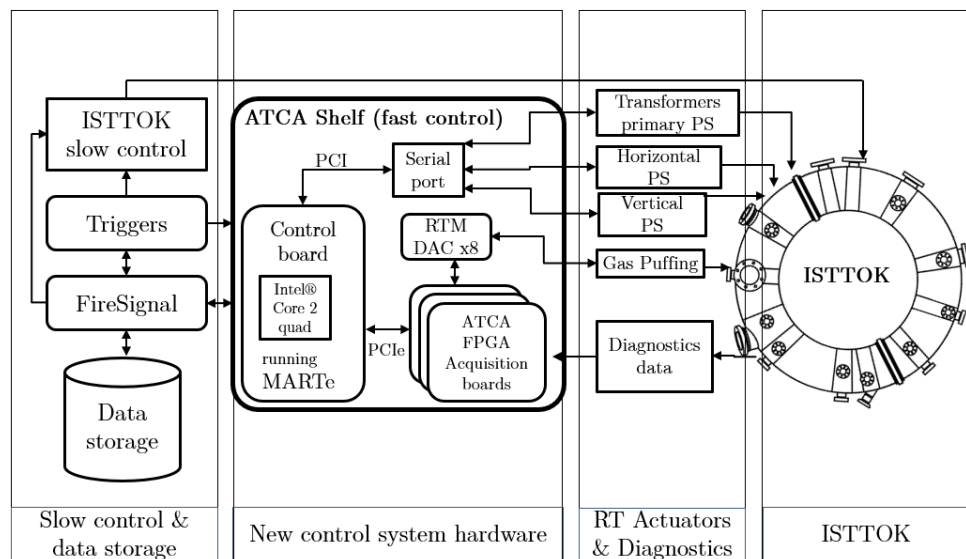


Figure 4.9.: ISTTOK hardware overall scheme. Data is acquired by the ATCA data acquisition boards, and decimated and transferred to the hosts every $100\ \mu s$.

Recently implemented hardware-integrated acquisition of the magnetic probes signals at ISTTOK allowed the implementation of new real-time algorithms for an accurate reconstruction of the current centroid position.

4.3.1 ATCA-MIMO-ISOL boards

The ATCA carrier board, already slightly address in chapter 2, is an IPFN developed board [74] complying with the ATCA standard specification, highly modularized, and with an optional Rear Transition Module (RTM) . The carrier board can hold up 32 analog input channels, each connected

to a plugged-in ADC module. All modules are connected digitally to a XILINX Virtex-4 FPGA which performs necessary digital signal processing and includes a PCI Express Endpoint providing the data interface to the ATCA switch board. Figure 4.10 shows a newer version from the board in figure 2.6, both share basically the same elements. The latest version of the ATCA-MIMO-ISOL boards built in IPFN where mainly intended for the magnetic acquisition in the stellerator W7-X and lately tested in ISTTOK.

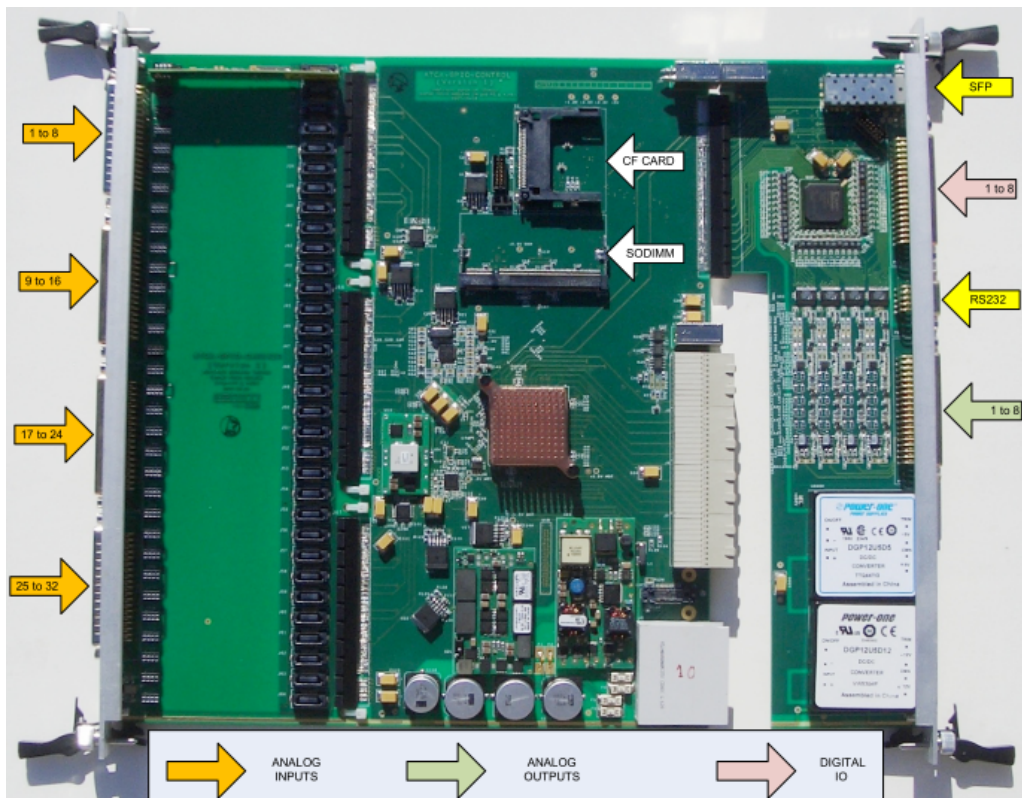


Figure 4.10.: General view of the ATCA-MIMO-ISOL carrier board, including on the right side an original IPFN RTM board joined through an edge connector.

The phase modulated (chopper) ADC module [74] was designed targeting the digital integration of signals generated by magnetic coils, over periods of time larger than one hour. The ADC module is composed by a Signal Condition block with a passive filter attenuator and active differential amplifier, the ADC block (18-bit resolution, fixed 2MSPS(Mega samples per second)), a DC-DC converter and Magnetic Isolation coupler (ILS711-S1) and finally the digital interface to the FPGA in the ATCA carrier Board. The FPGA also provides the clock signals for the DC-DC converter, the chopper and ADC clock (common to all channels) and receives the serial ADC data and respective clock signals.

4.4 REAL-TIME INTEGRATION SOFTWARE

To recover the magnetic fields absolute magnitude from inductive probe signals an integrating component is needed. Typical analog electronic integrator circuits always suffer from voltage offsets and drifts present in the components and wiring. Even very low offsets integrated during a long period of time may appear as a noticeable deviation of the integrated signals [75] and eventually saturate their outputs. A solution chosen for this integrator design, previously demonstrated in a four channel prototype in PXI format [76], was to modulate signals with a phase invertor (chopper), which reverses periodically the input signal before active amplification (multiplies the signal by 1 and then by -1), filtering and sampling in the ADC, as shown in figure 4.11. The switching frequency is programmable and made synchronous with the sampling ADC 2Mhz clock, as both are generated in the same FPGA. By applying the signal inversion before any electronic amplification, and reconstructing the digital equivalent of the signal after the digitalization, the average of the electronics offset (EO) is expected to be almost zero in the integration process if its value is steady enough over at least two inversion periods. In addition a second offset also appears before the chopper, the Wiring offset (WO) which may be generated either inside the module or in the external wiring, connectors and soldered parts, mainly due to uncompensated thermocouple effects, external interference or radiation effects. Unfortunately, the WO is not averaged by the chopping method, since it goes across two signal reversions, and is typically much lower than either both EO or the ADC resolution, the process for removing the WO in real-time will be discussed ahead. From figure 4.11 the integration process can be inferred. Let's say the upcoming signal from the probe is $s(t)$, the sampled value is $V_{ADC}[n]$ and $t = nT_s$, where T_s is the ADC sampling period:

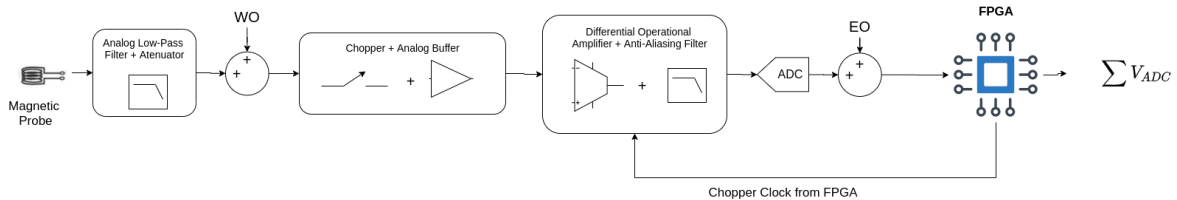


Figure 4.11.: ADC module diagram depicting the influence of the WO and EO offsets and the instrumentation since the magnetic probes signal it is acquired until its integration in the FPGA.

$$V_{ADC} = (s(nT_s) + WO) \cdot Ph_{chop}(nT_s) + EO \quad \text{V} \quad (4.1)$$

where Ph_{chop} is the phase signal of the chopper (1 or -1). Assuming $s(nT_s) \approx n[T]$ and $Ph_{chop}(nT_s) \approx Ph_{chop}[n]$, the phase reconstructed signal from the magnetic probe can thus be approximated from the discrete samples using:

$$s[n] \approx (V_{ADC} - EO) \cdot Ph_{chop}[n] - WO \quad \text{V} \quad (4.2)$$

Assuming the ADC sampling frequency is sufficiently higher than double of signal bandwidth, the integral related to magnetic fluxes can then be approximated by the expression:

$$\Phi(t = nT_s) = \int_0^{t=nT_s} s(t)dt \approx \sum_0^N ((V_{ADC}[n] - EO) \cdot Ph_{chop}[n]) - nT_s \cdot Wo \quad \text{V} \cdot \text{s} \quad (4.3)$$

Thus, the V_{ADC} summation for approximating the integral of the signals acquired from the magnetic diagnostics is computed in the FPGA and then sent to the MARTe database via PCI-express.

Even though WO removal is a common feature in processing magnetic data it is remarkable the flexibility ISTTOK gives by allowing the calculation of the offset prior to each discharge. In contrast with other experiments where the offsets do not tend to change and have to be calibrated one single time, due to the physical conditions in ISTTOK the offset values are in constant change and so they should be calculated on real-time prior to every discharge. Figure 4.12 shows the WO percentage change in the magnetic probe # 10 in 2019, it is possible to observe that in most of the shots the changing percentage is of at least $\approx 30\%$, figure 4.13 shows the WO values and percentage changes for a less number of shots on the magnetic probe #10, this shot numbers correspond to data acquisitions where the WO had the smallest changes, from these figures is possible to conclude that is needed a real-time algorithm to calculate the WO on each probe prior to a plasma discharge.

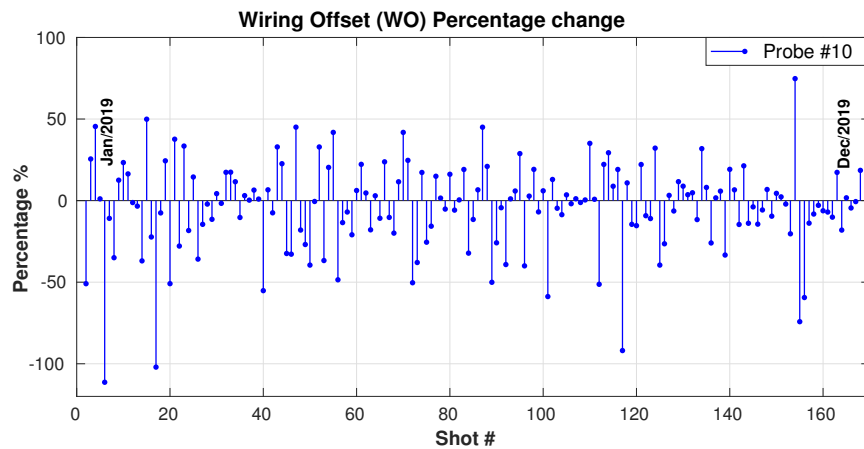


Figure 4.12.: WO percentage change in the magnetic probe # 10 in 2019 using data from approximately 180 shots distributed during the entire year.

At ISTTOK it is possible to acquire data using the MARTe framework. Even though the probes signals before the discharge starts are not stored on the data base, this feature allows to compute the WO of each probe several seconds before the discharge starts. For this process a GAM stores the signal from each integrated magnetic probe and calculates the slope from $t = 0$ until $t = 1$ s, repeats this process every second during 30 s and calculates an average WO value for each coil. The WO value obtained is then subtracted on every MARTe iteration once the discharge starts from the actual probe signals. In figure ?? it is possible to observe the integrated WO summed to the probe signal.

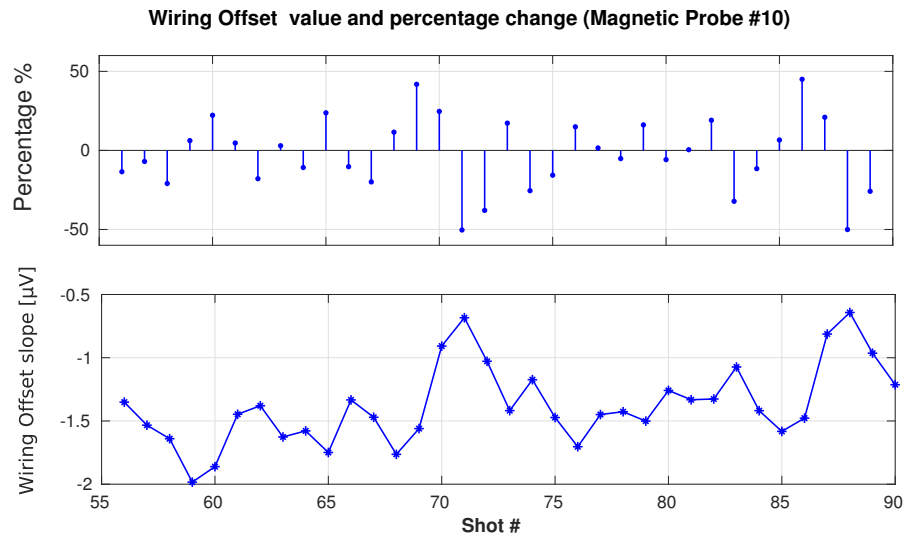


Figure 4.13.: WO and percentage change in the magnetic probe #4 throughout 45 shots in ISTTOK.

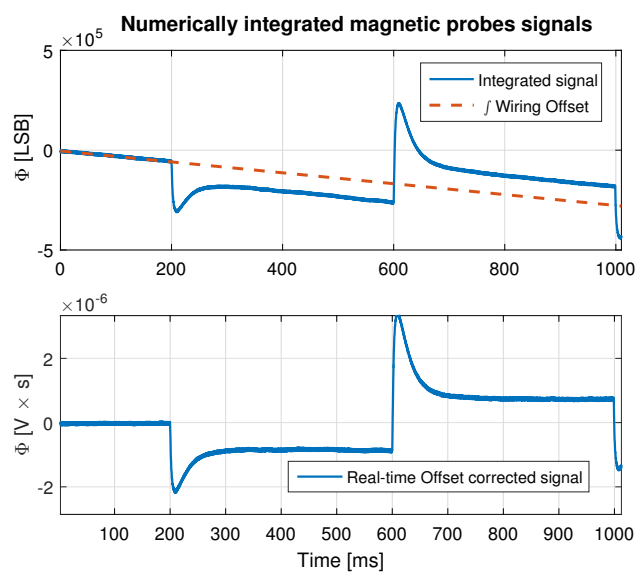


Figure 4.14.: Real-time subtraction from the integrated WO is performed on every MARTe cycle for each magnetic probe.

4.5 PLASMA CURRENT MAGNETIC FIELD

Retrieving the contribution of the plasma current in tokamaks can be achieved through the integrated magnetic probes signals. The magnetic probes are exposed to any poloidal field present in their surrounding which are: poloidal field generated by I_p , poloidal field generated by the PF coils and field generate by the eddy currents in the passive structures. Reconstructing the plasma centroid position from the signals in the magnetic probes implies that a process should be perform in order to extract only the plasma current magnetic contribution to the probes. On this section the methods of correction of the magnetic external fields due to PF coils, inaccuracies of tokamak manufacturing and assembly are considered.

4.5.1 PF coils state-space model estimation

Since currently the PF coils positions are not similar to the nominal ones and due to its physical configuration is hard to measure their positions and clearly identify the cables from each coil, the attempts to create a theoretical model for ISTTOK did not succeeded. Even though this fact could have brought a barrier for characterizing ISTTOK, this situation allowed to use different approaches and apply computational tools never used in order to implement novelty deployments in ISTTOK.

Performing plasma-less discharges in ISTTOK by applying different step functions waveforms in the PF coils currents, data-driven discrete state-space models were obtained in order to determine the contribution to the probes signals from passive-structures eddy currents and PF coils fluxes at any instant. Due to the linear dynamics of the PF coils and the simplicity for implementing the state-space equations on top of MARTe framework it was decided to use state-space models for the reconstruction of external contributions [40, Chapter 2].

The modelling process was done using the *System Identification Toolbox* from MATLAB [47, Chapters 2,3], the equations and algorithms used for retrieving the model parameters have already been described in section 2.4.5. Each magnetic probe possess a set of three state-space models associated to the magnetic contribution from the vertical, horizontal and primary PF coils. The extraction of magnetic measurements related only with the plasma are used to calculate and accurate reconstruction of the centroid position.

Figure 4.15a and 4.15b show the results obtained in one of the magnetic probes during the modeling process and the accuracy of the models for estimating the effect of plasma-less fluxes during a discharge. The signals shown in figure 4.15a were used as source information for calculating the state-space models while the figure 4.15b depicts the accuracy of the applied models in a vacuum discharge.



Figure 4.15.: Fig. 4.15a Response of the integrated and offset corrected signal in shot #44480 from magnetic probe #3 (red) used for obtaining data-driven models of the external fluxes. Reconstruction of the experimental signal through the data-driven model is shown in black. Fig. 4.15b Response of the magnetic probe #3 (orange) to a plasma-less discharge (shot #44632) with different current waveforms in the PF coils. Post-process reconstruction of the signal probe using the models already obtained is shown in orange.

4.6 PLASMA CENTROID POSITION DETERMINATION

The problems of the plasma position and shape reconstruction based on magnetic field measurements are discussed in this section. The vertical and radial plasma position centroid measurements are essential and must be computed on real-time since they are the input variables for the ISTTOK control position algorithms.

The procedures described in last sections allowed for the cleaning of the signals and for the compensation of the effect of the external fluxes in the measurements. In this section it is described the method for obtaining a vertical and horizontal centroid position in ISTTOK using the processed signals described in the past section. The plasma centroid position is a geometrical center for the current distribution. In [77] and [78] the current centroid is evaluated by substituting the plasma with a small number of arbitrary filaments in arbitrary fixed positions since the reconstruction is not sensitive to these parameters. These filaments are used to approximate the effect of the plasma current distribution on the probes magnetic measurements; hence each of them is assumed to carry a certain amount of current. It should be noted that the individual filamentary current values obtained with this approach possess no physical meaning, while the total current, and the centroid position (r_0, z_0) correspond to the actual current and position of the centroid.

The following work reconstructs a multi-filament model using the corrected magnetic measurements as input. This approach follows the guideline described in [4, Chapter 3]. The method is based on the fact that an optimal solution based on toroidal harmonics is typically close to the MHD equilibrium calculation for the centroid position [4, Chapter 3], MHD equations are not possible to solve by analytical method while numerical approaches are very demanding from a computational point of view. ISTTOK does not possess a Grad-Shafranov solver since it has a very limited set of magnetic field and flux



Figure 4.16.: Fig. 4.16a: ISTTOK Poloidal Cross Section with depiction of the radial and poloidal positions of the selected filaments for the plasma modelling and the magnetic probes. Fig. 4.16b: Comparison between magnetic probes measurements (blue line) and reconstructed values (orange line) during a plasma current positive Flat-top.

probes and due to the cycle time on MARTe, it is necessary to select a method such as a multi-filament model for a reliable centroid reconstruction. The first step consists in the generation of matrixes that are used to estimate the filamentary currents on real-time. The setup of the current filaments was designed by setting the number of filaments and their distance from the centre of the chamber. The values of the currents flowing in each filament were determined by inverting a discretized version of the Biot Savart's equation: $d\vec{B} = \frac{\mu_0}{4\pi} \frac{Id\vec{l} \times \hat{r}}{r^2}$. The numerical inversion is done by computing the pseudo-inverse matrix through Singular Value Decomposition (SVD), resulting in $i_{p,f} = M_{fp}^\dagger f_p$ where f_p is the magnetic probes measurements data vector, $i_{p,f}$ are the filamentary currents best fitting the measurements and M_{fp}^\dagger is the pseudoinverse of the fixed matrix whose ij -element gives the contribution to the measurement i of a unitary current in the filament j . The definitive geometry for ISTTOK has 12 degrees of freedom, as there are 12 static filaments at the distance of 5.5 cm from the centre of the chamber. Fig. 4.16a shows the geometry which was chosen after empiric analysis of the measurements optimization and comparison of the plasma current with the sum of the filaments.

Afterwards it is possible to evaluate the results by comparing the magnetic measurements with the ones obtained using the filamentary currents, as in Fig. 4.16b; another estimation of the results is the total current in the filaments, which is approximately equal to the total current calculated by the sum from the magnetic probes measurements (Ampere's Law) as shown in Fig. 4.17 . Finally, is possible to reconstruct the position of the current centroid with a weighted average of the 12 filaments currents as in eqs. 4.4 where μ is the respective filament number.

$$r_0 = \sqrt{\frac{\sum_{k=1}^{\mu} i_{p,f_k} r_{p,f_k}^2}{\sum_{k=1}^{\mu} i_{p,f_k}}} \quad (4.4a)$$

$$z_0 = \frac{\sum_{k=1}^{\mu} i_{p,f_k} z_{p,f_k}}{\sum_{k=1}^{\mu} i_{p,f_k}} \quad (4.4b)$$

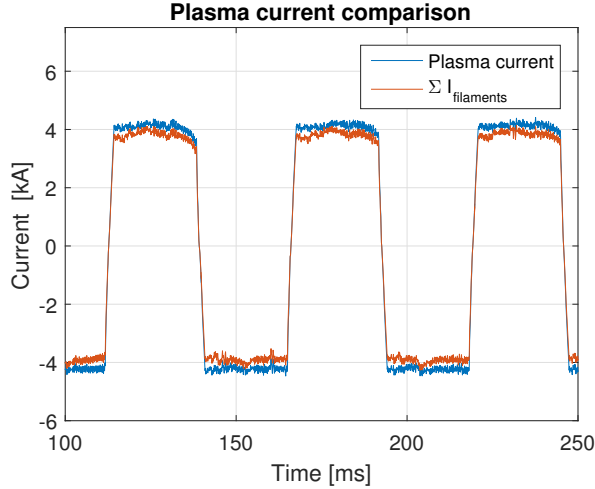


Figure 4.17.: Comparison between the plasma current signal computed with Ampere's law and with the filamentary currents sum.

4.7 REAL-TIME MARTE IMPLEMENTATIONS FOR THE PLASMA POSITION RECONSTRUCTION

Real-Time control in ISTTOK relies on the execution of Generic Application Modules (GAM) executed on MARTe [14]. Algorithms for the subtraction of the magnetic contributions of the PF coils from the magnetic probes signals and for the reconstruction of the current centroid position were implemented in C++ language in an specific ISTTOK GAM .

4.7.1 *Poloidal magnetic external contributions subtraction*

Figure 4.18 compares the time response in one of the magnetic probes to the one reconstructed by the state-space models. During this plasma-less discharge positive and negative current step functions waveforms were applied at different starting times on the PF coils. In figure 4.19 are shown the signals related to the external fluxes subtraction on real-time from a magnetic probe signal during a plasma current flat-top.



Figure 4.18.: Real-Time reconstruction of the external fluxes contribution to the magnetic probes, this plot corresponds to the time trace of the magnetic probe # 3.



Figure 4.19.: Real-Time reconstruction during a plasma flat-top of the external fluxes and its subtraction from the magnetic probe signal.

4.7.2 Plasma current and centroid position reconstruction

In addition to the centroid position, the plasma current is also estimated in ISTTOK from the magnetic probes measurements and programmed on top of MARTE as a discretization of Ampere's law (see eqs. 4.5)

$$\oint_S B \cdot dl = \mu_0 I_{plasma} \quad , \quad (4.5a)$$

$$\frac{2\pi r_{probe}}{N} \sum_{N=1}^{N=12} B_{probes_i} = \mu_0 I_{plasma} \quad . \quad (4.5b)$$

Figure 4.20 depicts a comparison between the plasma current contribution to the magnetic Probe # 1 and the reconstruction of it through the relation $f_p = M_{fp} i_{p,f}$. Figure 4.21 shows the horizontal and

vertical positions and plasma current waveforms calculated on real-time during an AC discharge. Due to the actual controller settings in the tokamak the radial position takes more time to reach the set point than the vertical position whose response is faster. Currently ISTTOK current centroid position reconstruction on real-time is performed based on the multi-filamentary model described on the previous section.

In figure 4.21 is possible to compare plasma current and position from two discharges. In the first one the control signals are based on a centroid position reconstructed by Langmuir probes and in the second discharge the centroid position is computed by the multi-filament model using magnetic probes. It is possible to observe successful inversions of plasma current when the centroid is computed by the multi-filament model in comparison with the absence of plasma current inversions when computing the centroid using the Langmuir probe signals. The plasma current inversion success percentage using algorithm reconstruction assisted by Langmuir probes in ISTTOK is $\sim 80\%$ and assisted by magnetic probes is $\sim 99.8\%$.



Figure 4.20.: Comparison of the magnetic probe # 1 signal without the contribution of the external fluxes and its real-Time SVD reconstruction over the course of an AC Plasma discharge

During the realization of the work corresponding to this chapter a comprehensive analysis and processing of the ISTTOK magnetic diagnostics was done in order to obtain a reliable reconstruction of the centroid position. With the presented corrections on the numerically hardware integrated magnetic signals in ISTTOK, it is now possible to reliably control the plasma position while varying key parameters these results are presented in the next chapter.

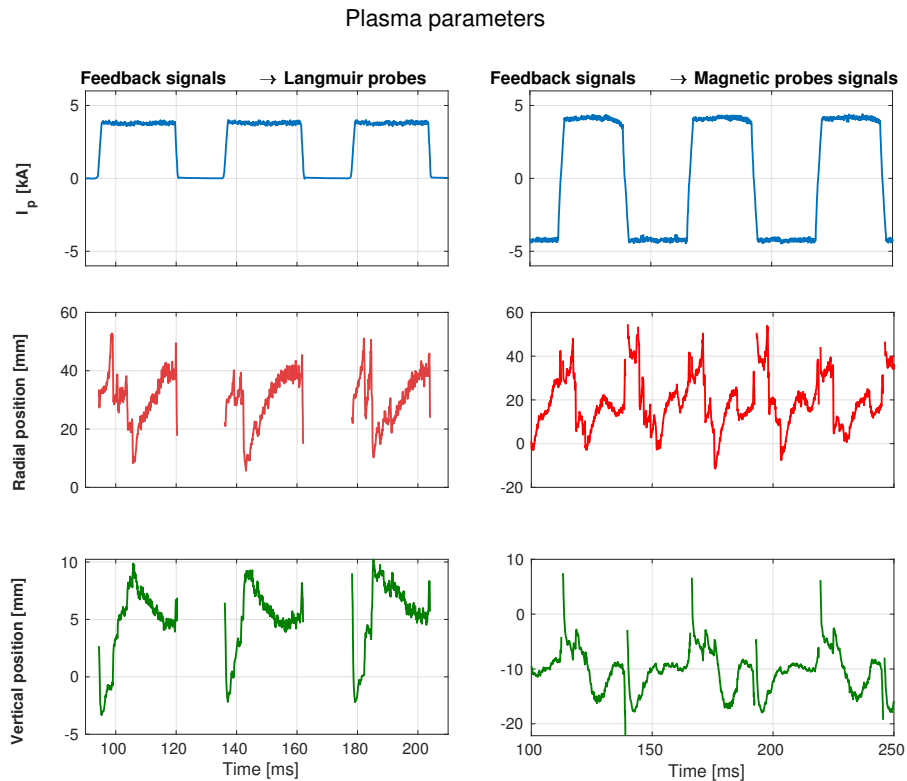


Figure 4.21.: Real-time reconstruction of the vertical and horizontal current centroid position and plasma current assisted by the magnetic probes signal acquisition and post-processing of two plasma discharges. Left column shows the resulting signals when the discharge control feedback is performed using Langmuir probes and right column shows when using Magnetic probes signals. Negative plasma cycles are lost when using Langmuir probes signals.

5

ISTTOK CONTROL IMPLEMENTATIONS AND RESULTS

Using the multi-filament centroid position reconstruction currently available in real-time for all the discharges, is possible to foray into control techniques and its real-time implementation. This chapter describes the latest implementations in ISTTOK's MARTe framework followed by the presentation of the obtained results for control of the vertical and radial current centroid position.

5.1 IMPLEMENTATION OF THE GENERAL APPLICATION MODULES

As mentioned in previous sections, ISTTOK operates on top of the MARTe framework who in turn is basically constructed by a set of General Application Modules (GAM) as described in chapter 2. The control of the plasma current centroid position is achieved by means of several GAMs working altogether, figure 5.1 depicts a scheme of how the control loop works. It starts by acquiring the signals from the magnetic probes and processing them in the "Magnetics" GAM where the radial and vertical centroid position are computed for every MARTe cycle. The "Controller" GAM selects the controller to be used for the centroid position based on the retrieved data from a GUI "Discharge Configurator" the tokamak operator has already configured before the discharge starts. Depending on the controller selection there is a "PID" GAM and a "LQR" GAM , based on the control algorithms studied in Chapter 2.4. After the "PID" GAM or the "LQR" GAM computed the required inputs of the system these values are sent back to the "Controller" GAM which then sends them as command signals to the power supplies of the PF coils.

Since ISTTOK is an AC tokamak during the transition from negative to positive, or opposite, plasma current there is no reconstruction of the centroid position, then a pre-programmed configuration of the PF coils currents acts during this transition of $\approx 1ms$, which means there is a constant switching from automatic to manual control in between plasma cycles, the switching process between controllers produces jumps at the plant inputs, this is known as the bumpless transfer problem [79, Chapter 8]. To remove the jump, the controller output should be made as close as possible to the output during manual mode. Then the jump at the instant of switching will be minimized [80].

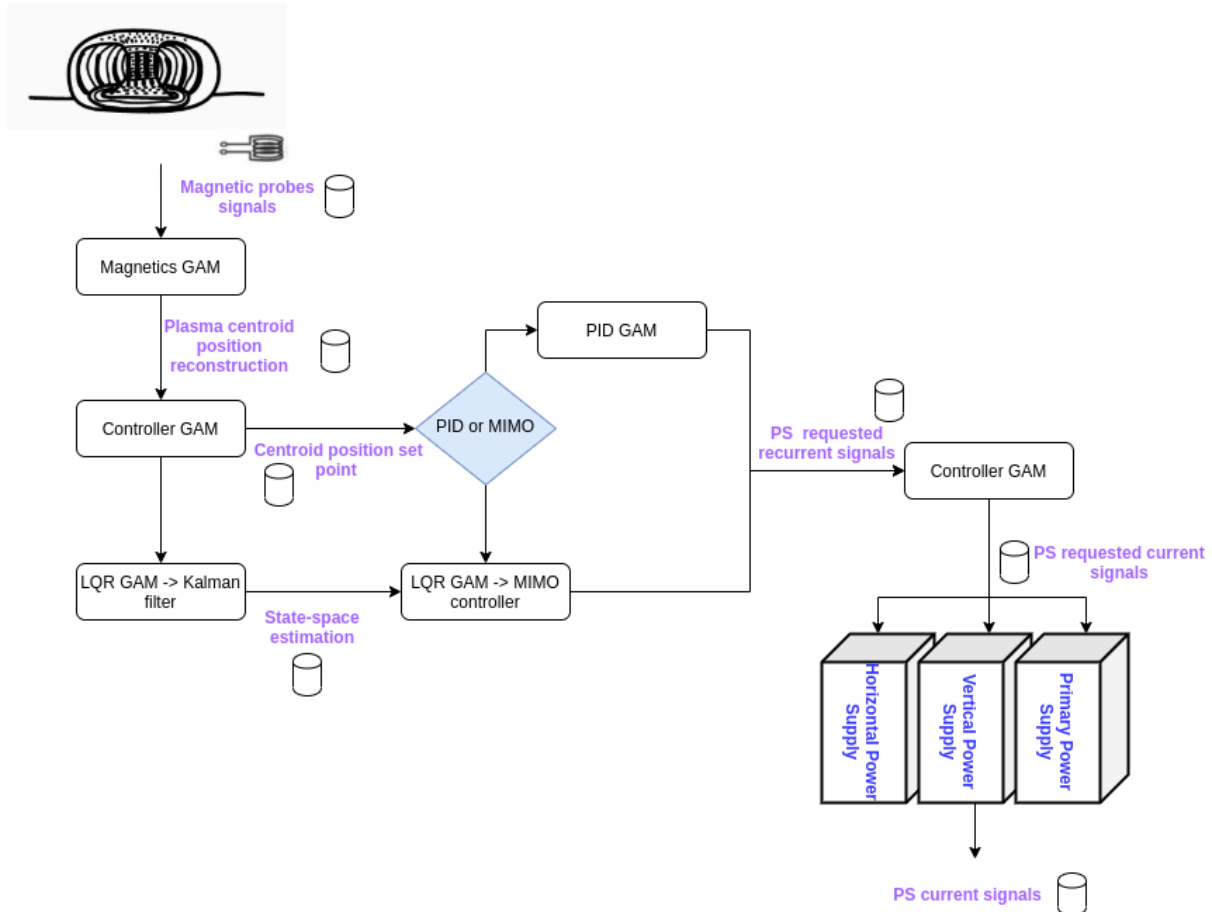


Figure 5.1.: ISTTOK MARTe overall control position scheme.

5.1.1 PID control implementation

Early tokamaks used sets of poloidal field coils symmetrically placed with respect to the tokamak equatorial plane to guarantee mutually independent vertical and horizontal movement of the plasma [4, Chapter 1]. For many years, ISTTOK control relied on the principle that due to Lorentz force law, the control strategy could simply be driven by the principle that an external vertical field generates an horizontal force and a horizontal external field generates a vertical force, having thus two separate SISO controllers for the vertical and radial centroid position. The "PID" GAM is responsible for this function, it has two PID controllers, concept deeply addressed in section 2.4.2, with pre-configuration gains, in addition they have a anti-windup¹ and correction for bumpless transfer by adjusting the integral action when the saturation limits are reached and when the transition from manual to automatic control takes place since this events cause an uncontrolled increment in the integral term [81, Chapter 3], [80].

¹ The saturation of actuators or major set point changes are some of the most frequent nonlinearities in control applications and they can cause instabilities in the system, the undesired effect of this events is called windup and typically it produces undesired overshoots resulting from overreaction in the integrator of a PID controller [79, Chapter 1].

The PID equations are digitally implemented in the "PID" GAM as [81, Chapter 1]:

$$u[k] = K_p e[k] + K_i T_s \sum_{i=1}^k e[i] + \frac{K_d}{T_s} (e[k] - e[k-1]) \quad (5.1)$$

where $u[k]$ is the controlled output signal, for ISTTOK it corresponds to the vertical and horizontal PF coils currents, K_p , K_d and K_i are the PID gains and $e[k]$ is error variable which in this case is the vertical or horizontal plasma centroid position minus a given set point programmed by the operator in the "Discharge configurator". Since no theoretical decoupled model or SISO dynamics are established in ISTTOK the PID gains were selected empirically based in the performance of the controller with different selection of gains in several ISTTOK discharges.

5.1.2 Data-driven state-space model retrieving

Data-driven dynamical systems is a rapidly evolving field, data are abundant, while physical laws or governing equations remain elusive even in classical fields, such as optics and turbulence, where governing equations do exist, researchers are increasingly turning toward data-driven analysis [82, Chapter 7].

Early efforts in finding a theoretical model for ISTTOK magnetic control were performed during the last years. Since ISTTOK PF coils are not axisymmetric a working theoretical model was never successfully retrieved. This fact made necessary to find a novel form to implement a model-based magnetic control on ISTTOK real-time MARTe platform. Through the *System Identification Toolbox* from MATLAB, whose background concepts were explained in chapter 2.4.5, state-space models were retrieved. These models have as inputs the PF vertical and horizontal currents and as outputs the vertical and radial plasma current centroid position, having thus 2×2 MIMO systems. During this process data from several discharges were used in order to obtain sufficiently accurate models.

When joining data sets of signals from positive and negative plasma current discharges the models started to not be consistent showing since early stages that the tokamak needed to be modeled separately: one state-space model for discharges where $I_p > 0$ and another for discharges where $I_p < 0$. This matter probably originates from the fact that a tokamak is not completely axisymmetric in reality, and particularly for ISTTOK, it happens to have a very non-axisymmetric PF coils which can translate as a different overall topology of the poloidal magnetic field in the tokamak for $I_p < 0$ and the $I_p < -0$ case. Figure 5.2 and figure 5.3 show the comparison between the data-base centroid position signal and its reconstruction using the estimated state-space models. These are validation plots, which means the signals from the reconstruction of the centroid position were not used as modeling data, differences in the transients of the signals might be originated from the differences in initial states between systems.

Since a tokamak is not a linear system, the modeling process was done using data sets where the centroid position was located in a certain region of values in order to approximate the estimated model



(a) Comparison between the identified model response and the real-time centroid position reconstruction. Shot #48559

(b) Comparison between the identified model response and the real-time centroid position reconstruction. Shot #48541

Figure 5.2.: Model response for two different $I_p \approx 4 kA$ discharges.



(a) Comparison between the identified model response and the real-time centroid position reconstruction. Shot #48338

(b) Comparison between the identified model response and the real-time centroid position reconstruction. Shot #48345

Figure 5.3.: Model response for two $I_p \approx -4 kA$ discharges.

to an equilibrium region where a linear model approximation is valid. A local linearized model is typically evaluated in a set of operating points that capture the key modes of operation. Using classical PID controllers or optimal design methods like LQR are synthesized for the system in these points ensuring that some relevant performance specifications are met in the vicinity of the operating point in question [83]. The optimal number of states computationally retrieved was 10. The input and output vectors for ISTTOK models are defined as:

$$\begin{aligned} u^T &= [R, z] \quad , \\ y^T &= [I_{vert}, I_{hor}] \quad . \end{aligned} \quad (5.2)$$

5.1.3 Kalman filter implementation

After retrieving the state-space models for the plasma centroid position, the next goal is to implement a MIMO controller based on them. In order to reconstruct the states vector x two Kalman filters were implemented, one for plasma current positive model and another for the negative model. The Kalman filter matrices were obtained based on noise vectors from ISTTOK real data calculating the covariance matrices from the signal vectors [84]. Figure 5.5 and 5.4 correspond to the real-time Kalman filter reconstruction of the vertical and radial plasma centroid position and its comparison with the multi-filament reconstructed position computed at the "Magnetics" GAM.

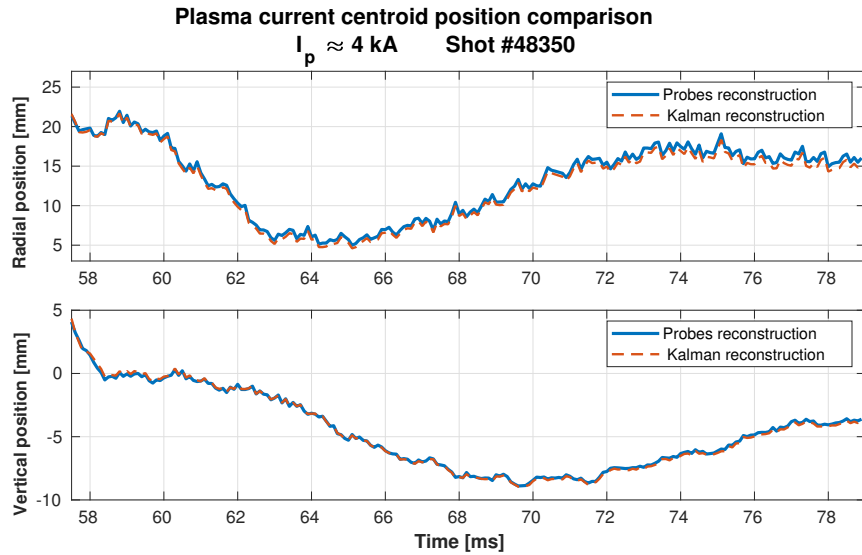


Figure 5.4.: Comparison of the real-time Kalman filter retrieved centroid position and the multi-filament reconstruction time trace for $I_p > 0$.

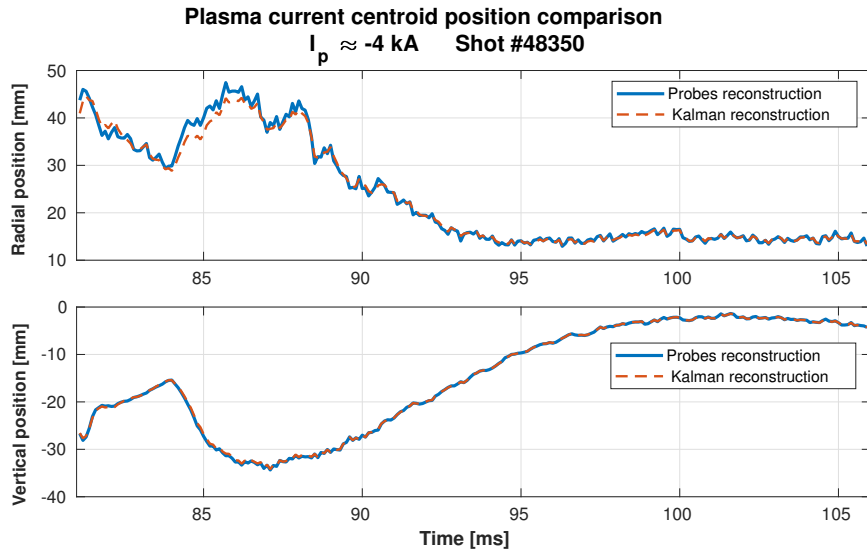


Figure 5.5.: Comparison of the real-time Kalman filter retrieved centroid position and the multi-filament reconstruction time trace for $I_p < 0$

5.1.4 Multiple-Input Multiple-Output control implementation

The full-state estimate from the Kalman filter is generally used in conjunction with the full-state feedback control law from LQR, resulting in optimal sensor-based feedback. Combining the LQR full-state feedback with the Kalman fitler full-state estimator results in the linear-quadratic Gaussian (LQG) controller [82, Chapter 8]. Under this principle the real-time reconstructed states are multiplied by the control LQR gain K in order to take the the vertical and radial plasma centroid position to a certain set point, this process is computed in the "LQR" GAM. The weight matrices for the discrete LQR controller were empirical tuned in order to have a balance between a fast response and a not so energetically demanding input, several algorithms for a non-empirical calculation of the LQR matrices exist some of them propose a tuning based on experimental data with a gain matrix that can be iterative updated [85, Chapter 9], [86].

Pole-zeros maps

Given the transfer function $H(s) \frac{b(s)}{a(s)}$ the value of s such that $b(s) = 0$ are places where $H(s)$ is zero, and the corresponding s locations are called zeros. The concept of pole was introduced in section 2.4.3. A Pole-zeros map is a representation in the complex plain n of the poles and zeros location of a system, either is in open-loop or in closed-loop. Since the data-driven models and its controllers are discrete the pole stability is given in a different form as in the continues time case, figure 5.6 shows the stable location of discrete poles($|\lambda| = 1$), the locations of the zeros have no role in determining the system stability.



Figure 5.6.: The matrix exponential defines a conformal map on the complex plane, mapping stable eigenvalues in the left half plane for continuous systems into eigenvalues inside the unit circle for discrete [82, Chapter 8].

Pole-zero cancellation of stable poles will not cause any serious problem in the overall system except if the canceled pole is unstable. If a system has at least one pole or zero outside the unitary circumference the system is called Non-minimum phase ([42, Chapter 6], [38, Chapter 2]). Non-minimum phase systems can show an inverse response or undershoot, which is an initial response in the opposite direction from the steady states, figure 5.7 shows the time trace of the response to a unit step of a non-minimum phase system. In these plots is possible to observe several important details which allow to understand more the dynamics of the systems.

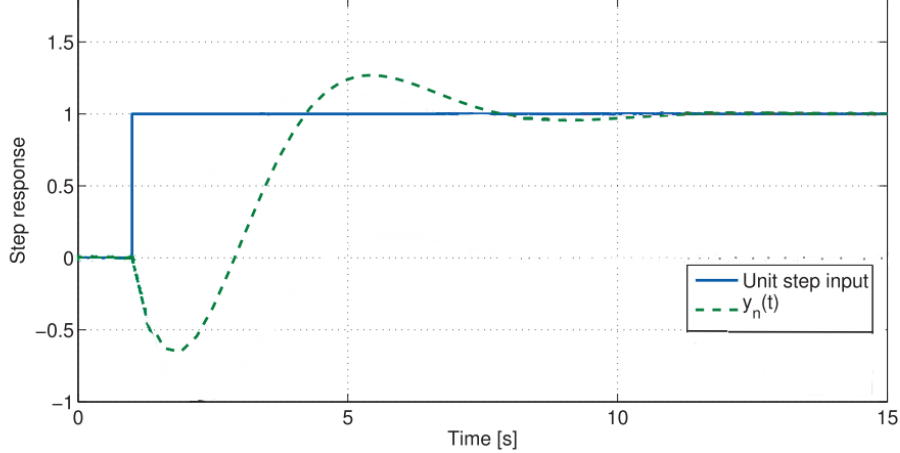


Figure 5.7.: Response to a unit step input from a non-minimum phase system [87].

Figures 5.8 and 5.9 correspond to the pole-zero maps for the state-space model where $I_p \approx 4 \text{ kA}$ in closed loop and figures 5.10 and 5.11 to the same system in open-loop. Figures 5.12 and 5.13 correspond to the pole-zero maps for the state-space model where $I_p \approx -4 \text{ kA}$ and figures 5.14 and 5.15 to the same system in open-loop. It should be noticed that since the data-driven models are 2×2 MIMO systems each case is formed by 4 pole-zero maps.

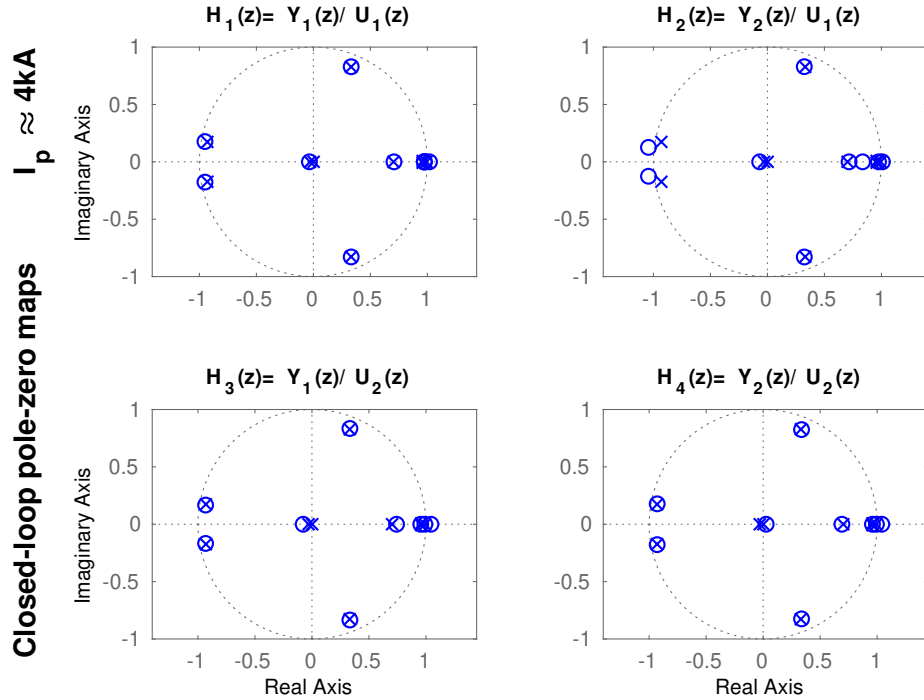


Figure 5.8.: Pole-zero maps in closed loop for the model when $I_p \approx 4kA$. Superposition of poles and zeros can be seen in the four transfer functions.

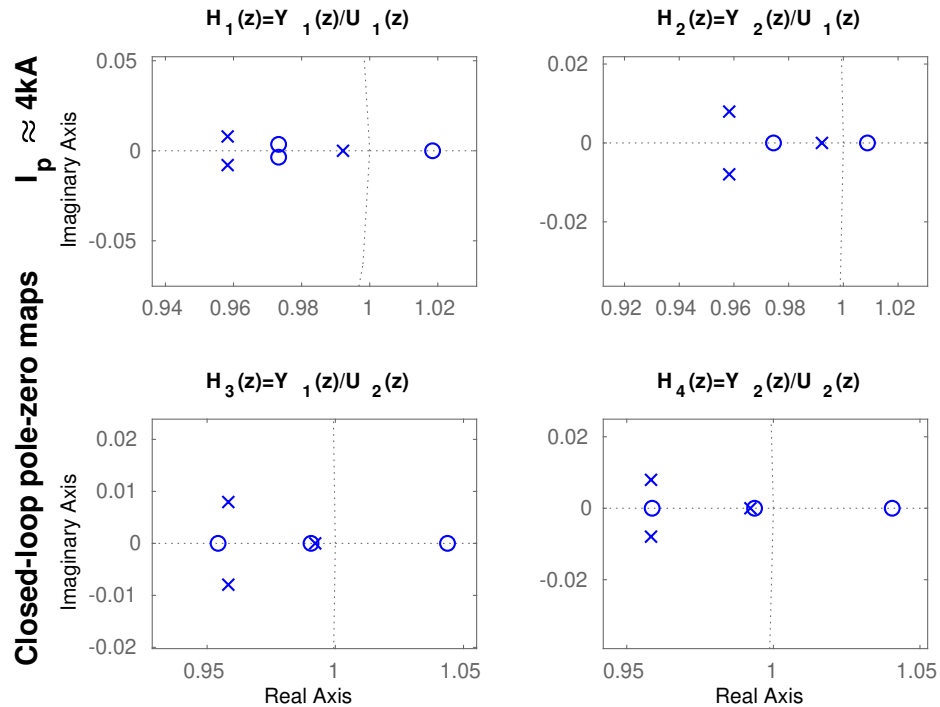


Figure 5.9.: Zoom to the stability border of the pole-zero maps in closed loop for the model when $I_p \approx 4kA$.

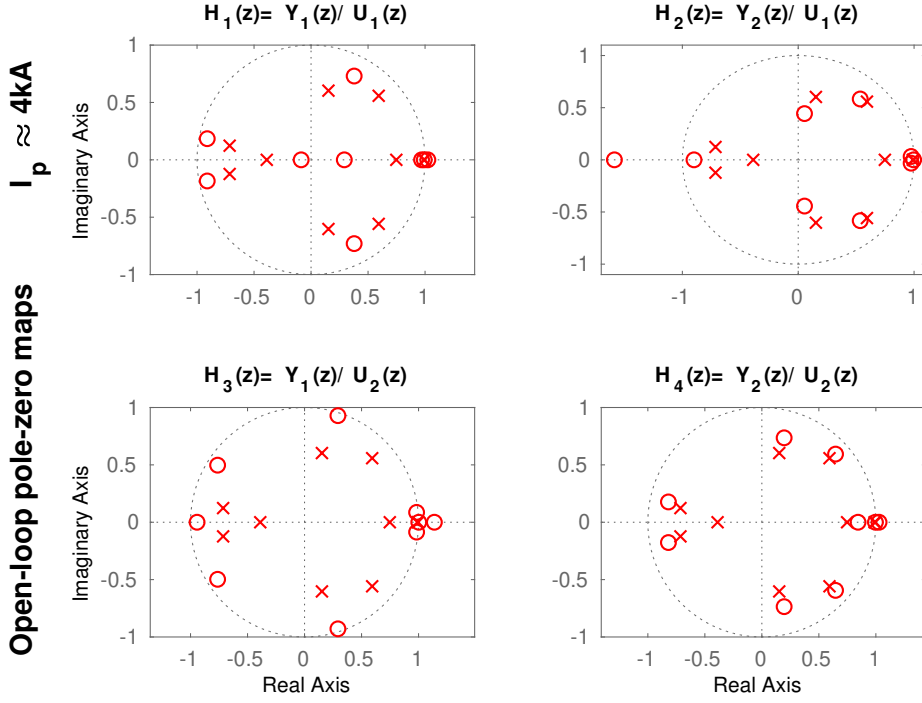


Figure 5.10.: Pole-zero maps in open loop for the model when $I_p \approx 4kA$. Superposition of poles and zeros can be seen in the four transfer functions.



Figure 5.11.: Zoom to the stability border of the pole-zero maps in open loop for the model when $I_p \approx 4kA$.



Figure 5.12.: Pole-zero maps in closed loop for the model when $I_p \approx -4kA$. Superposition of poles and zeros can be seen in the four transfer functions. In the transfer function $H_2(z)$ should be noticed the zero far from the unitary circumference.

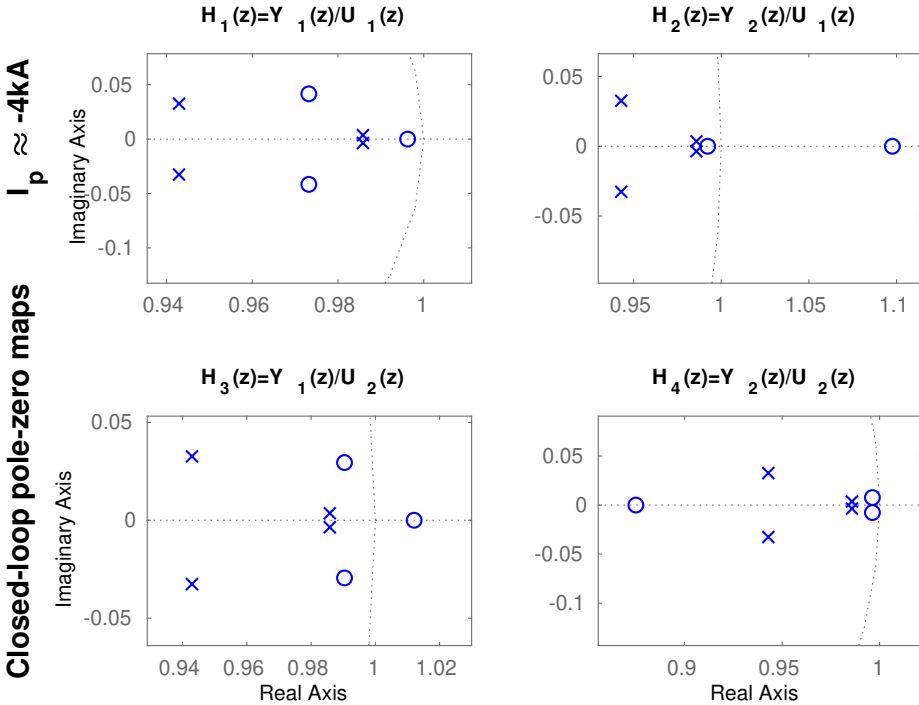


Figure 5.13.: Zoom to the stability border of the pole-zero maps in closed loop for the model when $I_p \approx -4kA$.



Figure 5.14.: Pole-zero maps in open loop for the model when $I_p \approx -4kA$. Superposition of poles and zeros can be seen in the four transfer functions. In the transfer function $H_2(z)$ should be noticed the zero far from the unitary circumference.



Figure 5.15.: Zoom to the stability border of the pole-zero maps in open loop for the model when $I_p \approx -4kA$.

- Open-loop and closed-loop models for $I_p \approx -4kA$ have a zero far from the unitary circumference in the transfer function $H_2(z)$ map which links the vertical centroid position z and the vertical PF coils current I_{vert} , this might generate an initial inverse response in the vertical centroid position.
- The open-loop and closed-loop systems for both models , i.e. $I_p \approx 4kA$ and $I_p \approx -4kA$, have pole-zero cancellation inside the unitary circle.
- The model for $I_p \approx 4kA$ in open-loop has one unstable pole for the 4 transfer functions, see figure 5.15, this shows a significant characteristic that differentiates both models, for negative and positive plasma current.

5.2 PLASMA CURRENT CENTROID POSITION CONTROL RESULTS

This section presents the latest results from the real-time implementation of control algorithms in ISTTOK. The position set points are pre-programmed by the operator in the "Discharge configurator", in the plots presented in this section the discharges are referred as *Shot#* followed by the ISTTOK's database discharge number.

In the following plots vertical and horizontal plasma centroid position are compared when they are controlled by a set of 2 PID and by a LQR MIMO controller for different pre-programmed set points. Also the inputs response, vertical and horizontal PF coils currents, are shown and compared.

The discharges with LQR MIMO control start with PID controllers and then switch to MIMO LQR control at $t \sim 1 ms$ for positive plasmas and $t \sim 3.5 s$ for negative ones. Since it is not mathematically possible to determine the initial conditions of the states they must be steered to the MIMO controller region of attraction, this is achieved by controlling the centroid position with the PID's at the beginning of the discharge while the Kalman filter reconstructs the state vector. Switching between two controllers in parallel yields a control substitution which causes bumps in the response, there is available literature for applications of the bumpless transfer scheme in order to smooth phasing-in of a new controller to supplement or replace an existing control at the plant as described in [83].

Figure 5.17 and 5.16 show the time traces of the vertical and horizontal plasma centroid position for two different scenarios. Figure 5.16 shows the plots corresponding to a plasma discharge where $I_p \approx -4 kA$, the green vertical line marks the switching point from PID control to MIMO LQR. The vertical position time trace shows a non-minimum phase system behavior for the MIMO LQR control which is consistent with the pole-zero maps from last section, but this behavior does not show for the PID case. This might be originated during the data-driven identification procedure as a numerical artifact to model a delay. Figure 5.17 corresponds to a plasma discharge where $I_p \approx 4 kA$, since the PID controlled part of the discharge is very short, the switching point is not signalized. The position set points are black dashed lines in both figures.



Figure 5.16.: Horizontal and vertical plasma centroid position during $I_p \approx 4\text{kA}$ flat-tops, blue time trace corresponds to a PID feedback control and orange time trace to a LQR MIMO feedback control, the dashed black line shows the programmed set point. The green vertical line marks the time when the discharge Shot#48324 switches from PID to MIMO LQR control.

Figure 5.19 and 5.18 correspond to the vertical and horizontal PF coil currents plots. For both cases, $I_p \approx 4\text{kA}$ and $I_p \approx -4\text{kA}$, a noticeable smaller current request from the vertical and horizontal PF coils power supplies can be appreciate for the discharges controlled with the LQR MIMO algorithm in comparison with the ones controlled via the PID's, which implies less consume of energy in the system.

Table 5.2 summarizes the root-mean squared error (RMSE) for several plasma discharges for positive and negative plasma current and with different set points. For every plasma position set point a PID controlled and a MIMO LQR controlled discharge was performed. The time traces for all discharges presented in the table can be found in appendix A, as well as the plots of the corresponding vertical and horizontal PF coils requested currents. All signals discharges are available in the ISTTOK data base and the PID and MIMO LQR controllers are permanently available options for the tokamak operators in the "Discharge configurator" as well as the selection of switching times between controllers separately for positive and negative plasma discharges.

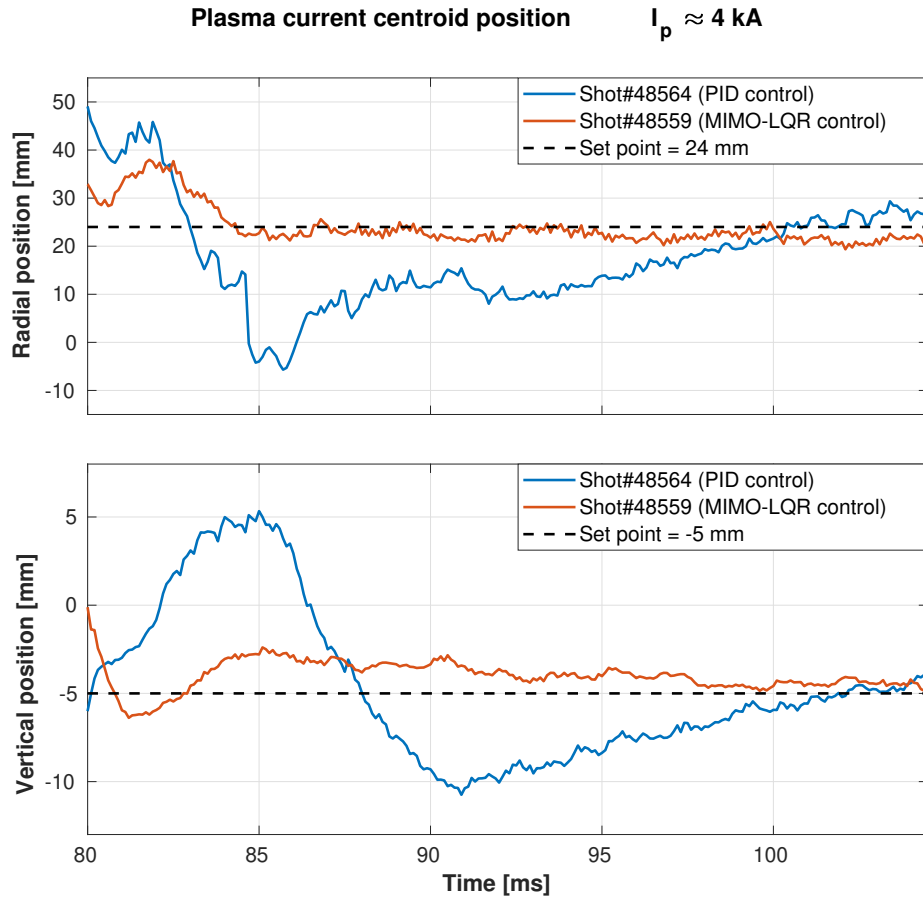


Figure 5.17.: Horizontal and vertical plasma centroid position during $I_p \approx 4 \text{ kA}$ flat-tops, blue time trace corresponds to a PID feedback control and orange time trace to a LQR MIMO feedback control, the dashed black line shows the programmed set point.

Control	Shot #	RMSE (R,z) mm	Set point (R,z) mm	I_p
PID	48564	(13.73, 4.4102)	(24, -5)	$\approx 4 \text{ kA}$
MIMO LQR	48559	(4.2252, 1.4215)		$\approx 4 \text{ kA}$
PID	48563	(13.6717, 4.1652)	(24, -4)	$\approx 4 \text{ kA}$
MIMO LQR	48561	(8.1047, 3.2752)		$\approx 4 \text{ kA}$
PID	48556	(12.0315, 3.3217)	(32, -5)	$\approx 4 \text{ kA}$
MIMO LQR	48555	(4.2618, 2.4698)		$\approx 4 \text{ kA}$
PID	48551	(13.9998, 3.3431)	(27, -5)	$\approx 4 \text{ kA}$
MIMO LQR	48554	(5.9830, 2.0062)		$\approx 4 \text{ kA}$
PID	48515	(6.0178, 2.6123)	(30, -5)	$\approx 4 \text{ kA}$
MIMO LQR	48541	(5.8372, 1.7664)		$\approx 4 \text{ kA}$
PID	48544	(4.8745, 2.5167)	(32, -4)	$\approx 4 \text{ kA}$

MIMO LQR	48542	(4.4346, 3.6573)		$\approx 4kA$
PID	48546	(11.4560, 3.4765)	(27, -7)	$\approx 4kA$
MIMO LQR	48548	(7.6745, 4.1569)		$\approx 4kA$
PID	48341	(12.0959, 5.7652)		$\approx -4kA$
MIMO LQR	48324	(15.4768, 14.3436)	(11, -5)	$\approx -4kA$
PID	48340	(11.7701, 5.9599)		$\approx -4kA$
MIMO LQR	48338	(11.5260, 12.6226)	(11.2, -5.5)	$\approx -4kA$
PID	48343	(15.7675, 5.7453)		$\approx -4kA$
MIMO LQR	48342	(14.5168, 14.4329)		$\approx -4kA$
PID	48346	(12.4228, 6.1541)	(12.2, -5.3)	$\approx -4kA$
MIMO LQR	48345	(9.7513, 13.0338)		$\approx -4kA$
PID	48349	(19.3397, 5.5406)	(11.5, -5.6)	$\approx -4kA$
MIMO LQR	48348	(9.1727, 13.1505)		$\approx -4kA$
PID	48352	(15.2181, 6.5395)	(10.8, -4.7)	$\approx -4kA$
MIMO LQR	48354	(14.6405, 13.7307)		$\approx -4kA$
PID	48351	(13.4078, 5.8769)	(13.2, -5.6)	$\approx -4kA$
MIMO LQR	48350	(13.9320, 14.4940)		$\approx -4kA$

Table 5.1.: Centroid position RMSE comparison between PID and MIMO-LQR controlled discharges for different set points and plasma current scenarios.

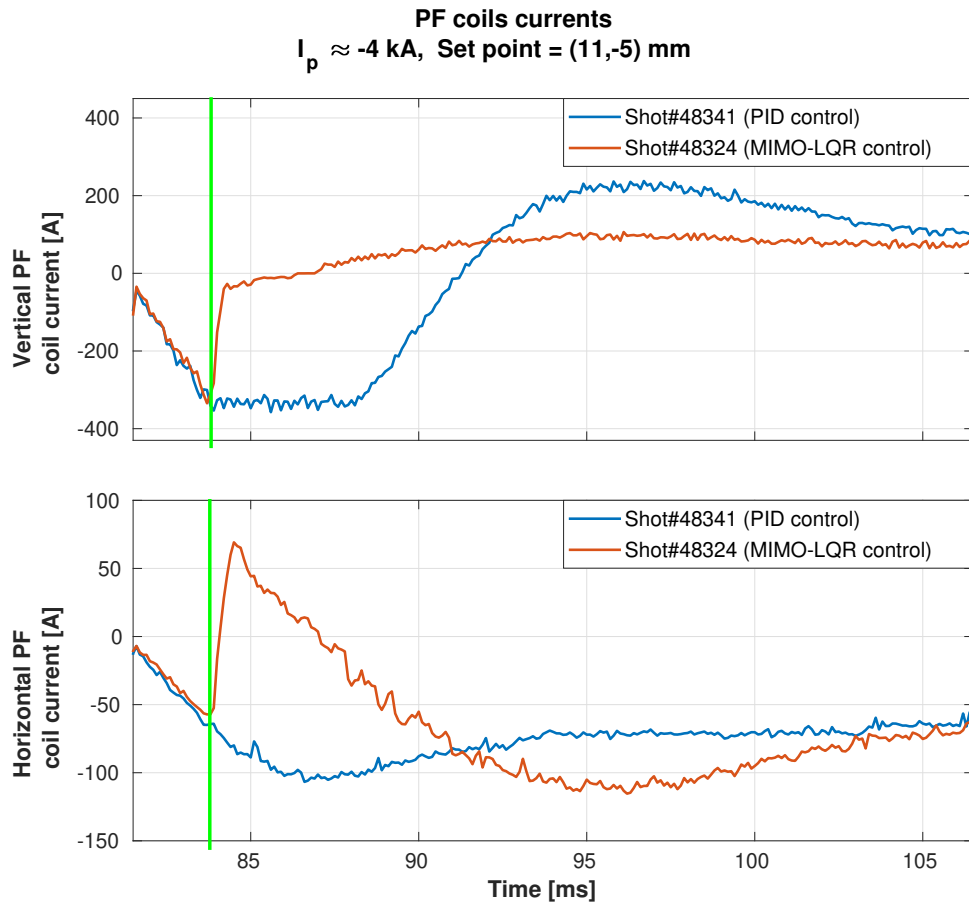


Figure 5.18.: Vertical and Horizontal PF coils currents during $I_p \approx -4 \text{ kA}$ flat-tops, blue time trace corresponds to a PID feedback control and orange time trace to a LQR MIMO feedback control. The green vertical line marks the time when the discharge Shot#48324 switches the control from PID to MIMO LQR.

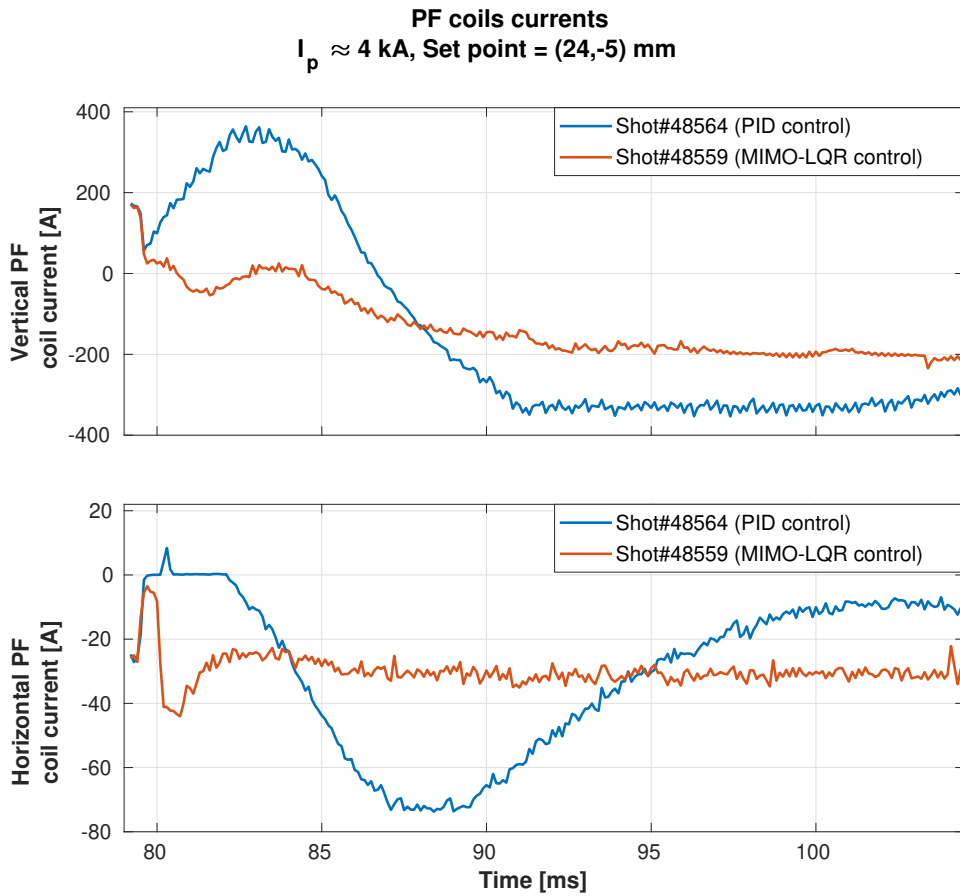


Figure 5.19.: Vertical and Horizontal PF coils currents during $I_p \approx 4\text{kA}$ flat-tops, blue time trace corresponds to a PID feedback control and orange time trace to a LQR MIMO feedback control.

6

CONCLUSIONS

6.1 GENERAL CONCLUSION

6.2 JT60-SA

6.3 ISTTOK

BIBLIOGRAPHY

- [1] Jeffrey P. Freidberg. *Plasma physics and fusion energy*. Cambridge University Press, 2007.
- [2] K. Miyamoto. *Fundamentals of Plasma Physics and Controlled Fusion*. Group, Taylor and Francis, 3 edition, 2011.
- [3] Hartmut Zohm. *Magnetohydrodynamic Stability of Tokamaks*. Wiley, 2015.
- [4] A. Pironti and M. Ariola. *Magnetic Control of Tokamak Plasma*. Springer, 2nd edition, 2016.
- [5] J B Lister, Y Martin, Centre De Recherches, Ecole Polytechnique, Fédérale De Lausanne, T Fukuda, R Yoshino, Jaeri Fusion, V Mertens, and Max-planck Institut Plasmaphysik. The Control of Modern Tokamaks. In *International Conference on Accelerator and Large Experimental Physics Control Systems*, Trieste, Italy, 1999.
- [6] Andrej A. Kavin Valerij A. Belyakov. *Fundamentals of Magnetic Thermonuclear Reactor Design*. Elsevier, 2018.
- [7] F. Janky, M. Hron, J. Havlicek, M. Varavin, F. Zacek, J. Seidl, and R. Panek. Plasma density control in real-time on the COMPASS tokamak. *Fusion Engineering and Design*, 96-97:637–640, 2015.
- [8] J. R. Ferron, A. Kellman, E. McKee, T. Osborne, P. Petrach, T. S. Taylor, J. Wight, and E. Lazarus. An advanced plasma control system for the dIII-d tokamak. In *[Proceedings] The 14th IEEE/NPSS Symposium Fusion Engineering*, pages 761–764 vol.2, Sep. 1991.
- [9] B. G. Penaflor, J. R. Ferron, A. W. Hyatt, M. L. Walker, R. D. Johnson, D. A. Piglowski, E. Kolemen, A. S. Welander, and M. J. Lanctot. Latest advancements in DIII-D Plasma Control software and hardware. *2013 IEEE 25th Symposium on Fusion Engineering, SOFE 2013*, pages 1–4, 2013.
- [10] M. Margo, B. Penaflor, H. Shen, J. Ferron, D. Piglowski, P. Nguyen, J. Rauch, M. Clement, A. Battey, and C. Rea. Current State of DIII-D Plasma Control System. *Fusion Engineering and Design*, 150(October 2019), 2020.
- [11] Mellanox Technologies. Introduction to InfiniBand. Technical report, 2003.
- [12] J. I. Paley, S. Coda, B. Duval, F. Felici, and J. M. Moret. Architecture and commissioning of the TCV distributed feedback control system. *Conference Record - 2010 17th IEEE-NPSS Real Time Conference, RT10*, pages 1–6, 2010.

Bibliography

- [13] H. Anand, C. Galperti, S. Coda, B. P. Duval, F. Felici, T. Blanken, E. Maljaars, J. M. Moret, O. Sauter, T. P. Goodman, and D. Kim. Distributed digital real-time control system for the TCV tokamak and its applications. *Nuclear Fusion*, 57(5), 2017.
- [14] A. C. Neto, F. Sartori, F. Piccolo, R. Vitelli, G. De Tommasi, L. Zabeo, A. Barbalace, H. Fernandes, D. F. Valcarcel, and A. J. N. Batista. Marte: A multiplatform real-time framework. *IEEE Transactions on Nuclear Science*, 57(2):479–486, April 2010.
- [15] G. De Tommasi, F. Piccolo, A. Pironti, and F. Sartori. A flexible software for real-time control in nuclear fusion experiments. *Control Engineering Practice*, 14(11):1387–1393, 2006.
- [16] André C. Neto, Diogo Alves, Luca Boncagni, Pedro J. Carvalho, Daniel F. Valcárcel, Antonio Barbalace, Gianmaria De Tommasi, Horácio Fernandes, Filippo Sartori, Enzo Vitale, Riccardo Vitelli, and Luca Zabeo. A survey of recent MARTe based systems. In *IEEE Transactions on Nuclear Science*, volume 58, pages 1482–1489, 2011.
- [17] A Neto, D Alves, B B Carvalho, P J Carvalho, H Fernandes, D F Valc, G De Tommasi, Associazione Euratom-enea create, Via Claudio, P Mccullen, A Stephen, Euratom-ccfe Fusion Association, Culham Science Centre, Abingdon Ox, United Kingdom, R Vitelli, Tor Vergata, Via Politecnico, L Zabeo, and Iter Organisation. Marte Framework : a Middleware for Real-Time Applications Development. In *13th International Conference on Accelerator and Large Experimental Physics Control Systems*, number 11, pages 1277–1280, Grenoble, France, 2011.
- [18] B. Gonçalves, J. Sousa, A. Batista, R. Pereira, M. Correia, A. Neto, B. Carvalho, H. Fernandes, and C. A.F. Varandas. ATCA advanced control and data acquisition systems for fusion experiments. *IEEE Transactions on Nuclear Science*, 57(4 PART 2):2147–2154, 2010.
- [19] A. J.N. Batista, J. Sousa, and C. A.F. Varandas. ATCA digital controller hardware for vertical stabilization of plasmas in tokamaks. *Review of Scientific Instruments*, 77(10):1–4, 2006.
- [20] Ivo S. Carvalho, Paulo Duarte, Horácio Fernandes, Daniel F. Valcárcel, Pedro J. Carvalho, Carlos Silva, André S. Duarte, André Neto, Jorge Sousa, António J.N. Batista, Tiago Hekkert, and Bernardo B. Carvalho. ISTTOK real-time architecture. *Fusion Engineering and Design*, 89(3):195–203, 2014.
- [21] P. J. Carvalho, B. B. Carvalho, A. Neto, R. Coelho, H. Fernandes, J. Sousa, C. Varandas, E. Chávez-Alarcón, and J. J.E. Herrera-Velázquez. Real-time plasma control based on the ISTTOK tomography diagnostic. *Review of Scientific Instruments*, 79(10):1–4, 2008.
- [22] Yash Gupta. *Software Quality Assurance*, volume 6. 1989.
- [23] Andre C. Neto, Filippo Sartori, Riccardo Vitelli, Llorenç Capella, Giuseppe Ferro, Ivan Herrero, and Hector Novella. An agile quality assurance framework for the development of fusion real-time applications. In *2016 IEEE-NPSS Real Time Conference, RT 2016*, 2016.

- [24] I. Neto, A. Herrero. D4 MARTE Project Management Plan. *F4E Internal Document*, (July):1–4, 2018.
- [25] I. Neto, A. Herrero. D4 MARTE Coding Standard. *F4E Internal Document*, (July):1–4, 2018.
- [26] I. Neto, A. Herrero. MARTE Quality Assurance Plan. *F4E Internal Document*, (July):1–4, 2018.
- [27] V. D. Shafranov and V. S. Mukhovatov. Plasma Equilibrium in a Tokamak. *Nuclear Fusion*, 11(6):605–633, 1971.
- [28] L. L. Lao, H. St John, R. D. Stambaugh, A. G. Kellman, and W. Pfeiffer. Reconstruction of current profile parameters and plasma shapes in tokamaks. *Nuclear Fusion*, 25(11):1611–1622, 1985.
- [29] M. Fitzgerald, L. C. Appel, and M. J. Hole. EFIT tokamak equilibria with toroidal flow and anisotropic pressure using the two-temperature guiding-centre plasma. *Nuclear Fusion*, 53(11), 2013.
- [30] D Mueller, D A Gates, J E Menard, J R Ferron, and S A Sabbagh. Real-time Equilibrium Reconstruction and Isoflux Control of Plasma Shape and Position in the National Spherical Torus Experiment (NSTX) by PRINCETON PLASMA PHYSICS LABORATORY. Technical Report August, 2004.
- [31] Chiara Piron, Gabriele Manduchi, Paolo Bettini, Federico Felici, Claudio Finotti, Paolo Franz, Ondrej Kudlacek, Giuseppe Marchiori, Lionello Marrelli, J. M. Moret, Paolo Piovesan, Olivier Sauter, and Cesare Taliercio. Integration of the state observer RAPTOR in the real-time MARTE framework at RFX-mod. *Fusion Engineering and Design*, 123:616–619, 2017.
- [32] F. Felici, O. Sauter, S. Coda, B. P. Duval, T. P. Goodman, J. M. Moret, and J. I. Paley. Real-time physics-model-based simulation of the current density profile in tokamak plasmas. *Nuclear Fusion*, 51(8), 2011.
- [33] Federico Felici, Marco De Baar, and Maarten Steinbuch. A dynamic state observer for real-time reconstruction of the tokamak plasma profile state and disturbances. *Proceedings of the American Control Conference*, pages 4816–4823, 2014.
- [34] D. P. O'Brien, J. J. Ellis, and J. Lingertat. Local expansion method for fast plasma boundary identification in JET. *Nuclear Fusion*, 33(3):467–474, 1993.
- [35] D. MAZON, J. BLUM, C. BOULBE, B. FAUGERAS, M. BARUZZO, A. BOBOC, S. BREMOND, M. BRIX, P. DE VRIES, S. SHARAPOV, L. ZABEO, and JET-EFDA Contributors. Equinox: a Real-Time Equilibrium Code and Its Validation At Jet. (June):327–332, 2010.
- [36] R. Albanese and F. Villone. The linearized CREATE-L plasma response model for the control of current, position and shape in tokamaks. *Nucl. Fus.*, 38(5):723–738, May 1998.
- [37] R. Albanese, G. Calabrograve, M. Mattei, and F. Villone. Plasma response models for current, shape and position control at JET. *Fus. Eng. Des.*, 66–68:715–718, 2003.

Bibliography

- [38] Farid Golnaraghi and Benjamin C Kuo. *Automatic Control Systems*. Pearson, 9nd edition, 2010.
- [39] T. Kailath. *Linear Systems*. Prentice Hall, Englewood Cliffs, 1980.
- [40] Chi-Tsong Chen. *Linear System Theory And Design*. Oxford University Press, 3 edition, 1999.
- [41] Norman Nise. *Control Systems Engineering*. John Wiley & Sons, Inc., 6 edition, 2011.
- [42] Katsuhiko Ogata. *Modern Control Engineering*. Prentice Hall, 5 edition, 2009.
- [43] Sigurd Skogestad and Ian Postlethwaite. 2 edition.
- [44] Peter Hippe and Joachim Deutscher. *Design of Observer-based Compensators*. 2009.
- [45] L. Ljung. *System Identification Theory for User*. 1987.
- [46] T McKelvey. *Identification of State-Space Models from Time and Frequency Data*. PhD thesis, Linkoping University, 1995.
- [47] L. Ljung. *System identification toolbox: User's guide*. MathWorks, 2017.
- [48] William R. Spears. JT-60SA construction status. *IEEE Transactions on Plasma Science*, 2014.
- [49] JT-60SA Team. Research objectives and strategy. Technical report, 2018. <http://www.jt60sa.org/>.
- [50] N Cruz, G. De Tommasi, M Mattei, A Mele, Y Miyata, A Pironti, and T Suzuki. Control-oriented tools for the design and validation of the JT-60SA magnetic control system. *Control Engineering Practice*, 63:81–90, 2017.
- [51] JT-60SA Team. Plant integration document. Technical report, 2017. <https://users.jt60sa.org/?uid=222UJY>.
- [52] R. Albanese, R. Ambrosino, and M. Mattei. CREATE-NL+: A robust control-oriented free boundary dynamic plasma equilibrium solver. *Fus. Eng. Des.*, 96–97:664–667, Oct. 2015.
- [53] Gianmaria De Tommasi, Raffaele Albanese, Giuseppe Ambrosino, Marco Ariola, Massimiliano Mattei, Alfredo Pironti, Filippo Sartori, and Fabio Villone. XSC tools: A software suite for tokamak plasma shape control design and validation. *IEEE Transactions on Plasma Science*, 35(3):709–723, 2007.
- [54] R. Albanese, G. Ambrosino, M. Ariola, A. Cenedese, F. Crisanti, G. De Tommasi, M. Mattei, F. Piccolo, A. Pironti, F. Sartori, and F. Villone. Design, implementation and test of the XSC extreme shape controller in JET. *Fusion Engineering and Design*, 74(1-4):627–632, 2005.
- [55] H. Anand et al. A novel plasma position and shape controller for advanced configuration development on the TCV tokamak. *Nucl. Fus.*, 57(12):126026, 2017.

- [56] E. de la Luna et al. Recent Results on High-Triangularity H-Mode Studies in JET-ILW. In *26th IAEA Fusion Energy Conference*, Kyoto, Japan, October 2016.
- [57] G. Ambrosino et al. Design and Implementation of an Output Regulation Controller for the JET Tokamak. *IEEE Trans. Control Syst. Tech.*, 16(6):1101–1111, Nov. 2008.
- [58] M. Ariola and A. Pironti. The design of the eXtreme Shape Controller for the JET tokamak. *IEEE Control Sys. Mag.*, 25(5):65–75, Oct. 2005.
- [59] H. Urano et al. Y. Miyata. Documents on inputs, outputs of ccs(cauchy condition surface) method. Technical report, 2018.
- [60] H. Urano et al. Y. Miyata. Documents on inputs, outputs and control scheme of the qst magnetic controller. Technical report, 2018.
- [61] G. De Tommasi et al. Shape Control with the eXtreme Shape Controller During Plasma Current Ramp-Up and Ramp-Down at the JET Tokamak. *J. Fus. Energy*, 33(2):149–157, 2014.
- [62] H. Urano et al. Development of operation scenarios for plasma breakdown and current ramp-up phases in JT-60SA tokamak. *Fus. Eng. Des.*, 100:345–356, 2015.
- [63] H. Meyer et al. Overview of progress in European medium sized tokamaks towards an integrated plasma-edge/wall solution. *Nuclear Fusion*, 57, 2017.
- [64] Y. Miyata et al. Study of JT-60SA Operation Scenario using a Plasma Equilibrium Control Simulator. *Plasma and Fus. Res.*, 8:2405109–2405109, 2013.
- [65] Y. Miyata, T. Suzuki, S. Ide, and H. Urano. Study of Plasma Equilibrium Control for JT-60SA using MECS. *Plasma and Fus. Res.*, 9:3403045–5, 2014.
- [66] C. A.F. Varandas. Engineering aspects of the tokamak isttok. *Fusion Technology*, 29(1):105–115, 1996.
- [67] O. Mitarai, Chijin Xiao, Liyan Zhang, D. McColl, Wei Zhang, G. Conway, A. Hirose, and H. M. Skarsgard. Alternating current plasma operation in the STOR-M tokamak. *Nuclear Fusion*, 36(10):1335–1343, 1996.
- [68] B. J.D. Tubbing, N. A.C. Gottardi, B. J. Green, J. A. How, M. Huart, R. Konig, C. G. Lowry, P. J. Lomas, P. Noll, J. J. O'Rourke, P. H. Rebut, D. Stork, A. Tanga, A. Taroni, and D. J. Ward. AC plasma current operation in the JET tokamak. *Nuclear Fusion*, 32(6):967–972, 1992.
- [69] Guerra Tiago. Real-Time measurement of the plasma electron density at ISTTOK. Master's thesis, Universidade Tecnica de Lisboa, Lisbon, Portugal, 2008.
- [70] H Fernandes, C A F Varandas, J A C Cabral, H Figueiredo, and R Galvão. Engineering aspects of the ISTTOK operation in a multicycle alternating flat-top plasma current regime. *Fusion Engineering and Design*, 43(1):101–113, 1998.

Bibliography

- [71] ISTTOK real-time control assisted by electric probes. *Journal of Physics: Conference Series*, 591(1):12008, 2015.
- [72] Ivo S. Carvalho, Paulo Duarte, Horácio Fernandes, Daniel F. Valcárcel, Pedro J. Carvalho, Carlos Silva, André S. Duarte, André Neto, Jorge Sousa, António J N Batista, Tiago Hekkert, and Bernardo B. Carvalho. *Fusion Engineering and Design*.
- [73] I. S. Carvalho, P. Duarte, H. Fernandes, D. F. Valcárcel, P. J. Carvalho, C. Silva, A. S. Duarte, A. Neto, J. Sousa, A. J. N. Batista, and B. B. Carvalho. ISTTOK control system upgrade. *Fusion Engineering and Design*, 88(6):1122–1126, 2013.
- [74] ATCA control system hardware for the plasma vertical stabilization in the JET tokamak. *IEEE Transactions on Nuclear Science*, 57(2 PART 1):583–588, 2010.
- [75] An analog integrator for thousand second long pulses in Tore Supra. *Fusion Engineering and Design*, 66-68:953–957, 2003.
- [76] Andreas Werner, Michael Endler, Joachim Geiger, and Ralf Koenig. W7-X magnetic diagnostics: Rogowski coil performance for very long pulses. *Review of Scientific Instruments*, 79(10):1–5, 2008.
- [77] A Pironti, F Amato, and Napoli Federico. On-Line Plasma Shape Identification for use in control systems. *Proceedings of International Conference on Control Applications*, pages 1–2, 1995.
- [78] D. W. Swain and G. H. Neilson. An efficient technique for magnetic analysis of non-circular high-beta tokamak equilibria. *Nuclear Fusion*, 22(8):1015–1030, 1982.
- [79] Peter Hippe. *Windup in Control Its Effects and Their Prevention*. Springer, 2011.
- [80] Damir Vrancic and Raymond Hanus. Anti-Windup, Bumpless, and Conditioned Transfer Techniques for PID Controllers. *IEEE Control Systems*, 16(4):48–57, 1996.
- [81] Hao Yu, Tiantian Xie, and Bogdan Wilamowski. *Practical PID Control*. 2011.
- [82] Steven L. Brunton and J. Nathan Kutz. *Data-Driven Science and Engineering: Machine Learning, Dynamical Systems, and Control*. Cambridge University Press, 2019.
- [83] J. D. Bendtsen, J. Stoustrup, and K. Trangbaek. Bumpless transfer between observer-based gain scheduled controllers. *International Journal of Control*, 78(7):491–504, 2005.
- [84] A. Mele, G. De Tommasi, A. Pironti, and B. J. Xiao. Shape reconstruction and eddy currents estimation via Kalman Filter at the EAST tokamak. *45th EPS Conference on Plasma Physics, EPS 2018*, 2018-July:417–420, 2018.
- [85] F. Franklin. *Digital Control of Dynamic Systems*. Ellis-Kagle Press, 3 edition, 1998.

- [86] Sebastian Trimpe, Alexander Millane, Simon Doessegger, and Raffaello D'Andrea. A self-tuning LQR approach demonstrated on an inverted pendulum. In *Proceedings of the 19th World Congress The International Federation of Automatic Control*, volume 19, pages 11281–11287, Cape Town, 2014. IFAC.
- [87] Kenny Uren and George Van. *Predictive PID Control of Non-Minimum Phase Systems*. INTECH, 2011.

A

EXTENDED CONTROL RESULTS

This appendix contains the corresponding plots of the ISTTOK discharges from table 5.2.

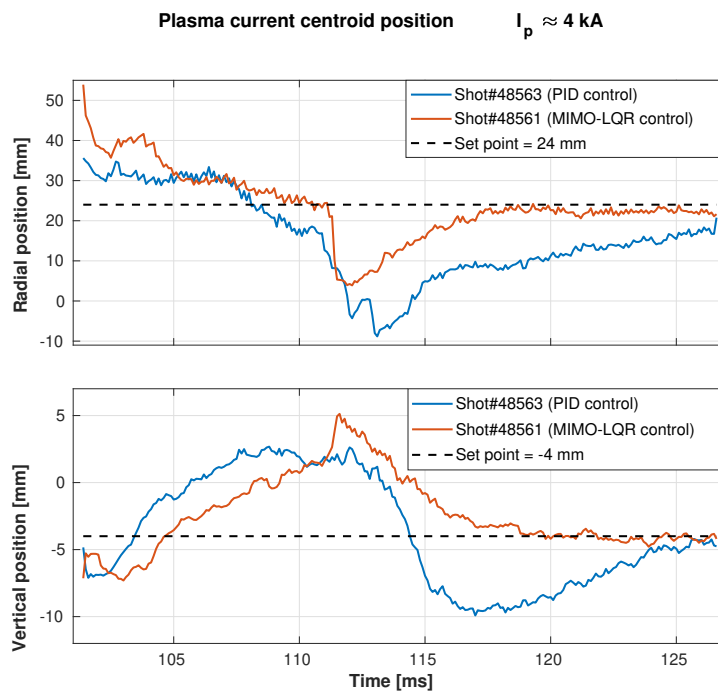


Figure A.1.: Horizontal and vertical plasma centroid position during $I_p \approx 4\text{kA}$ flat-tops, blue time trace corresponds to a PID feedback control and orange time trace to a LQR MIMO feedback control, the dashed black line shows the programmed set point. Shot# 48563 and Shot# 48561.

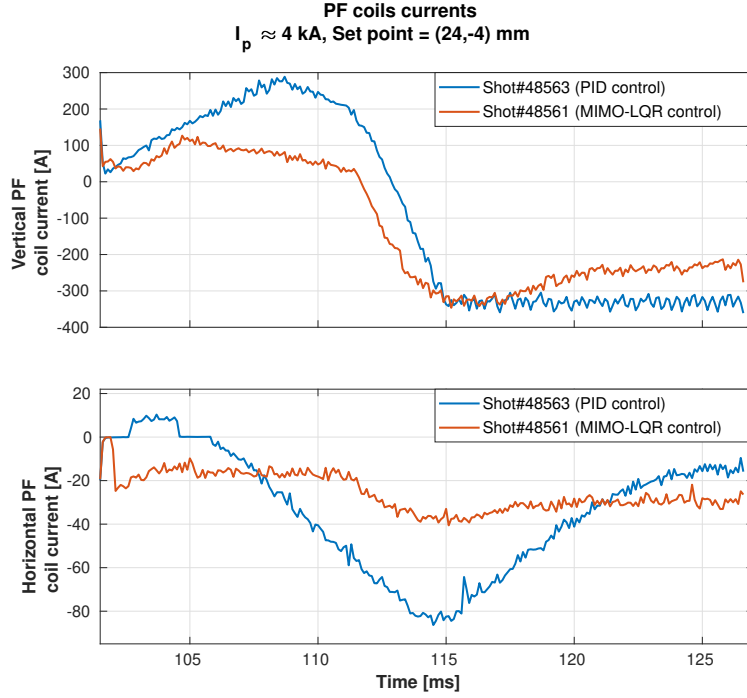


Figure A.2.: Vertical and Horizontal PF coils currents during $I_p \approx 4 \text{ kA}$ flat-tops, blue time trace corresponds to a PID feedback control and orange time trace to a LQR MIMO feedback control. Shot # 48563 and Shot # 48561.

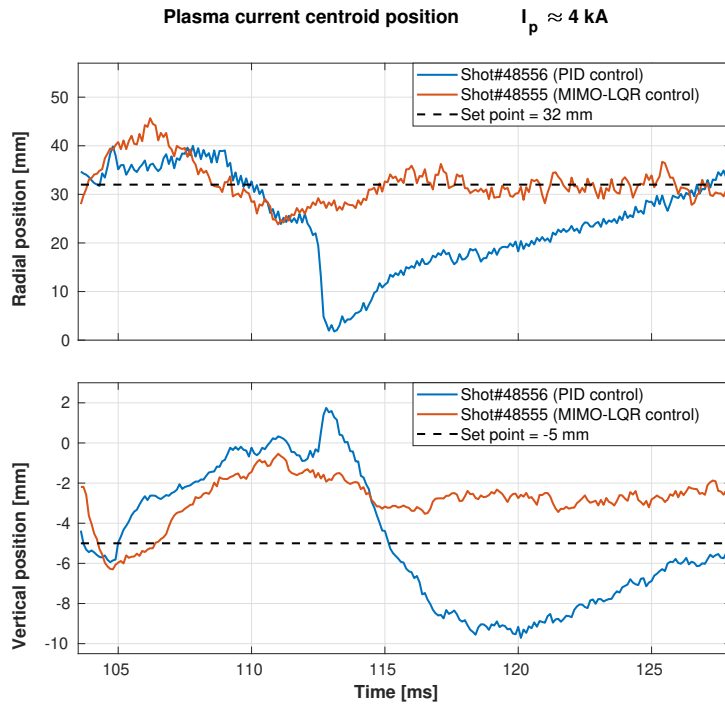


Figure A.3.: Horizontal and vertical plasma centroid position during $I_p \approx 4 \text{ kA}$ flat-tops, blue time trace corresponds to a PID feedback control and orange time trace to a LQR MIMO feedback control, the dashed black line shows the programmed set point. Shot # 48556 and Shot # 48555.

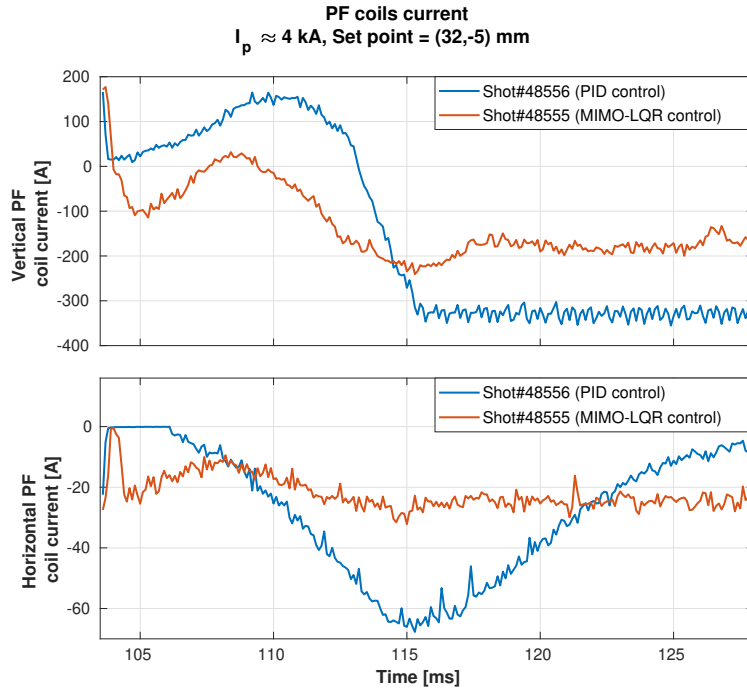


Figure A.4.: Vertical and Horizontal PF coils currents during $I_p \approx 4\text{kA}$ flat-tops, blue time trace corresponds to a PID feedback control and orange time trace to a LQR MIMO feedback control. Shot# 48556 and Shot# 48555.

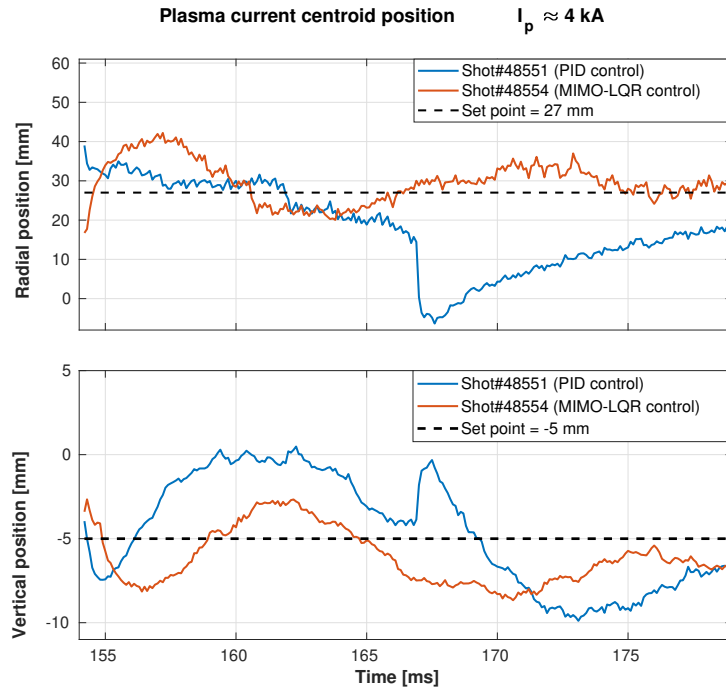


Figure A.5.: Horizontal and vertical plasma centroid position during $I_p \approx 4\text{kA}$ flat-tops, blue time trace corresponds to a PID feedback control and orange time trace to a LQR MIMO feedback control, the dashed black line shows the programmed set point. Shot# 48551 Shot# 48554.

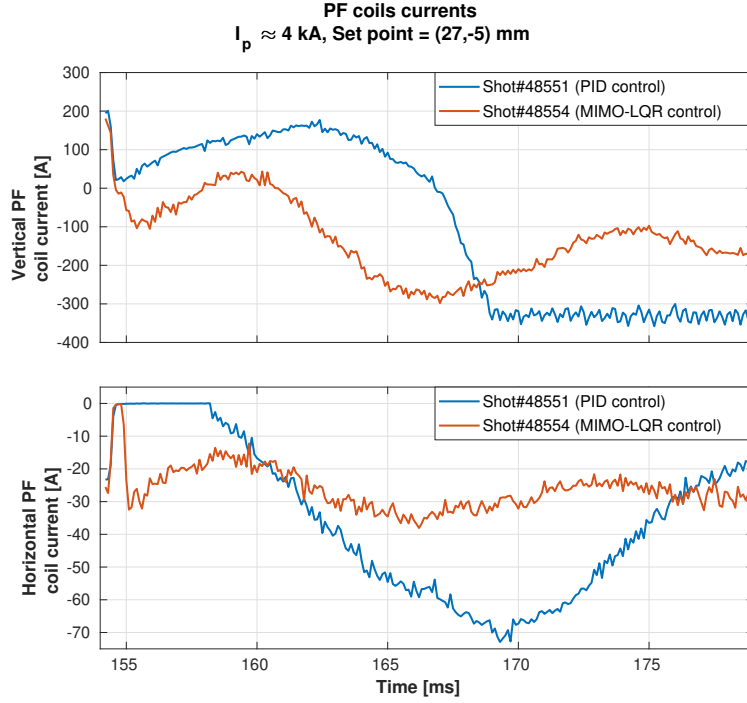


Figure A.6.: Vertical and Horizontal PF coils currents during $I_p \approx 4 \text{ kA}$ flat-tops, blue time trace corresponds to a PID feedback control and orange time trace to a LQR MIMO feedback control. Shot# 48551 and Shot# 48554.

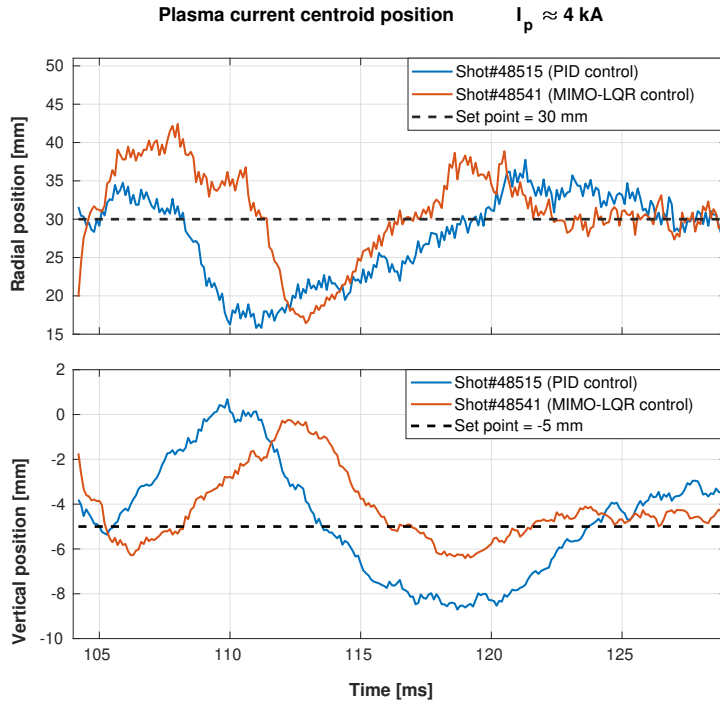


Figure A.7.: Horizontal and vertical plasma centroid position during $I_p \approx 4 \text{ kA}$ flat-tops, blue time trace corresponds to a PID feedback control and orange time trace to a LQR MIMO feedback control, the dashed black line shows the programmed set point. Shot# 48515 and Shot# 48541.

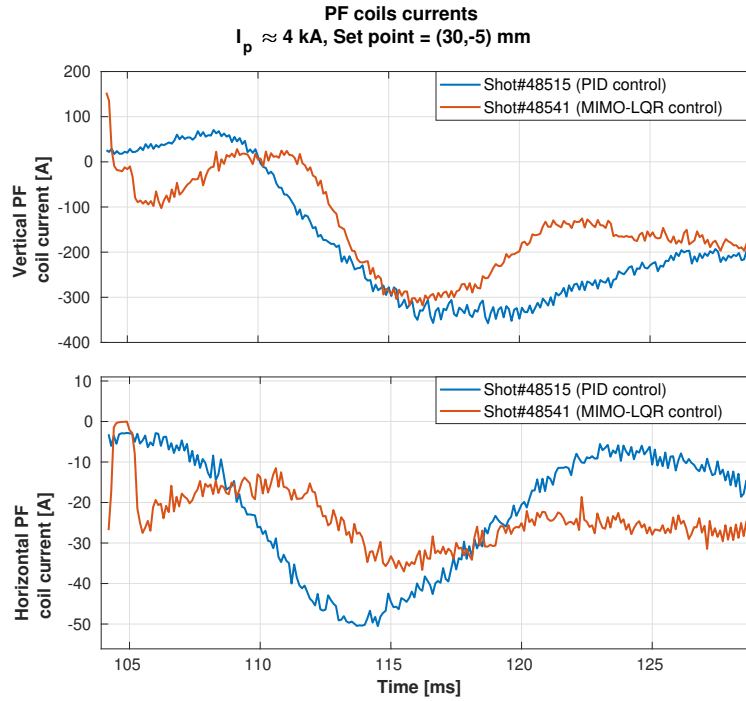


Figure A.8.: Vertical and Horizontal PF coils currents during $I_p \approx 4 \text{ kA}$ flat-tops, blue time trace corresponds to a PID feedback control and orange time trace to a LQR MIMO feedback control. Shot# 48515 and Shot# 48541.

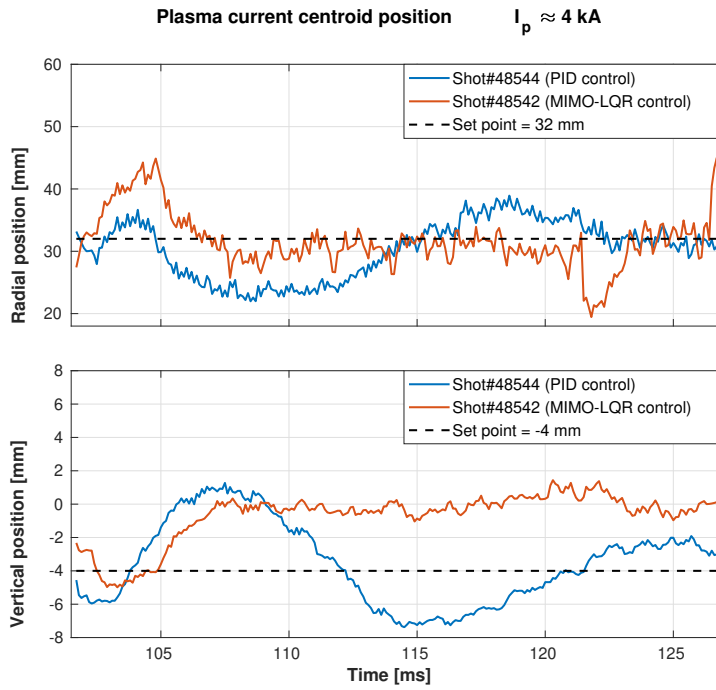


Figure A.9.: Horizontal and vertical plasma centroid position during $I_p \approx 4 \text{ kA}$ flat-tops, blue time trace corresponds to a PID feedback control and orange time trace to a LQR MIMO feedback control, the dashed black line shows the programmed set point. Shot# 48544 and Shot# 48542.

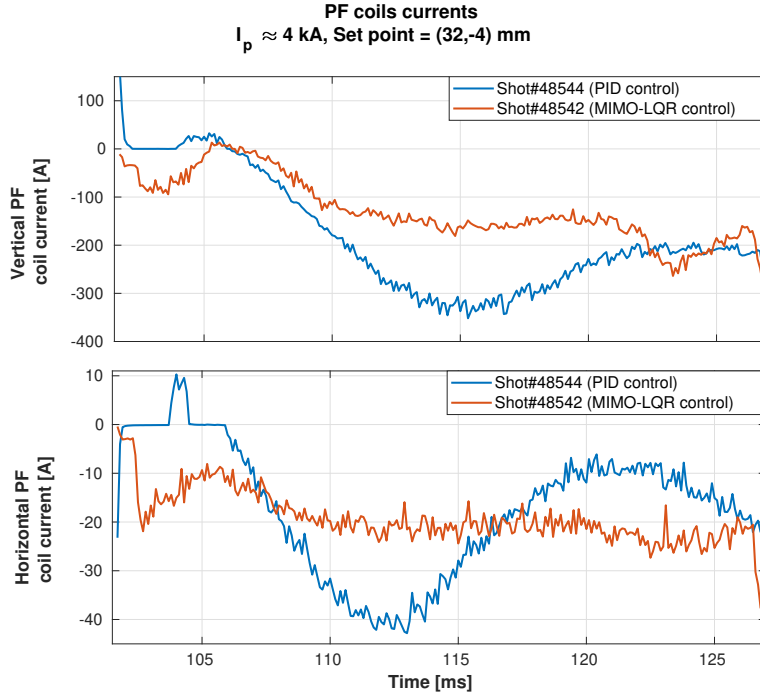


Figure A.10.: Vertical and Horizontal PF coils currents during $I_p \approx 4 \text{ kA}$ flat-tops, blue time trace corresponds to a PID feedback control and orange time trace to a LQR MIMO feedback control. Shot # 48544 and Shot# 48542.

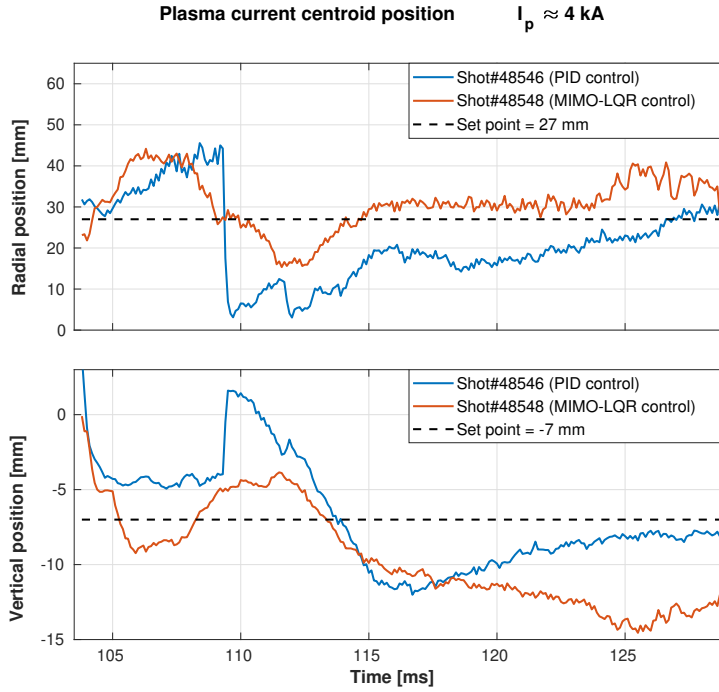


Figure A.11.: Horizontal and vertical plasma centroid position during $I_p \approx 4 \text{ kA}$ flat-tops, blue time trace corresponds to a PID feedback control and orange time trace to a LQR MIMO feedback control, the dashed black line shows the programmed set point. Shot# 48546 and Shot#48548.

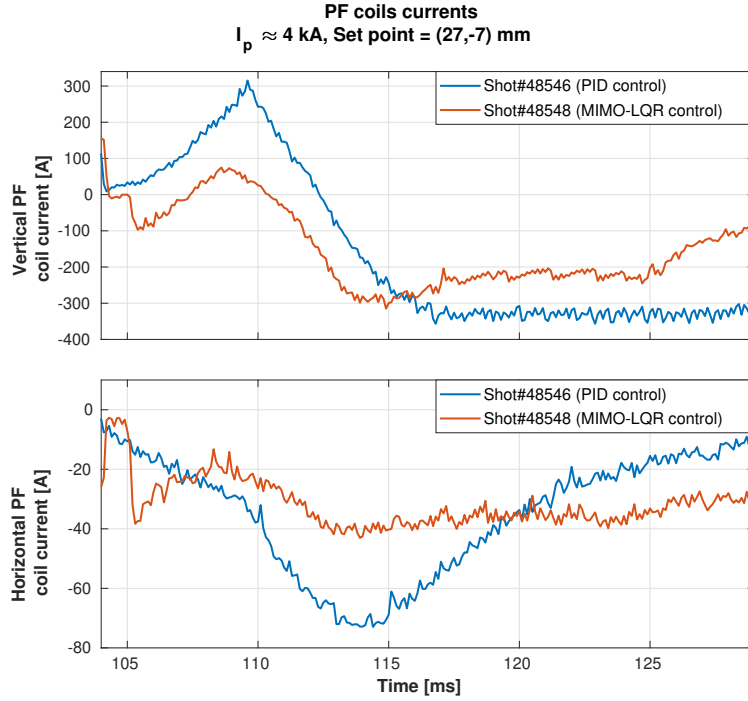


Figure A.12.: Vertical and Horizontal PF coils currents during $I_p \approx 4\text{kA}$ flat-tops, blue time trace corresponds to a PID feedback control and orange time trace to a LQR MIMO feedback control. Shot # 48546 and Shot# 48548.

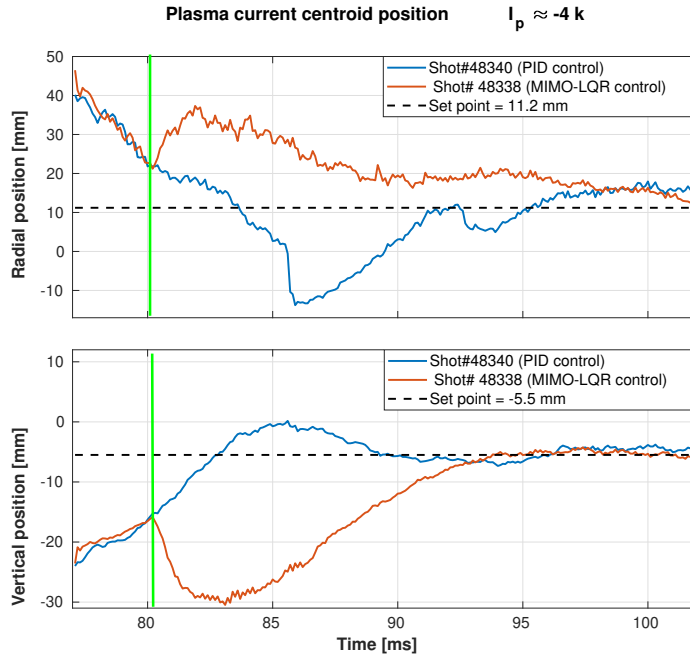


Figure A.13.: Horizontal and vertical plasma centroid position during $I_p \approx 4\text{kA}$ flat-tops, blue time trace corresponds to a PID feedback control and orange time trace to a LQR MIMO feedback control, the dashed black line shows the programmed set point. The green vertical line marks the time when the discharge Shot# 48338 switches from PID to MIMO LQR control.

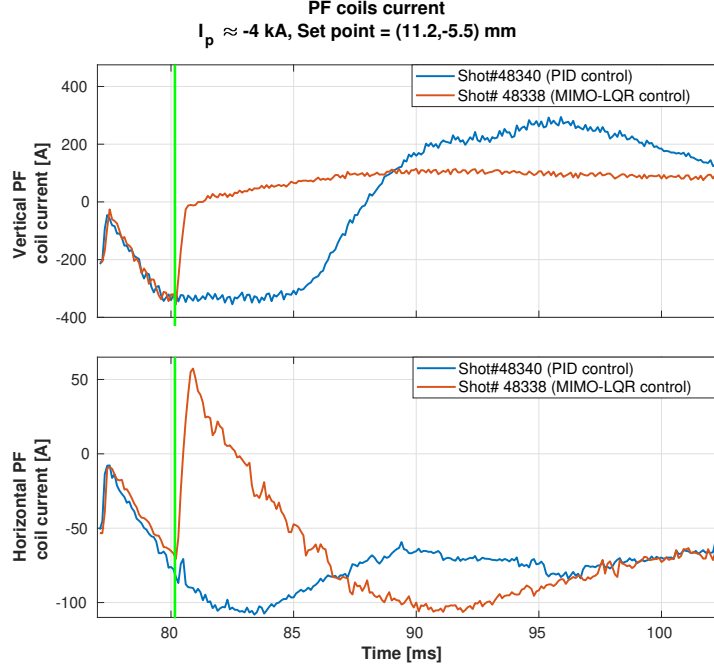


Figure A.14.: Vertical and Horizontal PF coils currents during $I_p \approx -4 \text{ kA}$ flat-tops, blue time trace corresponds to a PID feedback control and orange time trace to a LQR MIMO feedback control. The green vertical line marks the time when the discharge Shot#48338 switches the control from PID to MIMO LQR. Shot# 48340 and Shot# 48338.

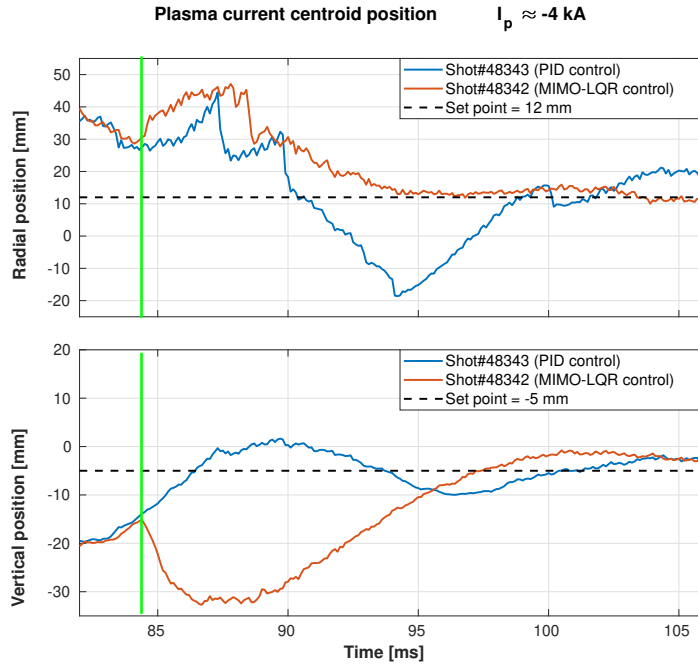


Figure A.15.: Horizontal and vertical plasma centroid position during $I_p \approx 4 \text{ kA}$ flat-tops, blue time trace corresponds to a PID feedback control and orange time trace to a LQR MIMO feedback control, the dashed black line shows the programmed set point. The green vertical line marks the time when the discharge Shot# 48342 switches from PID to MIMO LQR control.

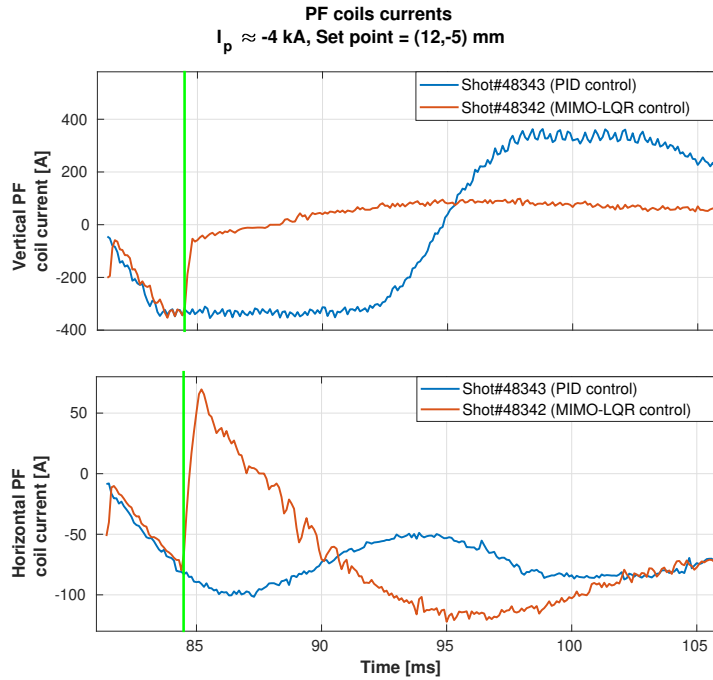


Figure A.16.: Vertical and Horizontal PF coils currents during $I_p \approx -4 \text{ kA}$ flat-tops, blue time trace corresponds to a PID feedback control and orange time trace to a LQR MIMO feedback control. The green vertical line marks the time when the discharge Shot#48342 switches the control from PID to MIMO LQR. Shot # 48343 and Shot# 48342.

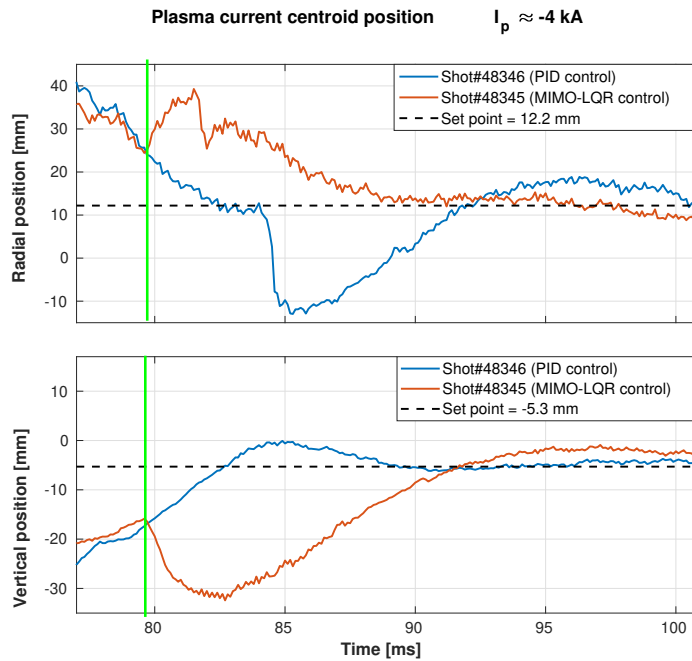


Figure A.17.: Horizontal and vertical plasma centroid position during $I_p \approx 4 \text{ kA}$ flat-tops, blue time trace corresponds to a PID feedback control and orange time trace to a LQR MIMO feedback control, the dashed black line shows the programmed set point. The green vertical line marks the time when the discharge Shot# 48345 switches from PID to MIMO LQR control.

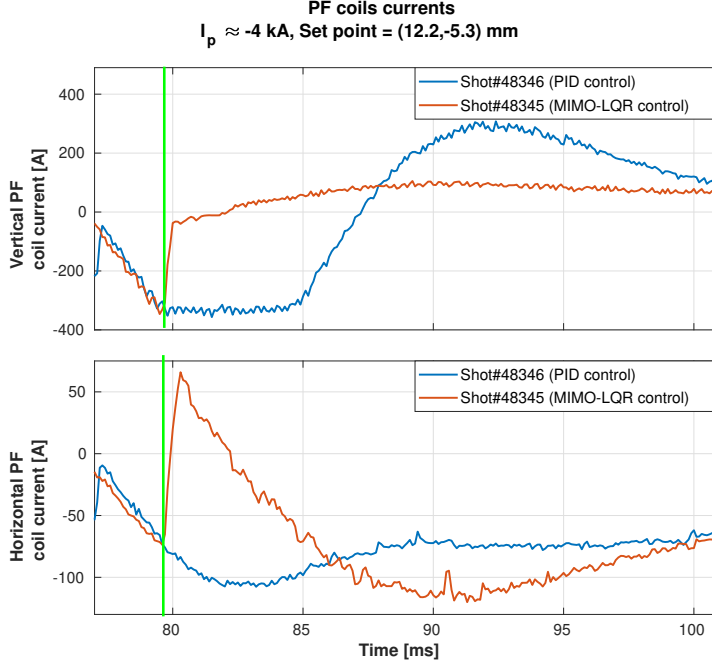


Figure A.18.: Vertical and Horizontal PF coils currents during $I_p \approx -4 \text{ kA}$ flat-tops, blue time trace corresponds to a PID feedback control and orange time trace to a LQR MIMO feedback control. The green vertical line marks the time when the discharge Shot#48345 switches the control from PID to MIMO LQR. Shot# 48346 and Shot# 48345.

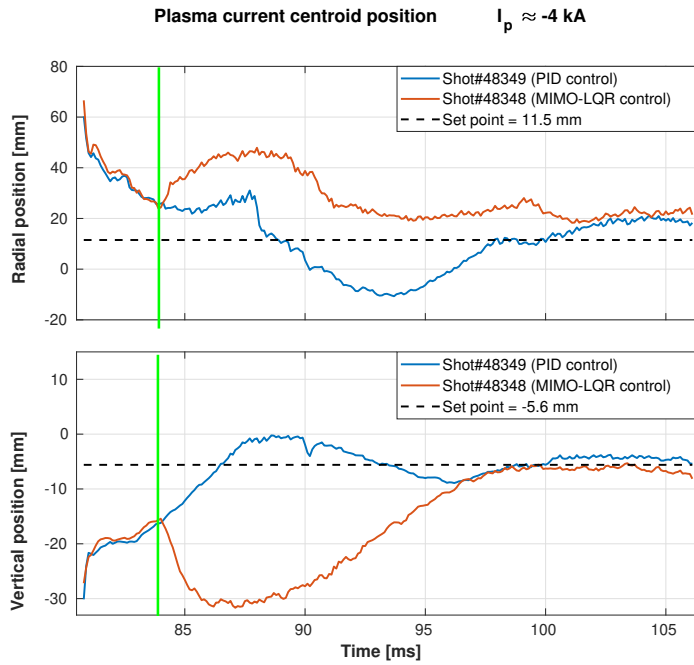


Figure A.19.: Horizontal and vertical plasma centroid position during $I_p \approx 4 \text{ kA}$ flat-tops, blue time trace corresponds to a PID feedback control and orange time trace to a LQR MIMO feedback control, the dashed black line shows the programmed set point. The green vertical line marks the time when the discharge Shot# 48348 switches from PID to MIMO LQR control.

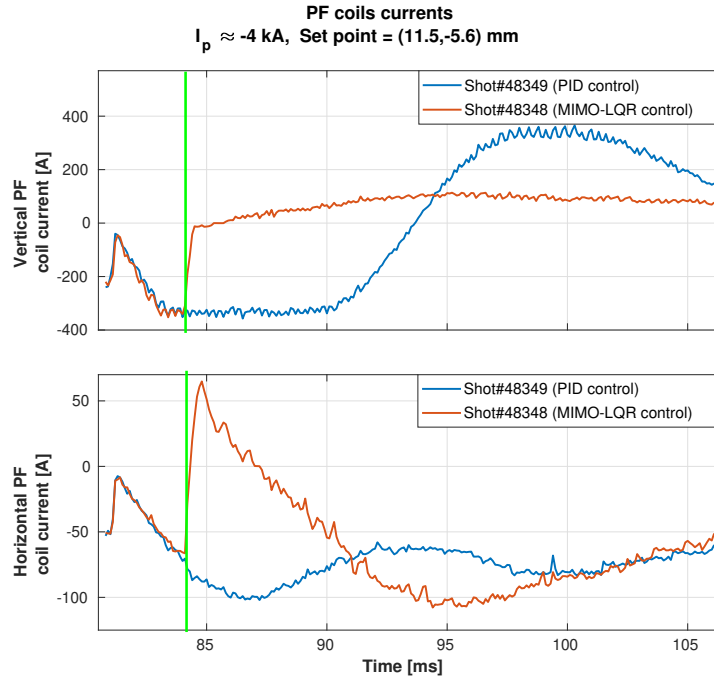


Figure A.20.: Vertical and Horizontal PF coils currents during $I_p \approx -4 \text{ kA}$ flat-tops, blue time trace corresponds to a PID feedback control and orange time trace to a LQR MIMO feedback control. The green vertical line marks the time when the discharge Shot#48348 switches the control from PID to MIMO LQR. Shot# 48349 and Shot# 48348

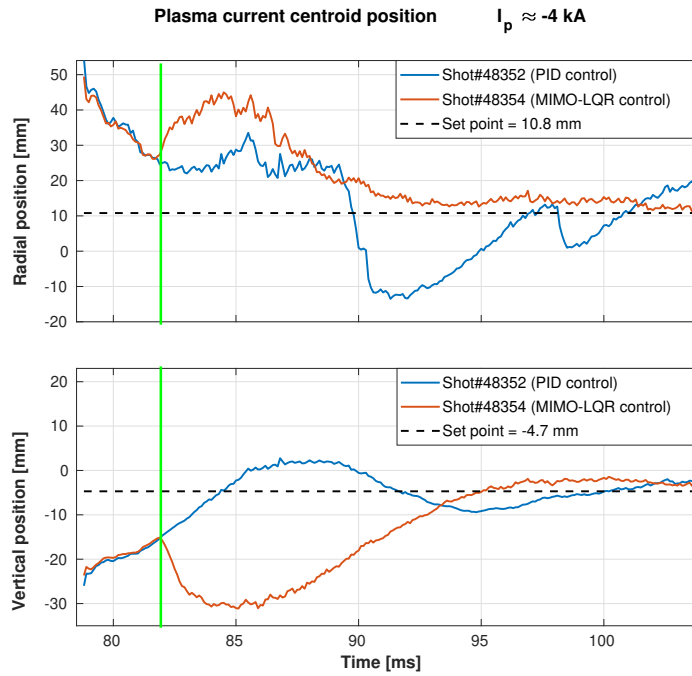


Figure A.21.: Horizontal and vertical plasma centroid position during $I_p \approx 4 \text{ kA}$ flat-tops, blue time trace corresponds to a PID feedback control and orange time trace to a LQR MIMO feedback control, the dashed black line shows the programmed set point. The green vertical line marks the time when the discharge Shot# 48354 switches from PID to MIMO LQR control.

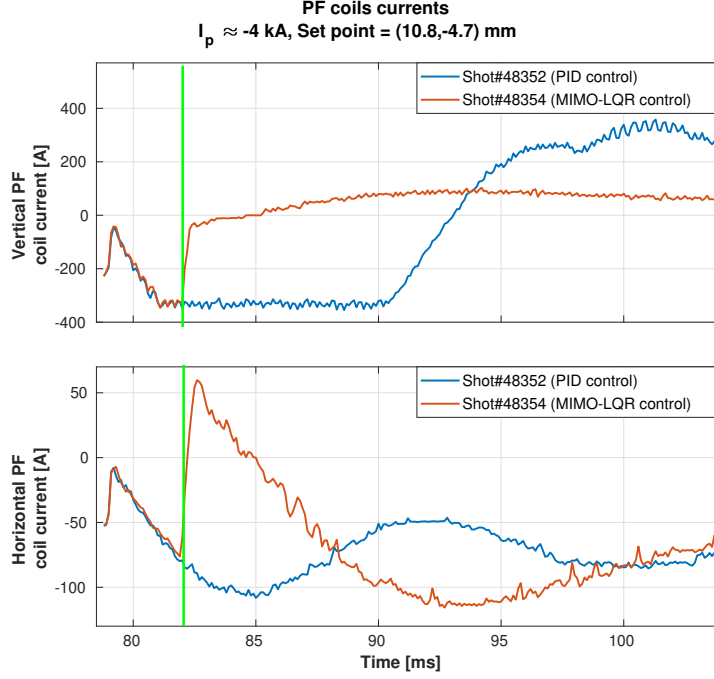


Figure A.22.: Vertical and Horizontal PF coils currents during $I_p \approx -4 \text{ kA}$ flat-tops, blue time trace corresponds to a PID feedback control and orange time trace to a LQR MIMO feedback control. The green vertical line marks the time when the discharge Shot#48354 switches the control from PID to MIMO LQR. Shot# 48352 and Shot# 48354.

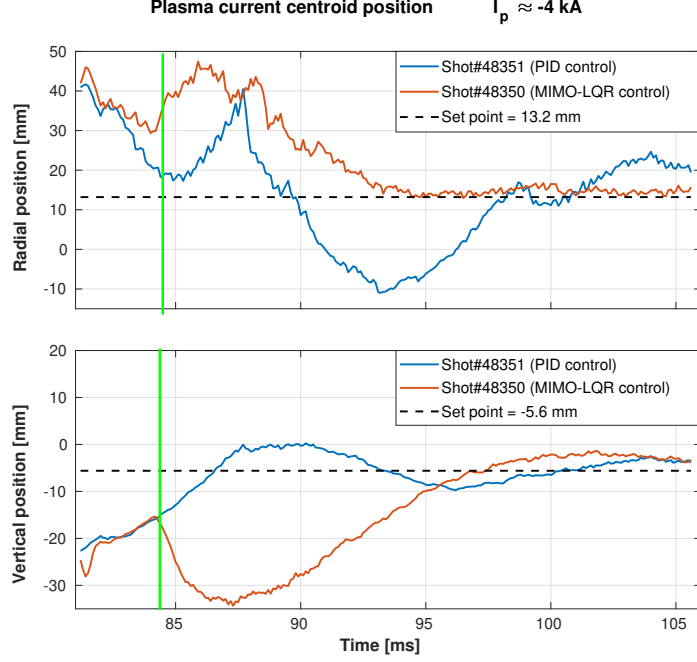


Figure A.23.: Horizontal and vertical plasma centroid position during $I_p \approx 4 \text{ kA}$ flat-tops, blue time trace corresponds to a PID feedback control and orange time trace to a LQR MIMO feedback control, the dashed black line shows the programmed set point. The green vertical line marks the time when the discharge Shot# 48350 switches from PID to MIMO LQR control.

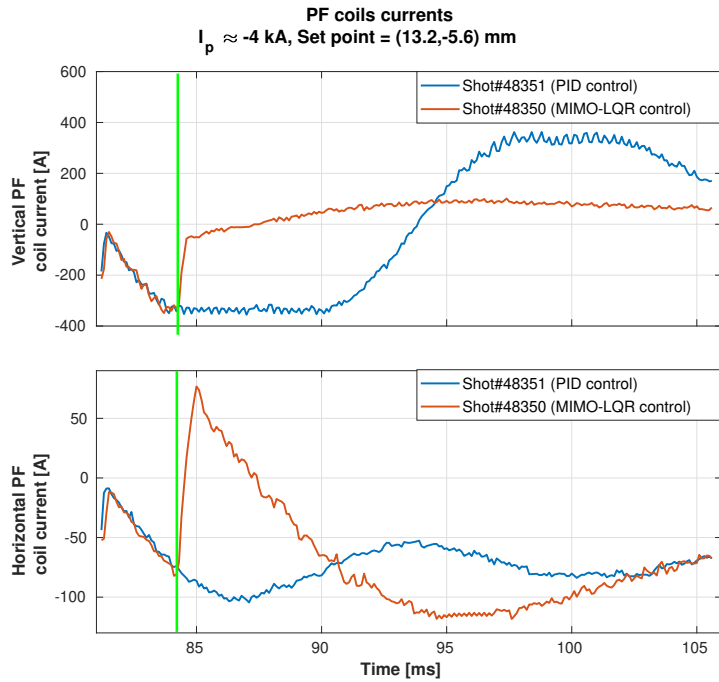


Figure A.24.: Vertical and Horizontal PF coils currents during $I_p \approx -4kA$ flat-tops, blue time trace corresponds to a PID feedback control and orange time trace to a LQR MIMO feedback control. The green vertical line marks the time when the discharge Shot#48350 switches the control from PID to MIMO LQR. Shot# 48351 and Shot# 48350.

B

JT60-SA PICTURES

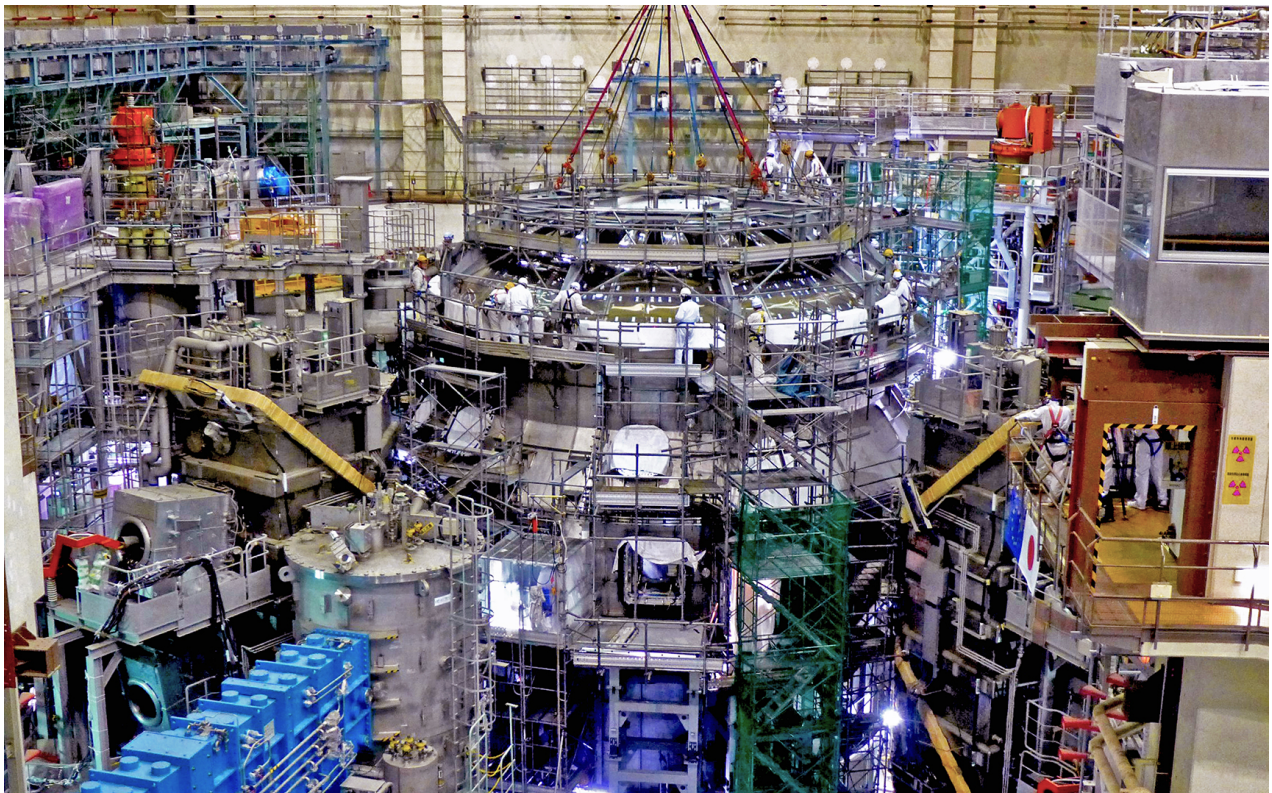


Figure B.1.: JT60-SA assembly when the cryostat top part was installed, 2018.

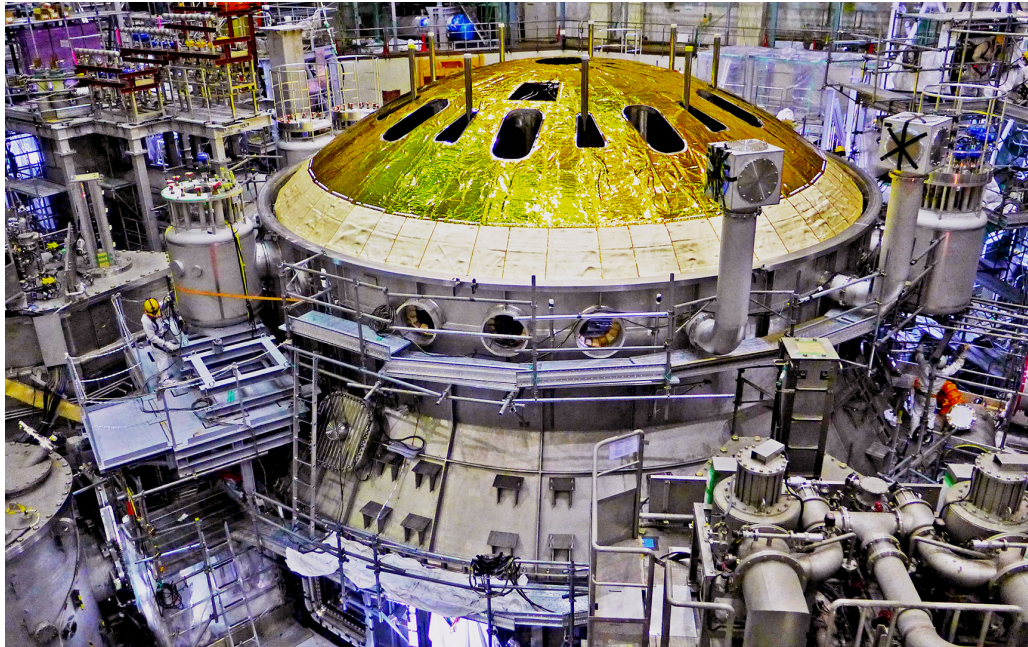


Figure B.2.: JT60-SA assembly in 2019.JT60-SA

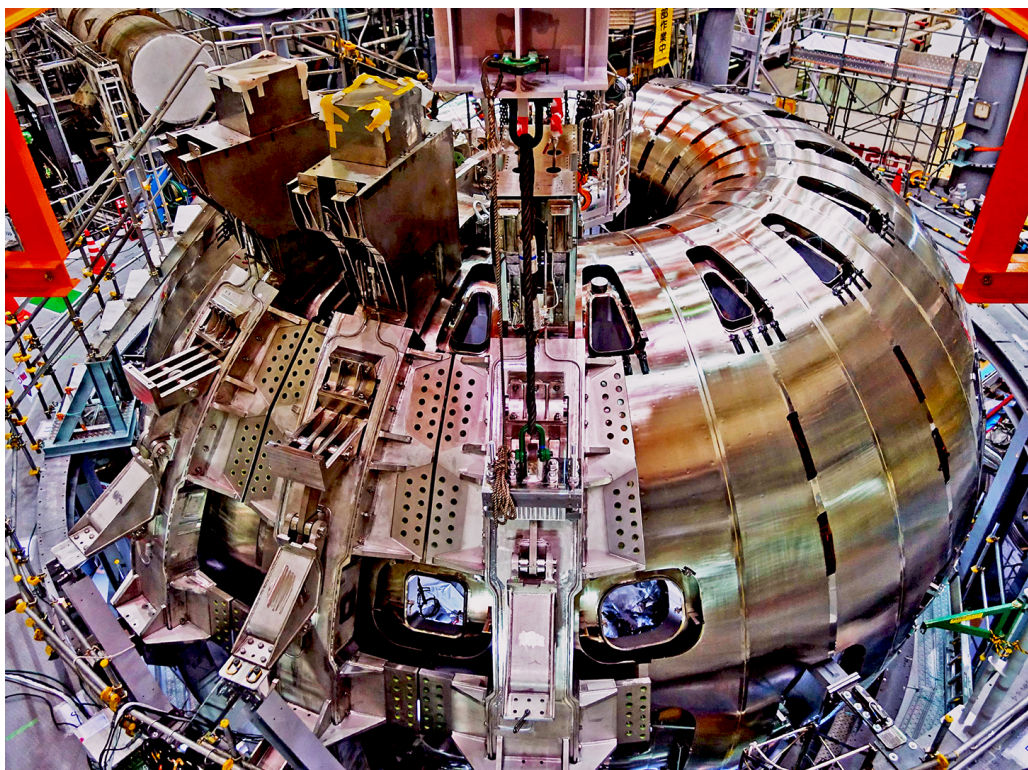


Figure B.3.: JT60-SA insertion of TF coil in 2018.

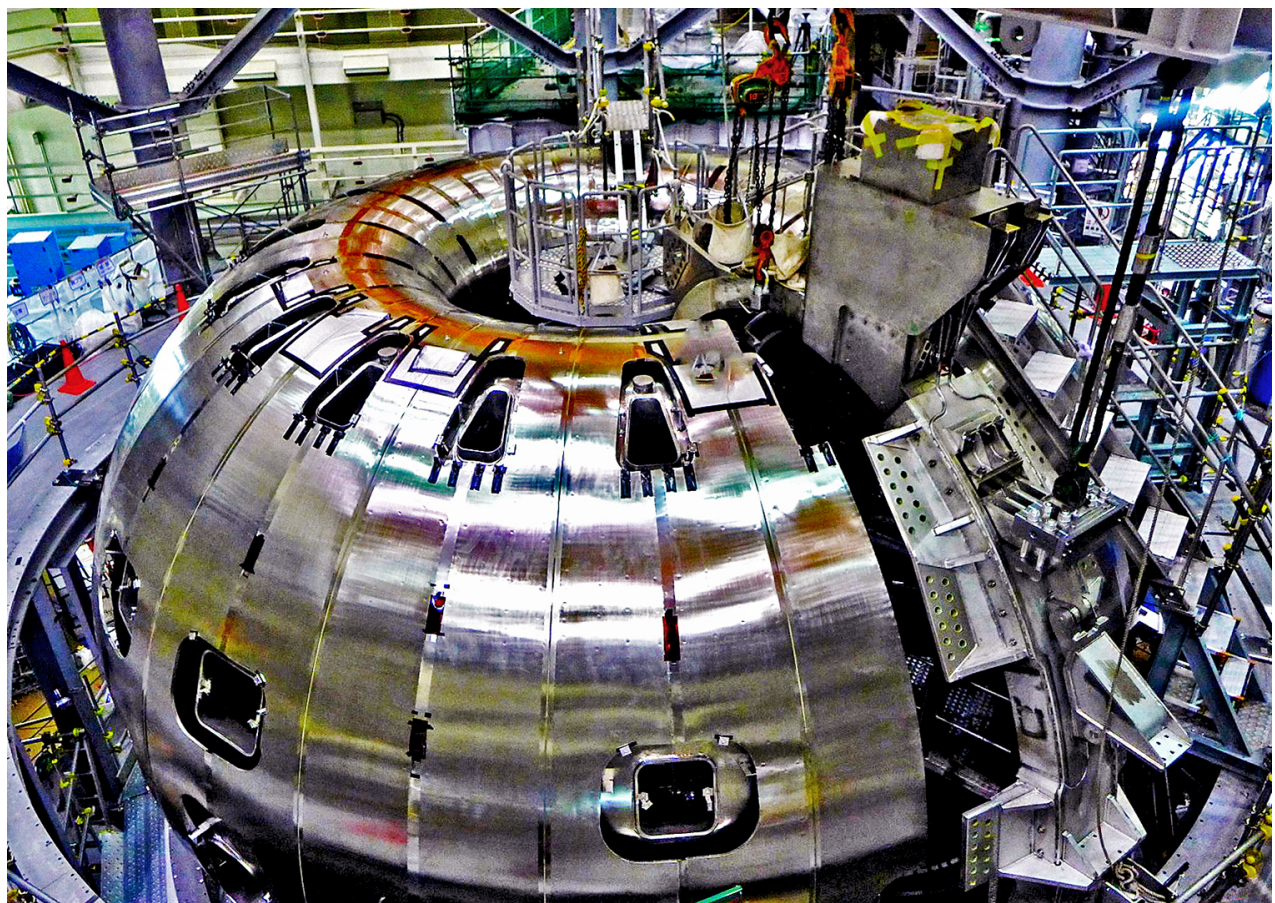


Figure B.4.: JT60-SA insertion of TF coil in 2018.



Figure B.5.: JT60-SA transportation of the first PF coil in 2019.